e-ISSN: 2148-4171

12 cilt volume
1 sayı issue
2025 Mart March

HITTITE JOURNAL OF SCIENCE AND ENGINEERING

HİTİT ÜNİVERSİTESİ YAYINLARI

HITTITE JOURNAL OF SCIENCE AND ENGINEERING

e-ISSN: 2148-4171

Volume 12

March 2025

Issue 1

LANGUAGE OF PUBLICATION

English

CONTACT ADDRESS

Hitit Üniversitesi Mühendislik Fakültesi, ÇORUM, TÜRKİYE
Tel: 0090 364 2191200 Fax: 0090 364 2191399
hjse@hitit.edu.tr | https://www.hjse.hitit.edu.tr

PUBLISHER

Hitit University Press

LOCKSS: http://dergipark.org.tr/hjse/lockss-manifest

OAI: https://dergipark.org.tr/ api/public/oai/hjse/?verb=ListRecords&metadataPrefix=oai_de

FROM EDITOR

Dear Readers,

Today, technological developments in the field of engineering play the most important role in shaping the comfort of our lives. The basis of technological developments is scientific and academic studies. Hittite Journal of Science and Engineering (HJSE) aims to contribute to the implementation of technological developments by disseminating the ideas of scientists. In line with this purpose, we published the first issue of 2025 (2025-Volume 12, Issue 1) by working in a disciplined manner as a team in the first three months of 2025.

As Editor in Chief, I am grateful to all our authors and contributing reviewers of this issue. I also would like to thank the President of Hitit University, Prof. Dr. Ali Osman Öztürk, for his support and interest in HJSE and the Associate Editors of HJSE, namely Prof. Dr. Dursun Ali Kose and Assoc. Prof. Dr. Öncü Akyıldız and also the Section Editors of HJSE, namely Prof. Dr. Murat Hoşöz, Prof. Dr.Kazim Savaş Bahçeci, Prof. Dr. Cengiz Baykasoğlu and Prof. Dr. Akif Akgül as well as our Production Editors, Ömer Faruk Tozlu, Harun Emre Kıran and Hayati Töre for their invaluable efforts in making of the journal.

The new issue of Hittite Journal of Science and Engineering contains six papers from the engineering disciplines including Mechanical Engineering (3), Electrical and Electronics Engineering, Materials Science and Engineering, and Computer Engineering. One of the papers in mechanical engineering observes experimentally the temperatures at the anode, cathode, and midpoint of the battery in natural convection and the effects of passive cooling method on three different organic phase change materials located around Li-ion battery during different discharges. The second one analyses experimentally tool wear and the effect of tool wear on surface roughness under dry machining conditions on X2CrNiMoN2253. It was observed that both the flank wear and notch wear values intensified swiftly and then intensified at a steady rate. The final paper observes the resistance spot welding properties of ultra-high-strength MS1500 steel and hot-rolled DD11 (1.0332) steel of varying thicknesses and it resulted that the effectiveness of the double-pulse welding strategy improves the strength and quality of resistance spot-welded joints. In the scope of the study of electrical and electronics engineering, an electronic nose with eleven gas sensors is improved to observe the garlic concentration in five different yogurt types. As for the article in materials science and engineering, production (vacuum arc melting) and high-temperature oxidation of Y doped (0.08 at.%Y) cost-effective medium entropy AlCrFeNi alloy at 1100 °C for 168h were studied. The last paper, related to computer engineering, aims to create risk profiles based on the behaviors of employees within the company and develop effective measures accordingly and it demonstrates that the use of machine learning tools provides a valuable resource for strengthening companies' cybersecurity strategies.

I am sure that the researchers studying in the above-mentioned disciplines of engineering will benefit from the results of the papers published in this issue.

It's my pleasure to invite researchers and scientists from all branches of engineering to join us by sending their best papers for publication in Hittite Journal of Science and Engineering.

Dr. Ali Kilicarslan

Editor-in-Chief

CONTENTS

From Editor

Research Articles

Determining the Cyber Risk Matrix and Actions Created by Company Employees with Machine Learning
Esma Sığırtmaç, Musa Balta, Deniz Balta.....**1**

Investigation of the Effect on Thermal Performance Using Organic Phase Change Material in Battery Cooling Systems
Mustafa Yasin Gökaslan.....**15**

High Temperature Oxidation of Y doped Equiatomic AlCrFeNi Medium Entropy Alloy
Kerem Özgür Gündüz.....**25**

Assessment of the Altering of Tool Wear and Surface Finish in X2CrNiMoN2253 Stainless Steel Under Dry Machining Conditions
Fikret Sönmez.....**35**

Electronic Detection of Garlic Density in Various Kinds of Yogurts Using Statistical Features
Bilge Han Tozlu.....**43**

Effect of Double-Pulse Strategy on the Expulsion Formation and Peak Loads During Resistance Spot Welding of Dissimilar Thickness Ultra - High Strength MS1500 and Mild DD11 Steels
Mehmet Okan Görtan.....**51**

HITTITE JOURNAL OF SCIENCE AND ENGINEERING

e-ISSN: 2148-4171
Volume: 12 • Number: 1
March 2025

Determining the Cyber Risk Matrix and Actions Created by Company Employees with Machine Learning

Esma Sığırtmaç[1] | Musa Balta[1] | Deniz Balta[2]
[1]Sakarya University, Department of Computer Engineering, Sakarya, Türkiye.
[2]Sakarya University, Department of Software Engineering, Sakarya, Türkiye.

Corresponding Author
Esma Sığırtmaç
E-mail: esma.sigirtmac@ogr.sakarya.edu.tr Phone: +90 543 227 35 87
RORID: https://ror.org/04ttnw109

Article Information
Article Type: Research Article
Doi: https://doi.org/10.17350/HJSE19030000346
Received: 30.01.2024
Accepted: 09.12.2024
Published:25.03.2025

Cite As
Sığırtmaç E, et al. Determining the Cyber Risk Matrix and Actions Created by Company Employees with Machine Learning. Hittite J Sci Eng. 2025; 12(1):1-14.

Peer Review: Evaluated by independent reviewers working in at least two different institutions appointed by the field editor.
Ethical Statement: Not available.
Plagiarism Checks: Yes - iThenticate
Conflict of Interest: Authors declare no conflict of interest.

CRediT AUTHOR STATEMENT
Esma Sığırtmaç: Conceptualization, Data curation, Formal Analysis, Investigation, Methodology, Resources, Supervision, Writing – review and editing. **Musa Balta:** Conceptualization, Data curation, Formal Analysis, Investigation, Methodology, Supervision, Visualization, Writing – original draft & editing. **Deniz Balta:** Conceptualization, Data Curation, Formal Analysis, Methodology, Validation, Writing.

Determining the Cyber Risk Matrix and Actions Created by Company Employees with Machine Learning

Esma Sığırtmaç[1,*] | Musa Balta[1] | Deniz Balta[2]

[1]Sakarya University, Department of Computer Engineering, Sakarya, Türkiye.
[2]Sakarya University, Department of Software Engineering, Sakarya, Türkiye.

Abstract

In today's digital age, the integration of various fields with the internet and technology has enabled people to meet many issues online, from their basic needs to business, banking and entertainment. However, this digital transformation poses new threats for companies, especially in terms of cyber security. Cyber-attacks can directly harm companies, disrupting systems and damaging their credibility. Despite taking technical measures, companies often encounter weaknesses due to the human factor. This study aims to identify profiles that may cause security vulnerabilities and increase the company's cybersecurity defense level with appropriate actions. When the results are examined, it is discovered that people with a certain experience range have the same approaches. Using K-means and Mean Shift clustering algorithms, individuals are grouped according to their behaviors and a cyber risk matrix is created for the company, and it is determined which situations these people fall into which risk category. As a result of the data obtained, it is clearly seen that the human factor has emerged as a more important issue than the technical dimension in cyber security.

Keywords: Security, Machine Learning, Cyber Risk Matrix, Human Factor, Cyber Security Awareness

INTRODUCTION

Humanity, especially after Covid-19, has increasingly turned to using the internet for many tasks. New applications and systems have been developed, and many processes have been moved to the virtual environment. According to the report published by ENISA (The European Union Agency for Cybersecurity) on October 20, 2020, an increase in cyber-attacks and their varieties has been observed [1]. The closures and economic fluctuations experienced after Covid-19 have provided an opportunity for financially motivated criminals to target many corporate and institutional areas by exploiting the increased use of the internet. Tonya Ugoretz, Deputy Assistant Director of the Cyber Division of the FBI (Federal Bureau of Investigation), stated in 2020 that they used to receive 1000 cyber-attack complaints every day before Covid-19. However, after Covid-19, this number experienced a surge, reaching between 3000 and 4000 per day [2].

Research has observed an increase in cyber-attacks and their diversity. Conclusions have been drawn that companies need to take additional security measures to protect against cyber-attacks. However, according to statements from ENISA, existing measures may not be sufficient as attack methods evolve [1].

No matter how many mitigation techniques are taken, the error rate increases when humans are involved. According to reports from ENISA, the most commonly used attack methods during the Covid-19 period are phishing, social engineering, malware, misconfiguration, poor policies, and technology-induced security vulnerabilities [1]. This ranking is made from the most used to the least used.

Organizations should place significant emphasis on technological solutions to combat potential cyber threats. Recent research in cybersecurity strongly agrees that a holistic approach is necessary to resist cyber-attacks, in contrast to relying solely on technical solutions. This is particularly noticeable in well-targeted sectors like education and health, as well as emerging fields such as autonomous vehicles. User behaviors and attitudes can undermine technological advancements.

Due to these developments and the increasing use of the internet, the presence of people of all ages online has become a significant danger for companies [3-4]. Despite companies investing in and prioritizing technical measures, undesirable situations can arise due to the carelessness of an employee within the company.

There are studies in the literature to increase cybersecurity awareness and consciousness. In their study, Avcı and Oruç (2022) examined the relationship between university students' information security awareness and cybersecurity behaviors according to various demographic variables. In order to increase students' awareness, solution suggestions such as including relevant courses in the curriculum, informing students about these issues from an early age, and making them aware of the importance of ensuring cybersecurity were presented [5]. In the study of Yiğit and Seferoğlu (2019), university students' cybersecurity behaviors were examined according to personality traits and variables such as gender, grade level, department, information security training status, and weekly internet usage time. At the end of the study, in the light of the findings, it was suggested that cybersecurity training should be emphasized and students' personality traits should be taken into account in these trainings [6]. In their study, Yetgin and Karakaya (2020) measured the personal cybersecurity perceptions of academic and administrative staff working at Karabük University. The data collected with the survey method were analyzed with Cronbach Alpha, single sample t test, independent sample t test, and ANOVA test. It is not stated that there are differences in the perceptions of employees about personal cyber security according to the parameters and various training suggestions are given [7]. Gündüz and Das (2022) mentioned in their study that personal cyber security awareness can be increased on the end user side with cyber awareness. The article suggests new approaches for end users to create secure passwords within the scope of ensuring the security of online individual identity data [8]. Tokmak (2023) determined the cyber security awareness levels of students about cyber threats with machine learning methods in his study. Data was collected with the survey method. The effect of factors such as the department the students study and gender on the cyber security awareness of students was emphasized [9]. In the

study conducted by Cam et al. (2019), the Internet usage levels and personal information security attitudes of students, employees and academicians at Gümüşhane University were examined. Exploratory factor analysis, descriptive statistical analyses and two-way variance analysis were used for the analysis of the data. The research results emphasized that studies should be conducted to increase the information security awareness levels in higher education institutions. [10].

Based on the data obtained, it is clearly seen that the human factor has become more crucial in cybersecurity than the technical dimension. Within the scope of this study, the aim is to minimize the human risk factor in the field of cybersecurity to the lowest possible level. Investigations have been conducted in various areas such as business life, personal life, education, etc., where the internet can be utilized. In order to minimize the human factor, specific methods and research results have been consolidated at a common point, leading to a human-centric approach.

Due to evolving new cyber-attack methods and threats, it is essential to raise awareness among individuals. Tailored education needs to be provided to individuals based on their specific needs, guiding them through instructive actions and actions to avoid. Research and observations have revealed that technical security measures alone are not sufficient.
In this study, individuals are aimed to be grouped based on survey results. Tests have been conducted on various parameters and data using technologies, leading to similar results.

The literature on cyber risks in companies has indeed explored various methodologies for grouping individuals based on survey results, particularly in relation to risk assessment and management. Several studies have examined the factors contributing to cyber risks, the effectiveness of cyber insurance, and the implications of organizational behavior in mitigating these risks. One significant study by Talesh discusses how cyber risk management services, including cyber insurance, not only reduce risks but also shape compliance behaviors within organizations. This research highlights the role of insurance companies as "compliance managers," indicating that organizations are increasingly institutionalizing responses to cyber risks through insurance policies [11]. This perspective is critical as it suggests that organizations can be grouped based on their compliance strategies and the extent to which they engage with cyber insurance. This aligns with findings from Kenny et al., who identified specific demographic factors that correlate with cyber-victimization among different groups [12]. Such demographic insights could be crucial for grouping individuals based on their risk profiles. In the context of cybersecurity awareness, Tempestini et al. developed a tool to assess cybersecurity knowledge among college students, categorizing participants into risk groups based on their reported behaviors and experiences [13]. This method of grouping individuals based on survey responses is particularly relevant to the task of identifying cyber risk profiles.

Moreover, the work of Bergh and Junger reviews victim surveys related to cybercrime across Europe, emphasizing the need for standardized methodologies in assessing cyber risks. They argue that such standardization can facilitate better grouping of organizations based on their experiences with cybercrime victimization [14]. This aligns with the idea that organizations can be categorized based on their risk profiles and responses to cyber incidents. In the context of cyber incident prediction, Pramoda et al. present a novel model that utilizes machine learning to assess the risk of cyber incidents among different demographics. Their findings indicate that increased internet usage correlates with a higher likelihood of cyber incidents, suggesting that organizations can be grouped based on their employees' internet usage patterns and associated risks [15]. This quantitative approach to risk assessment is crucial for developing targeted interventions. Additionally, the research by Nurse et al. emphasizes the importance of understanding the complexities of assessing security risks in Internet of Things (IoT) systems. Their findings indicate that professionals from various sectors identify key issues in cyber-risk assessment, which can inform how organizations are grouped based on their technological vulnerabilities and risk management practices [16]. This highlights the necessity of a multidisciplinary approach to cyber risk assessment, which can lead to more effective grouping of organizations based on their specific risk profiles. Furthermore, the study by Cains et al. focuses on defining cyber security and cyber security risk within a multidisciplinary context, utilizing expert elicitation methods. This research underscores the importance of a common understanding of cyber risks, which can facilitate the grouping of organizations based on their perceived vulnerabilities and risk management strategies [17]. In summary, the literature provides substantial evidence that grouping individuals and organizations based on survey results related to cyber risks has been explored through various lenses, including compliance behaviors, victimization surveys, incident prediction models, and multidisciplinary definitions of cyber security. These studies collectively contribute to a deeper understanding of how organizations can be categorized based on their cyber risk profiles and management strategies.

Upon reviewing the results, it was discovered that individuals within certain experience year ranges exhibit similar approaches. Accordingly, individuals within certain experience year ranges show similarities in terms of mistakes and shortcomings. By creating a cyber risk matrix, it has been determined which risk category corresponds to these individuals for specific situations, and necessary precautions and actions have been recommended.

By using the cyber risk matrix, actions are taken for existing employees or new incoming employees based on their position on the matrix. Through the cyber risk matrix, the deficiencies in employees' cybersecurity aspects are addressed, aiming to minimize the human factor in cyber threats.

MATERIAL AND METHODS

Determining the Algorithm

There are many questions and answers related to the study. However, how individuals will behave is uncertain. The use of

machine learning is important for clustering individuals, but when it comes to human behavior, a clear result cannot be obtained. Therefore, using any form of supervised machine learning algorithm is not considered.

In the early stages of the study, clustering with regression algorithms was attempted. The analysis of behavior was based on the measures individuals took and whether they had previously experienced a cyber-attack. Behavior analysis was conducted based on this information. However, in the survey results, it was observed that a significant number of individuals claimed to have never experienced a cyber-attack or did not know about it. Therefore, a clear conclusion about whether individuals have experienced a cyber-attack or not could not be reached. Additionally, a person who has previously experienced a cyber-attack is likely to have learned from the incident and is less likely to be targeted again.

As a result of observations and investigations, it was concluded that supervised studies would not yield satisfactory results. Due to the inherent lack of clear results in human behavior, using an unsupervised algorithm would be more appropriate when working with these individuals. Upon examining unsupervised algorithms, it was found that there are various types available. The investigations revealed that clustering algorithms in the category of unsupervised algorithms provided the desired results.

Clustering involves algorithms that group data based on similarities according to entered parameters. These algorithms have different working principles, such as distance to the center, distance to neighbors, etc. However, they all share a common point: grouping similar data.

K-Means Algorithm

To test the functionality of the code and the established system, testing was initially started with K-means. Because the K-Means algorithm is a frequently used method in cluster analysis of data expressed with high-dimensional and continuous variables, especially survey data. In the evaluation of cyber awareness survey results, the K-Means algorithm is an effective method to separate individuals into similar groups according to their awareness levels [18].

The K-Means algorithm is a center-based clustering method used to divide data into K clusters. The algorithm works on the assumption that each cluster is clustered around a center point (centroid) and that data points with similar characteristics are placed in the same cluster. Each data point is assigned to the nearest center by measuring the distances to the center points, so that similar data points are included in the same cluster. The Working Steps of the K-Means Algorithm are as follows.

Determining the K Value: First, it is necessary to determine how many clusters will be created (K value). The K value is usually determined according to the structure of the data or the purpose of the analysis.

Assigning Initial Centers: K random center (centroid) points are selected.

Assignment Step: Each data point is assigned to the nearest center point.

Updating Centers: New center points are determined by calculating the average for each cluster.

Iteration: Assigning data points to clusters and updating the centers is repeated until the centers do not change or a specified number of iterations is reached.

In this study, the elbow method was used to find the appropriate K value in areas where K-means was used. When the groups were examined in order from one to nine, it was seen that the break in the resulting graph occurred at 4. In this case, the K value was determined as 4 in the algorithm. The number of iterations was determined as 300 by default.

Mean Shift Algorithm

The K-means algorithm works with two parameters. In some complex cases, K-means is sufficient. However, in more problematic and complex cases, sufficient results are not obtained. For this, it is necessary to use a new structure that takes three parameters with the same working method and the same grouping system. Data is analyzed by switching between K-means or Mean Shift according to the need [19].

Mean Shift is based on the principle of shifting cluster centers towards the areas where the densities are highest. This algorithm does not require any fixed K number (predetermined number of clusters), instead it creates clusters by itself by focusing on the regions where the data density is. Thanks to this feature, it is ideal for revealing natural clusters in the data structure. The Working Steps of the Mean Shift Algorithm are as follows.

Determining the Starting Points: Each data point is initially considered a cluster center (centroid).

Mean Shift: Each point is “shifted” toward the center of the surrounding data density. A mean vector is calculated for each point by considering the other points within a certain bandwidth.

Approaching the Density Peaks: All data points continue this shifting process iteratively and eventually cluster at the density peaks. This process continues until a density center is found where the centers do not change any further.

Creating the Clusters: Once the shifting process is complete, the centers that are close to each other are merged, thus obtaining clusters.

COLLECTION AND FORMATTING OF DATA

Survey Content and Questions

In this study, a survey called Cyber Awareness Form was created for company employees. Participants access the Cyber Awareness Form survey via the internet and fill out the survey anonymously. The Cyber Awareness Form survey consists of 22 questions. These questions aim to measure

the cyber awareness rate of company employees. The Cyber Awareness Form survey was mostly filled out by employees in sectors such as IT, banking, finance, automotive, etc. A total of 659 people responded to the survey called Cyber Awareness Form. The distribution of people by sector is shown in Figure 1.

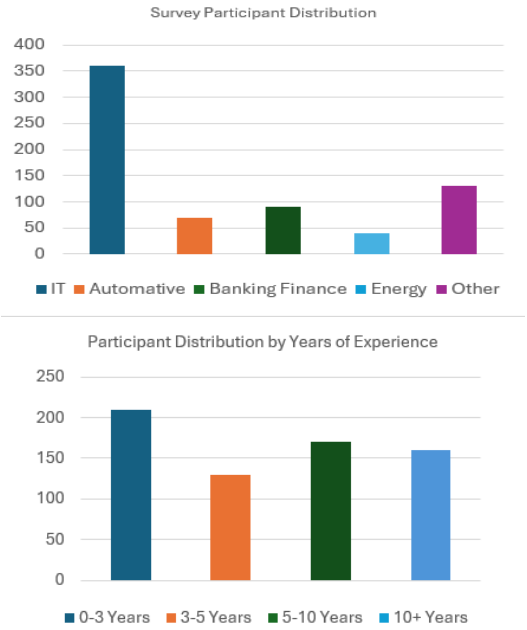

Figure 1. Participant distribution by sector and years of experience

Password security refers to the measures taken to increase the security of passwords used to access digital accounts. A password is an authentication information that is often used in conjunction with a username and is kept confidential to ensure account security. The main goal is to keep user accounts safe by ensuring that these passwords are protected against unauthorized access.

The survey also includes password security questions. Passwords that are long, complex and consist of random characters should be preferred. The questions aim to measure the user's password security knowledge by asking what kind of characters the passwords contain, the frequency of changing passwords, and how users store their passwords.

Email security refers to the measures taken to protect electronic communication from various threats. These measures aim to enhance the privacy, integrity, and security of messages sent and received through email services. Email security plays a critical role in safeguarding sensitive information for individuals, businesses, and organizations, as well as in resisting cyber-attacks and establishing reliable communication channels.

Email security involves implementing measures to protect electronic communication and mitigate threats such as unauthorized access, data leakage, phishing, and malicious software. Employees should carefully verify the links in the emails they receive. Reporting harmful or fraudulent emails to the relevant team is crucial for the company's security.

Testing and Performance Measurement

First of all, the textual data obtained from the surveys were converted into numerical data and made ready to be used in algorithms. After that, random data was created in certain models to determine the most accurate algorithm. Apart from the survey, a study needs to be conducted to see the performance and outputs of the most well-known algorithms with randomly generated data. A structure has been prepared in which 10 algorithms can be tested. With the generated random data, spiral, circular, ring, linear and random etc. 6 types of data types have been prepared: The prepared data were entered into the algorithms one by one and the graph in Figure 2 was obtained.

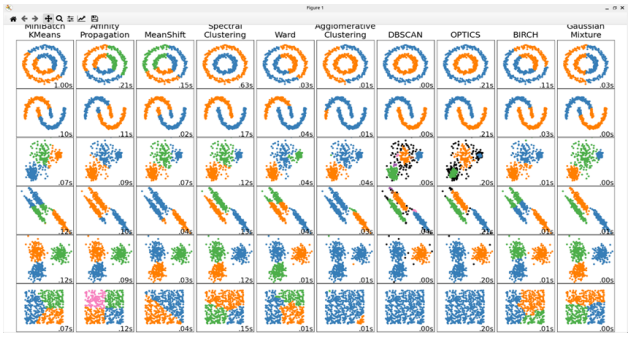

Figure 2. Algorithm comparison chart.

When examining the graph in Figure 2, several algorithms deemed suitable for use have been identified. Through research on these algorithms, the goal is to progress using these algorithms. The first of the identified algorithms is DBSCAN. The main advantages of this algorithm include not requiring the pre-specification of the number of groups, ease of clustering complex and varied data, and the presence of the concept of noise [4]. Due to these specified features of the DBSCAN algorithm, its usage has been observed to be appropriate. Especially, the concept of noise will be useful for exceptional cases outside the groups. However, over time, in some cases, all points from survey data have been perceived as noise. The use of the DBSCAN algorithm was deemed inappropriate due to considering all survey responses as noise.

After understanding the DBSCAN situation, other algorithms similar to it were ruled out. As a result of research, the decision was made to continue with the K-means algorithm for the data sets of our cybersecurity awareness survey. Finally, when exploring the Mean Shift algorithm, which produces similar outputs to K-means, it was noticed that it can take 3 parameters. In this case, it was identified that by adding another parameter, Y, instead of just adding the experience years and X as parameters, a three-dimensional graph can be plotted.

For example, by adding 3 parameters such as experience years, those who have fallen victim to phishing attacks, and mail URL (Uniform Resource Locator) check, we can make an inference about individuals' awareness levels. The use of the Mean Shift algorithm will be necessary to establish the structure due to its ability to take 3 parameters. Additionally,

it can yield good results in a complex dataset.

As seen in Figure 2, the data that needs to be examined will appear randomly distributed on a flat plane, such as the ones in the 3rd or 5th shape on the graph. Clustering distribution could not be done smoothly with K-means, Mean Shift, and a few other algorithms. When Figure 2 is examined, it is observed that while some data should be divided into at least three groups, some are divided into two groups and some into one group. Also, there are algorithms that perceive the dataset as noise. Assuming that the survey data is not so complex, the use of algorithms that do not separate into at least three groups will not be appropriate.

After the decision, instead of test data or random data; The formatted version of the survey data will be tested on these algorithms. After the data was run, all DBSCAN data was detected as noise. DBSCAN perceived all questions with two answers as noise. For questions with more than two answers, only a single data group was created. It is seen that using the DBSCAN algorithm within the scope of this study will not give accurate results.

After the test with K-means, appropriate results were obtained for questions with two answers. As seen in Figure 3 the center points have been removed for a question with a yes or no answer. In addition, the grouping process was carried out in line with the needs.

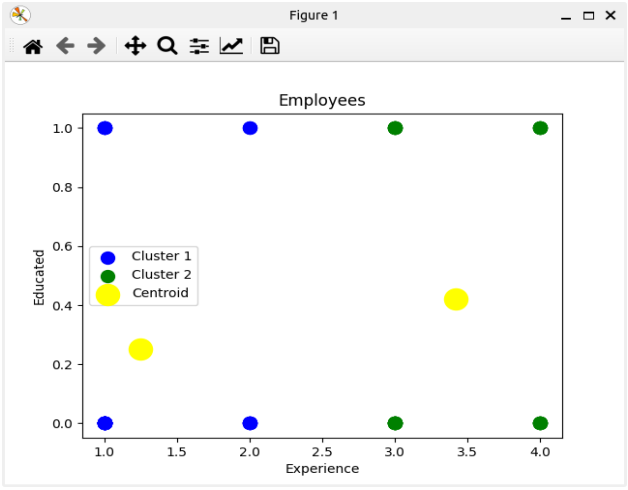

Figure 3. K-means plot tested with survey questions.

An example parameter has been selected for the accuracy of the algorithm, and the accuracy of the graph generated in Figure 3 has been tested with this parameter. According to the description in the graph, the dataset is divided into 2 groups. One group, represented by the blue color, includes employees with experience intervals of 0-3 and 3-5 years. The other group, shown in green, represents those with experience intervals of 5-10 and 10+ years. Another parameter is whether cybersecurity awareness training has been received or not. Looking at the centroids (centers of mass), the centroid for the blue group is located at the level of 0.2. The centroid for the green group is found at the level of 0.5. According to the obtained data, it is observed that individuals with fewer years of experience mostly have not undergone cybersecurity awareness training.

When the filled survey data is filtered and examined, it is likely that the situation appears this way. Upon examining the dataset, it is observed that the education level of individuals with 0-5 years of experience is lower than those with more than 5 years of experience. Additionally, in the group of participants with 0-5 years of experience, the number of individuals with 0-3 years of experience is observed to be higher than the group with 3-5 years of experience. The center of the blue group in the graph is also seen to shift to the left because the number of participants with 0-3 years of experience is higher as the center of mass. This test has been further validated with a few more data points, and similar studies on Mean Shift graphs have demonstrated effective clustering, indicating the accurate functioning of the algorithms.

RESULTS AND DISCUSSION

After ensuring the accuracy of the graphs, the next stage is the examination and interpretation of the data. In this stage, the progress was as follows: Other data were run according to the main parameter, which is the years of experience, and the situation was noted. During the processes, responses for different years of experience were compared with each other. After the general processes, the responses fed into the algorithm were classified based on the years of experience. For example, the algorithm was run for individuals with only 0-3 years of experience, and detailed data were examined. Then, a similar analysis was conducted for individuals with 3-5 years of experience.

As seen in Figure 3, there is a shift to the left at the center of the blue group. This means that there are more individuals with 0-3 years of experience in the blue group. Individuals within the 0-3 years of experience range determine the position of the center point and influence the responses of individuals with 3-5 years of experience. Individuals with 0-3 years of experience form the majority in the group representing the 0-5 years of experience range. This would lead to incorrect results, so after running the algorithm in a general sense, detailed analyses were conducted for each experience year group.

For the subsequent processes, the dataset was interpreted with different parameters, and a matrix was created. For this, a structure moving from general to specific was established. In this structure, individuals of all ages and experiences were examined under a single framework. At the end of the examination, it is more clearly understood whether individuals pose a cyber risk based on the study conducted by age. This results in a conclusion about under what conditions individuals create risks.

The first examined data is whether individuals have experienced a cyber-attack before. Since the answer to this question is more than two, the Mean Shift algorithm has been used to obtain the most accurate result. Three parameters, namely age, years of experience, and whether they have experienced a cyber-attack before, were provided to the

algorithm. When Figure 4 is examined, it can be seen that the data specifying years of experience is located at the bottom of the graph.

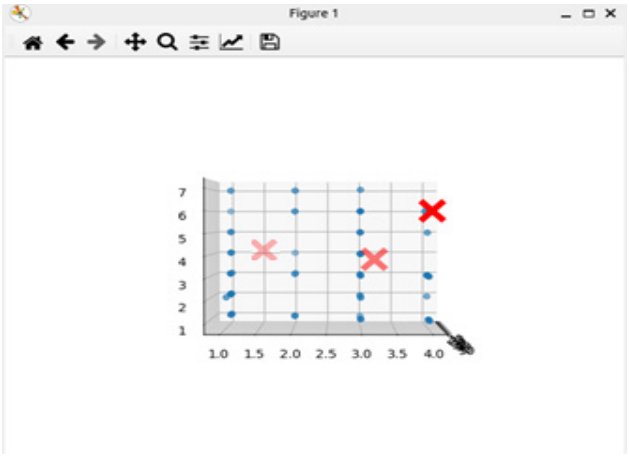

Figure 4. Previous cyber-attack incident graph.

In the graph in Figure 4, the data densely packed on the right side represents the age of individuals. The data on the left side represents the response individuals gave to this question. Since there are more than two answers to the question, the data needs to be formatted. According to the numbers on the left side of the graph, the answers are as follows: 1 = "I don't know," 2 = "I haven't experienced it," 3 = "Compromise of information due to link redirection via email (Phishing)," 4 = "Navigating on harmful websites," 5 = "Use of familiar disks/CDs, etc. used on different devices," 6 = "Through an application downloaded from the internet," 7 = "Through zip/rar files obtained from a third party."

In the interpretation phase of the graph in Figure 4, the centers with red crosses and blue dots constitute the majority of the answers. The points where the majority are present are examined and the data is recorded. When Figure 4 is examined, it can be seen that people with 0-3 and 3-5 years of experience are mostly grouped in the fourth answer. This means that people who have just started working life and have little experience generally choose the option number 4, "As a result of browsing harmful sites". People with experience between 0-3 years may not have checked the HTTPS (Hypertext Transfer Protocol Secure) on the sites they visit, or they may not have checked the reliability of any site they do not know, even if it has HTTPS. While browsing these sites, people may have clicked on an ad or downloaded an application, file, etc. They may have downloaded. For this reason, they may have caused malicious software to be installed on the computer, their cookies to be stolen, and their personal information to be stolen. In this case, it is concluded that people with little experience should be careful while surfing the Internet. For this reason, companies should raise awareness among their employees on this issue. People should be given training and seminars about safe internet browsing. Companies can prepare traps so that people can learn about the event by allowing them to experience the event. In the final stage of my study, these issues are mentioned among the actions that need to be taken.

When the data is examined in detail, it can be seen that people with less experience mostly choose the "I don't know" option. This is an indication that people with little experience act unconsciously. This process is also done based on years of experience and age. Detailed representations are also available for review.

A variation of the same situation is observed in people with more years of experience. It can be seen that similar cyber incidents occur as a result of applications downloaded from websites (number 6). Even though the site is safe, you should not download it. After downloading, an inactive virus may enter the computer and spread across the network, leaving the door open. Therefore, one should acquire the habit of being careful while surfing the Internet. For the next analysis, parameters were changed, and the information about whether individuals have received cybersecurity training was analyzed. As seen in Figure 5.a, when looked at in general, the number of those who have received training is observed to be low. Especially among individuals with less experience, the number of those who have received training is observed to be low. The graph and data in Figure 5.a have been examined. The question asked is whether they have received cybersecurity training before, and it consists of yes/no answers. When these answers are coded, resulting in 1 and 0, it is noticed that the green and blue groups only consist of 1s and 0s.

Since the dataset does not contain complex responses, the use of the Mean Shift algorithm is not appropriate. When the dataset is processed with the K-means algorithm, a correct result is obtained.

As seen in Figure 5.a, the algorithm has created 2 groups. The formed groups are divided into individuals with 0-5 years and more than 5 years of experience. After making general interpretations, a detailed examination can be conducted to obtain a more accurate result. Individuals with experience levels of 0-3 years and 3-5 years (numbers 1 and 2) show a high proximity to zero. These individuals pose a risk to the company. Additionally, when this result is combined with the information seen in Figure 4, it is observed that individuals with less than 5 years of experience often respond 'I don't know' to the question of whether they have experienced a hacking incident before. If this information is combined with not having received cybersecurity training, companies should consider providing cybersecurity training from the beginning based on the experience years of new or existing employees. If we examine Group 2, it is observed that this ratio is halved. Detailed examinations will be conducted in the later stages of the study. However, in general, regardless of the years of experience, basic cybersecurity awareness training should be provided to every individual. In the later stages of the study, when creating a cyber risk matrix, the lack of cybersecurity awareness training is emphasized as a significant risk.

In this study, it was aimed to learn whether individuals who answered the survey check if HTTPS is used on the websites they visit. In Figure 5.b, individuals received responses indicating that they have been attacked during internet browsing. In this context, when Figure 5.b is examined, the

likelihood of encountering such a graph is high.

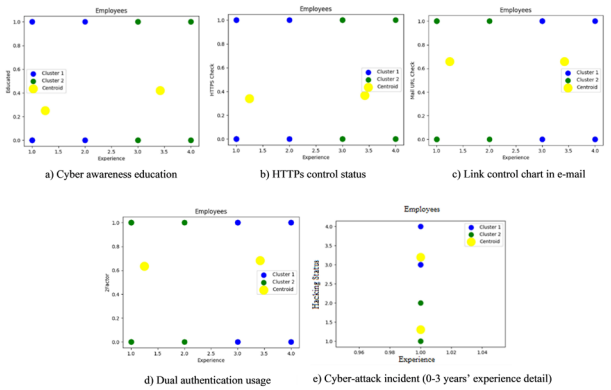

Figure 5. Cyber awareness education graph.

Regardless of experience, it is observed that HTTPS checking is very limited. The responses given by individuals, where 0 means they did not check HTTPS usage, and 1 means they checked it. Observations reveal that the central weight is closer to zero, indicating a deficiency in HTTPS checking among survey participants. In this case, there is a high probability that individuals may enter fake websites on the internet and expose their information to theft.

Recently, the increasing number of people falling into traps confirms this graph. In a news article published in 2023 on the Milli Gazete news site, it was announced that a fake site and application belonging to a popular retail chain were created [6]. The website of this retail chain has been completely copied. Ads and SEO (Search Engine Optimization) adjustments have been made to appear at the top of search engines. When searching for this retail chain on the internet, this fake site appears. Without link and HTTPS checking, there is a high probability of falling into such traps.

Another control method is one of the issues used in Figure 5.c and requires attention. Phishing attacks are a type of cyber-attack that uses disguised email as a weapon [7]. Varieties of phishing attacks use techniques such as text messages, voicemails, or QR (Quick-Response Code) codes. These attacks use social engineering techniques to convince the email recipient that the message is something they want or need (such as a request from a bank).

Referring to a blog post published by Josh F. on the CSO website, it is emphasized, especially for individuals playing a significant role in the company, to check the extensions and links in incoming emails [7]. Many people have fallen victim to phishing attacks that resulted in the theft of their information. Phishing attacks are a matter that companies pay attention to and warn their employees about.

Being cautious and ensuring control in this regard is an expected action from individuals [12].

Incoming links, for example, may come with different domains like g00gle.com instead of google.com. Redirection can also be done through a completely different link. Although a result of around 0.7 is generally obtained for both groups, raising it to 0.8 or even 0.9 levels is necessary for complete security.
The graph regarding the use of two-factor authentication is given in Figure 5.d. Individuals, regardless of their years of experience, mostly actively use two-factor authentication. In this regard, even if individuals' information is stolen, attackers will not be able to gain access unless authorized from their personal devices or applications.

2FA (Two-factor authentication) is an authentication technique that requires users to provide different forms of identification (such as fingerprint verification) and prevents access to their accounts until the password is entered. Using two-step authentication enhances the security of accounts and reduces the likelihood of password theft, decreasing the chances of unauthorized access by attackers. 2FA allows organizations to protect themselves more effectively against phishing attacks and vulnerabilities resulting from human error [8].

2FA can be seen as an additional method that prevents attackers from using stolen information through social engineering, phishing attacks, etc. Hence, the usage of 2FA is crucial, and it proves beneficial in applications, email logins, accounts, etc. [10].

The high usage rate of 2FA is observed due to applications compelling users to use it. Whether using phone applications, SMS (Short Message/Messaging Service), Microsoft Authenticator, etc., even if attackers capture the data, they cannot access users' systems without the code or approval from the users' phones [11].

The next check concerns the question of how often users change their passwords, as shown in Figure 6. When there are more than two answers to this question, representation should be made using Mean Shift. After entering parameters such as age and years of experience, the information about the password change interval, which is the other data to be measured, is used.

In the graph in Figure 6, the X-axis represents years of experience, the Z-axis represents age, and the Y-axis numbers indicate individuals' responses. The responses are sorted as follows: 1 = "Every 1-3 months," 2 = "Every 3-6 months," 3 = "Once a year," 4 = "I don't change it unless required."

Upon examining the graph in Figure 6, it can be observed that individuals with less than 5 years of experience are concentrated in the third option. This implies that individuals mostly change their passwords once a year. Individuals with more than 5 years of experience are seen to change their passwords every 3-6 months, which is a better practice compared to those with less than 5 years of experience. According to research, users changing their passwords every 1-3 months is considered appropriate. However, individuals with less than 5 years of experience changing their passwords only once a year pose a risk for companies.

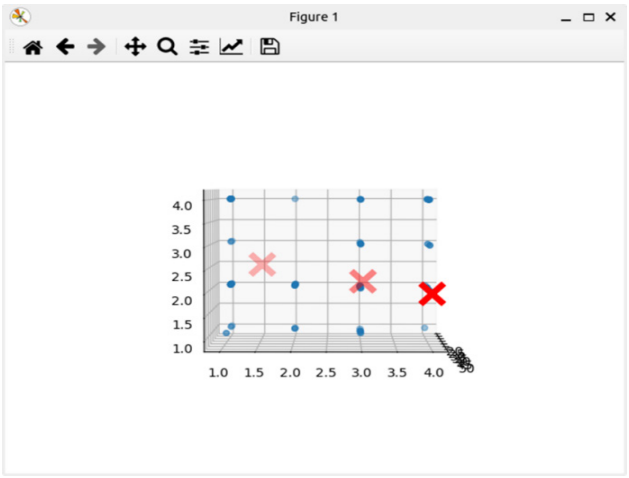

Figure 6. Password change frequency chart.

If individuals use the same password for all their accounts, and if one account is compromised, there is a high probability that other accounts will also be compromised. Each account should have a unique password; for example, the password for Facebook should not be the same as the work password or the mobile banking password [9]. The benefits of changing passwords frequently are as follows:

Prevents continuous access: A hacker may attempt to access your account multiple times within a specific period. Changing your password frequently reduces the risk of the attacker gaining access [9].

Prevents the use of compromised passwords: If you lose or change your devices, someone else might gain access to your passwords. Regularly updating your passwords means that even if an attacker finds an old or compromised password, it will no longer be useful, and your data will be secure [9].

Blocks access obtained by keyloggers: A keylogger is a surveillance technology used to record keystrokes, often used to steal login credentials along with credit card information. Changing your password regularly reduces the likelihood of passwords obtained in this way being useful over any period [9].

Attackers attempting to crack passwords through brute force can easily access user systems when user information is leaked on the internet. Individuals who do not change their passwords frequently are more likely to have their passwords stolen, posing a significant security threat for both users and organizations.

As mentioned at the beginning of this section, all these data and graphs have been examined in a general context so far. All the graphs examined up to this point include a common evaluation of individuals of all experiences and ages. While the used data reflects reality, it can affect each other in detail. For example, looking at Figure 3, it can be seen that the center of gravity of the blue group shifts to the left. In this case, the reason for the shift in the graph is the higher number of individuals with 0-3 years of experience in Group 1. The conclusion to be drawn from this is that individuals with 3-5 years of experience should also be examined separately. The graph in Figure 5.e has been created in detail, focusing only on individuals with 0-3 years of experience. When comparing Figure 5.e with Figure 3, the difference between individuals with 0-3 years and 3-5 years of experience is evident.

As a result, all data and parameters were examined. These reviews are kept on a general and detailed basis in a separate table. A lot of testing and detection has been done. The data obtained from these graphs were compared with each other and connected, and outputs were prepared for the next step, which is to create a risk matrix. These tables and outputs will be discussed in detail in the next section.

GRAPHICS IN DETAIL

The analyzes in the graphics below were used for the detailed part of the matrix. Detailed graphs were created for each question type and the resulting points were shown in the matrix.

In Figure 7, the cyber awareness training status of employees was measured in detail. For employees with 0-3 years of experience, results of 0.2, for employees with 3-5 years of experience, results of 0.4, for employees with 5-10 years of experience, results of 0.5, for employees after 10 years of experience, results of 0.4 were obtained.

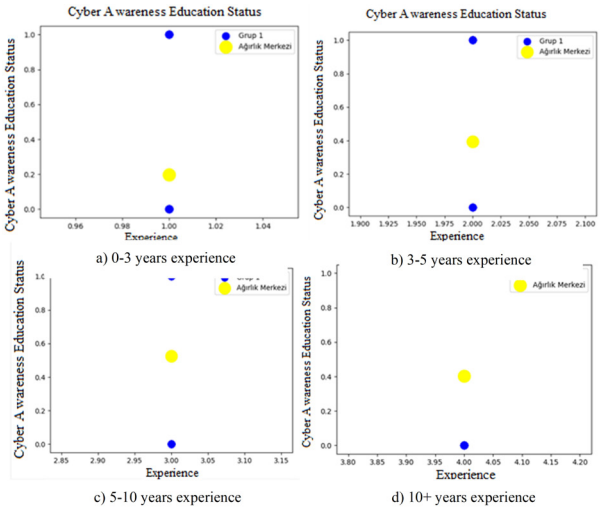

Figure 7. Cyber awareness education status (0-3 years' experience detail chart).

In Figure 8, the HTTPS control status of the employees is measured in detail. For employees with 0-3 years of experience, results of 0.2, for employees with 3-5 years of experience, results of 0.5, for employees with 5-10 years of experience, results of 0.5, for employees after 10 years of experience, results of 0.2 were obtained.

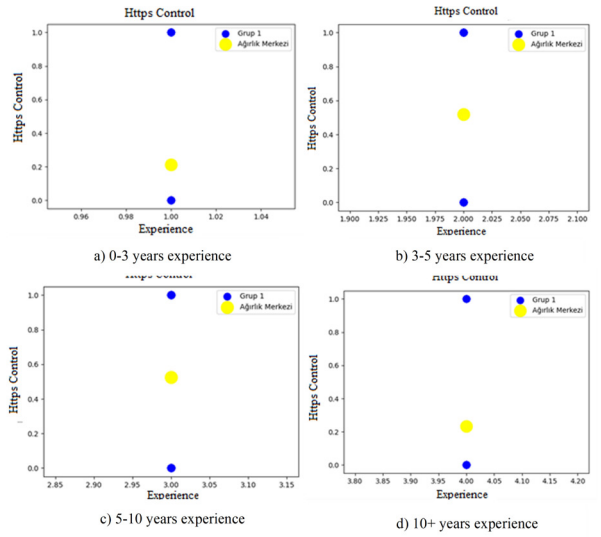

Figure 8. HTTPS check status

In Figure 9, the e-mail url control status of the employees is measured in detail.

For employees with 0-3 years of experience, results of 0.6, for employees with 3-5 years of experience, results of 0.6, for employees with 5-10 years of experience, results of 0.8, for employees after 10 years of experience, results of 0.5 were obtained.

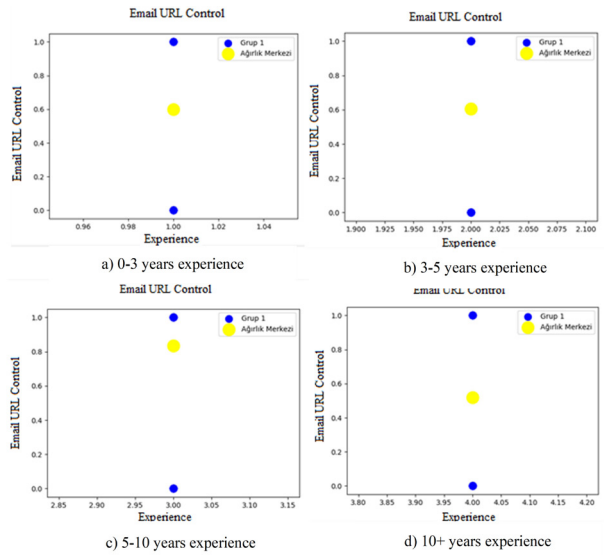

Figure 9. Mail url check status

In Figure 10, employees' 2FA usage is measured in detail. For employees with 0-3 years of experience, results of 0.6, for employees with 3-5 years of experience, results of 0.6, for employees with 5-10 years of experience, results of 0.8, for employees after 10 years of experience, results of 0.8 were obtained.

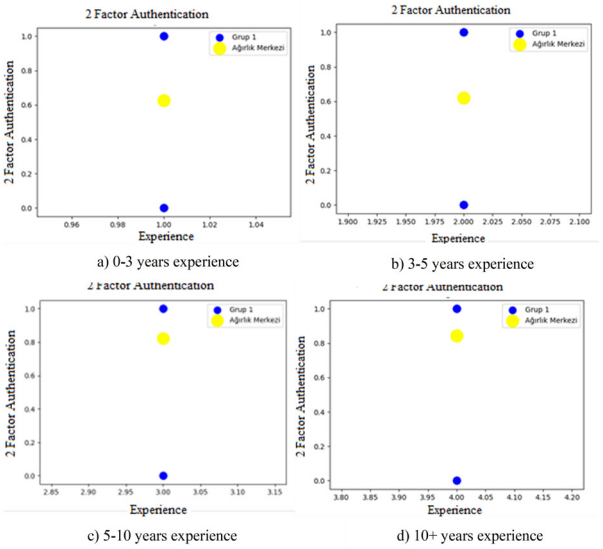

Figure 10. 2FA Usage Case (0-3 years' experience detail chart).

In Figure 11, the cyber incidents experienced by employees are measured in detail. For employees with 0-3 years of experience, results of 1.2 and 3.1, for employees with 3-5 years of experience, results of 1.9 and 3.3, for employees with 5-10 years of experience, results of 2.5 and 6, for employees after 10 years of experience, results of 2.2 and 5.1 when looking at the 2 centroids were obtained.

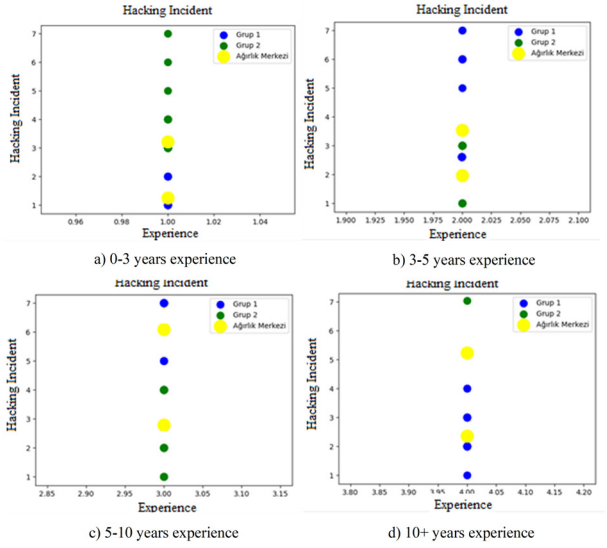

Figure 11. Hacking incident

In Figure 12, the frequency of employees changing their passwords is measured in detail. For employees with 0-3 years of experience, results of 1.7 and 3.8, for employees with 3-5 years of experience, results of 1.5 and 4, for employees with 5-10 years of experience, results of 1.6 and 3.3, for employees after 10 years of experience, results of 1.7 and 3.6 when looking at the 2 centroids were obtained.
These will be used in the risk matrix.

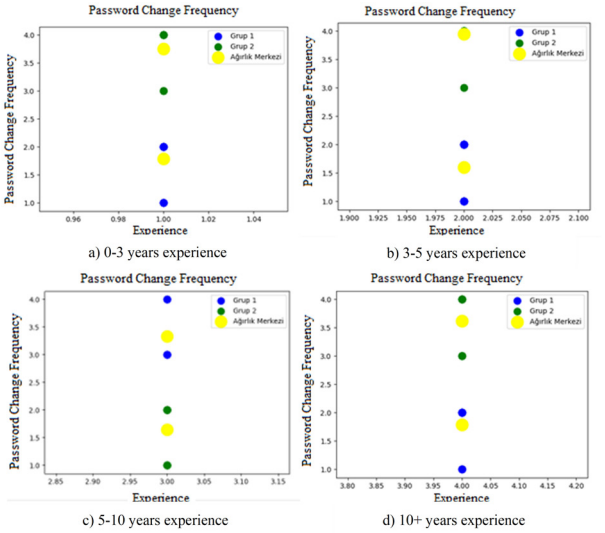

Figure 12. Password change frequency

In Figure 13, employees' password storage method is measured in detail. For employees with 0-3 years of experience, results of 1.3 and 3.2, for employees with 3-5 years of experience, results of 1.8 and 3, for employees with 5-10 years of experience, results of 1.8 and 3.2, for employees after 10 years of experience, results of 1.2 and 3.2 when looking at the 2 centroids were obtained.

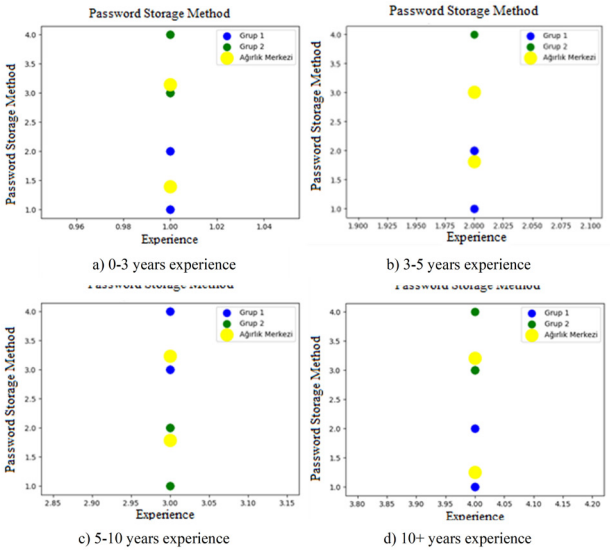

Figure 13. Password storage method

Creation of Risk Matrix and Actions

After the data set consisting of survey data was formatted, the data and algorithms were tested. After this, the algorithms run on real data were tested. Some of the reviews and comments are described in the previous topic. However, all of them were carried out and the results obtained as a result of the algorithm are stored numerically in Table 1. The data collected in this way were compared with each other by looking at the table prepared on a general and detailed basis.

Table 1. General and detailed algorithm results.

	General							
Field/ Year	**0-3**		**3-5**		**5-10**		**10+**	
1	0.3		0.3		0.4		0.4	
2	0.2		0.2		0.4		0.4	
3	0.3		0.3		0.4		0.4	
4	0.7		0.7		0.7		0.7	
5	0.6		0.6		0.7		0.7	
6	4.0		4.0		4.0		6.0	
7	2.5		2.5		2.0		1.5	
8	2.5		2.0		2.5		1.0	
	Detailed							
Field/ Year	**0-3**		**3-5**		**5-10**		**10+**	
1	0.2		0.4		0.5		0.4	
2	0.2		0.5		0.5		0.2	
3	0.6		0.6		0.8		0.5	
4	0.6		0.6		0.8		0.8	
5	0.6		0.8		0.8		0.7	
6	1.2	3.1	1.9	3.3	2.5	6	2.2	5.1
7	1.7	3.8	1.5	4	1.6	3.3	1.7	3.6
8	1.3	3.2	1.8	3	1.8	3.2	1.2	3.2

The fields in Table 1 and their meanings are as follows.

1. Cyber awareness training.
2. HTTPS control.
3. Mail URL control.
4. Use of dual verification.
5. KVKK Information
6. Cyber incident.
7. Password change frequency.
8. Password storage method.

The aim of the study is to interpret the dataset. Based on these interpretations, it seeks to identify under which conditions risks arise and what actions need to be taken. Depending on the company's needs, survey questions and actions may vary. The algorithms can be rerun with modified versions, and new actions and matrices can be determined. However, the established questions have been prepared based on specific research results and with the approval of experts in the field. These questions are sufficient as they are value-adding and universally applicable. Additionally, since the survey participants are not from a single company or profession, the questions are suitable for general use. In short, the conducted study is general, making it effective for any company.

The generated cyber risk matrix differs from matrices that only involve technical information and do not consider human behaviors. Typically, a cyber risk matrix involves a technical examination. In the matrix created for the study, individuals' potential cyber risks based on years of experience are illustrated. For example, it has been observed that individuals with more than 10 years of experience prefer using a notepad as a password storage method. The level of cyber risk posed by these individuals in terms of password storage is

determined to be high.

The data in Table 1 encompasses the results of detailed and general studies conducted as a result of the algorithm. When these questions and answers are examined, it is possible to observe similarities within certain groups. Following this observation, general headings have begun to be created for the cyber risk matrix. In some cases, a title is associated with two questions, while in other cases, it is associated with a single question.

Speaking of titles, the first heading is "Cyber Education." This heading pertains to individuals' basic cybersecurity education status. The second heading is "Cyber Inquiry." This heading includes individuals' HTTPS checks on the sites they visit and the inspection of attachments and links in emails. It indicates whether individuals have the ability to perform cyber inquiries. The third heading is "Password Protection." This heading concerns how individuals store their passwords. The fourth heading is "Password Change." This heading indicates the frequency with which individuals change their passwords and the importance of changing passwords frequently. The fifth heading is "Additional Measures." This heading covers the additional applications, password creation, protection measures, extra plugins, etc., used by individuals for protection in the online environment. The sixth heading is "Legal Authority." This heading encompasses individuals' knowledge of GDPR, procedures to follow in the event of a cyber-attack, and generally their knowledge of legal procedures. After determining the titles and domains of impact, a matrix has been created. Under these headings, individuals were separated by years of experience and added to the matrix. When adding data to the matrix, the structure in Table 2 was created by starting from a less risky level and increasing the risk level downward.

The numbering of the areas determined according to Table 2 is as follows:
1. Cyber awareness training.
2. Cyber interrogation awareness.
3. Password protection.
4. Password change frequency.
5. Additional measures.
6. Legal dominance.

Table 2. Cyber risk matrix.

Field/ Year	0-3 Year	3-5 Year	5-10 Year	10+ Year
6	Low	Low	Low	Low
5	Low	Low	Low	Low
4	Medium	Medium	Low	Low
3	Medium	Medium	Low	High
2	Medium	Medium	Medium	High
1	High	High	High	High

Examining the cyber risk matrix in Table 2, if we focus on the first heading, which is cybersecurity education, it is observed that the risk is high in all individuals regardless of years of experience. Therefore, for the first heading, which is cybersecurity awareness training, it has been indicated that the cyber risk is high regardless of years of experience. In this case, basic cybersecurity awareness training must be provided to everyone entering the company, regardless of years of experience.

Looking again at the cyber risk matrix in Table 2, interpretation has been made for the second heading, which is cyber inquiry. For this heading, when looking at individuals with more than 10 years of experience, the cyber risk is very high. When examining the graph in Figure 10, especially for individuals with more than 10 years of experience, the center of gravity has gathered around answer one. It is observed that these individuals store their passwords in a notepad. Therefore, individuals with more than 10 years of experience will pose a risk to the company. For individuals with other years of experience, the risk is at a moderate level.

Actions that companies should take for new employees or existing employees with more than 10 years of work experience are as follows: These individuals should be recommended password storage applications. The use of these applications can be taught, and the importance of storing passwords can be emphasized. Since this topic may be risky for individuals with more than 10 years of experience, it is necessary to be instructive and guiding to these employees. The same situation applies to individuals with a moderate risk level. However, high priority should be given to employees with more than 10 years of experience or new employees. The titles in the risk matrix and the precautions to be taken for these titles are as follows.

General cyber awareness training should be provided. People are informed about what may happen as a result of cyber-attacks, past individual or corporate cyber events, etc. should be informed about the issues and their importance should be emphasized.

Awareness should be raised among the relevant people with examples of what every action taken in the field of cyber interrogation, a site visited, an e-mail received, a file downloaded from the internet, or a link clicked, can lead to. In addition, they should be informed about how they can check this issue and what they should pay attention to. People should be trained on password protection. People should be informed about what might happen if they fail to keep their passwords well. Encrypted applications used worldwide to store passwords should be mentioned and the use of these applications should be encouraged. Advice should be given about changing existing passwords and switching to these applications.

Regarding changing passwords, people should be explained what might happen if they do not change their passwords. If people do not change their passwords, the methods used by attackers to obtain passwords should be mentioned. Additionally, applications that can be used when creating a password should be shown and their use should be encouraged. The points to be taken into consideration to create the correct password should be shown. Passwords must contain at least 1 numeric

character and 1 special character, and employees must be informed about creating and using complex passwords.

As additional precautions, add ad blockers, HTTPS enforcement, trusted link checking, etc. to the browsers used. Plugins and applications that will perform the operations should be mentioned. The use of these applications and plug-ins should be encouraged within the company.

People should be informed about what they can do legally. Information about KVKK should be given. People's rights should be taught. You should be taught who should be notified of this incident and what procedures should be followed in case of cybercrime occurring inside and outside the company.

CONCLUSION

This study focuses on addressing the human factor, which is a significant vulnerability source in the field of cybersecurity. The goal of the study is to create risk profiles based on the behaviors of employees within the company and develop effective measures accordingly. The findings obtained through the use of machine learning tools provide a valuable resource for strengthening companies' cybersecurity strategies.

The main focus of the study is to categorize employees into specific groups using K-means and Mean Shift algorithms. The aim is to identify similar behaviors within these groups and determine a common action. The risk matrix derived from combining the obtained groups with parameters such as age and experience provides companies with a better understanding of cybersecurity risks, enabling them to develop strategies accordingly.

This study offers an approach that goes beyond the technical aspects of preventive measures in the field of cybersecurity by addressing the human factor. The risk matrix created based on employee profiles provides companies with a clear perspective on potential risks in specific departments or age groups, helping them generate customized solutions.

The methodology presented in this study is applicable to companies, schools, government agencies, and even individual lives. Actions are adaptable based on the needs of legal entities or organizations. Surveys can be re-administered based on specific institutions, and new results can be obtained by running algorithms with this information. This allows for the creation of customized matrices and actions for more effective use.

In conclusion, this study offers a comprehensive approach that not only limits cybersecurity to technical measures but also focuses on employee behaviors. By adopting this methodology, companies can optimize their cybersecurity strategies more effectively and comprehensively. Future research is recommended to further develop this approach by integrating more data sources and exploring new algorithms.

References

1. ENISA. (2020, June 4). Threat landscape 2020: Cyber attacks becoming more sophisticated, targeted, widespread and undetected. European Union Agency for Cybersecurity. Retrieved from https://www.enisa.europa.eu/news/enisa-news/enisa-threat-landscape-2020
2. The Hill. (2020, March 13). FBI sees spike in cyber crime reports during coronavirus pandemic. Retrieved from https://thehill.com/policy/cybersecurity/493198-fbi-sees-spike-in-cyber-crime-reports-during-coronavirus-pandemic/
3. Rajasekharaiah, K. M., Dule, C. S., & Sudarshan, E. (2020, December). Cyber security challenges and its emerging trends on latest technologies. IOP Conference Series: Materials Science and Engineering, 981(2), 022062. https://doi.org/10.1088/1757-899X/981/2/022062
4. Tirumala, S. S., Sarrafzadeh, A., & Pang, P. (2016). A survey on internet usage and cybersecurity awareness in students. In 2016 14th Annual Conference on Privacy, Security and Trust (PST) (pp. 223-228). IEEE. https://doi.org/10.1109/PST.2016.7906931
5. Avcı, Ü., & Oruç, O. (2020). Üniversite öğrencilerinin kişisel siber güvenlik davranışları ve bilgi güvenliği farkındalıklarının incelenmesi. İnönü Üniversitesi Eğitim Fakültesi Dergisi, 21, 284-303. https://doi.org/10.17679/inuefd.526390
6. Yiğit, M., & Seferoglu, S. S. (2019). Öğrencilerin siber güvenlik davranışlarının beş faktör kişilik özellikleri ve çeşitli diğer değişkenlere göre incelenmesi. Mersin Üniversitesi Eğitim Fakültesi Dergisi, 15, 186-215. https://doi.org/10.17860/mersinefd.437610
7. Yetgin, M., & Karakaya, A. (2020). Karabük Üniversitesi çalışanlarına yönelik kişisel siber güvenlik üzerine araştırma. Kahramanmaraş Sütçü İmam Üniversitesi İktisadi ve İdari Bilimler Fakültesi Dergisi, 10. https://doi.org/10.47147/ksuiibf.816171
8. Gündüz, M., & Das, R. (2022). Kişisel siber güvenlik yaklaşımlarının değerlendirilmesi. DÜMF Mühendislik Dergisi. https://doi.org/10.24012/dumf.1122997
9. Tokmak, M. (2023). Öğrencilerin siber güvenlik farkındalık düzeylerinin makine öğrenmesi yöntemleri ile belirlenmesi. Yüzüncü Yıl Üniversitesi Fen Bilimleri Enstitüsü Dergisi, 28. https://doi.org/10.53433/yyufbed.1181694
10. Çam, H., Aslay, F., & Özen, Ü. (2019). Yükseköğretim kurumlarında bilgi güvenliği farkındalık düzeylerinin ölçümlenmesi. Yönetim Bilişim Sistemleri Dergisi, 5(2), 1-11.
11. Talesh, S. A. (2018). Data breach, privacy, and cyber insurance: How insurance companies act as "compliance managers" for businesses. Law & Social Inquiry, 43(2), 417-440. https://doi.org/10.1111/lsi.12303
12. Kenny, K. S., Merry, L., Brownbridge, D. A., & Urquía, M. L. (2020). Factors associated with cyber-victimization among immigrants and non-immigrants in Canada: A cross-sectional nationally-representative study. BMC Public Health, 20(1). https://doi.org/10.1186/s12889-020-09492-w
13. Tempestini, G., Rovira, E., Pyke, A., & Nocera, F. D. (2023). The cybersecurity awareness inventory (CAIN): Early phases of development of a tool for assessing cybersecurity knowledge based on the ISO/IEC 27032. Journal of Cybersecurity and Privacy, 3(1), 61-75. https://doi.org/10.3390/jcp3010005
14. Bergh, C. M. M. R. d., & Junger, M. (2018). Victims of cybercrime in Europe: A review of victim surveys. Crime Science, 7(1). https://doi.org/10.1186/s40163-018-0079-3
15. Pramoda, M., Pramoda, S., & Correa, Z. M. O. (2022). Luster regained: A novel cyber incident risk prediction model using

machine learning. International Journal of Scientific Research in Computer Science, Engineering and Information Technology, 1-19. https://doi.org/10.32628/cseit2283125

16. Nurse, J. R. C., Radanliev, P., Creese, S., & Roure, D. D. (2018). If you can't understand it, you can't properly assess it! The reality of assessing security risks in internet of things systems. Living in the Internet of Things: Cybersecurity of the IoT - 2018 (pp. 1-9). https://doi.org/10.1049/cp.2018.0001
17. Cains, M., Flora, L., Taber, D., King, Z. M., & Henshel, D. S. (2021). Defining cybersecurity and cybersecurity risk within a multidisciplinary context using expert elicitation. Risk Analysis, 42(8), 1643-1669. https://doi.org/10.1111/risa.13687
18. Kumar, A., & Singh, R. (2019). A review of K-means clustering algorithm and its applications. International Journal of Computer Applications, 178(24), 1-5. https://doi.org/10.5120/ijca2019919558
19. Huang, C., & Wang, Y. (2019). A survey on mean shift algorithm and its applications. Journal of Computer Science and Technology, 34(1), 1-20. https://doi.org/10.1007/s11390-019-1906-0
20. Alkhalil, Z., Hewage, C., Nawaf, L., & Khan, I. (2021). Phishing attacks: A recent comprehensive study and a new anatomy. Frontiers in Computer Science, 3, 563060. https://doi.org/10.3389/fcomp.2021.563060
21. Hirshman, E., & Bjork, R. A. (1988). The generation effect: Support for a two-factor theory. Journal of Experimental Psychology: Learning, Memory, and Cognition, 14(3), 484–494. https://doi.org/10.1037/0278-7393.14.3.484
22. Aloul, F., Zahidi, S., & El-Hajj, W. (2009). Two-factor authentication using mobile phones. In 2009 IEEE/ACS International Conference on Computer Systems and Applications (pp. 641-644). IEEE. https://doi.org/10.1109/AICSSA.2009.5069395

HITTITE JOURNAL OF SCIENCE AND ENGINEERING

e-ISSN: 2148-4171
Volume: 12 • Number: 1
March 2025

Investigation of the Effect on Thermal Performance Using Organic Phase Change Material in Battery Cooling Systems

Mustafa Yasin Gökaslan
Van Yüzüncü Yıl University, Department of Mechanical Engineering, Van, Türkiye.

Corresponding Author

Mustafa Yasin Gökaslan
E-mail: my.gokaslan@yyu.edu.tr Phone: +90 542 217 47 28 Fax: +90 432 225 1730
RORID: https://ror.org/041jyzp61

Article Information

Article Type: Research Article
Doi: https://doi.org/10.17350/HJSE19030000347
Received: 18.11.2024
Accepted: 14.01.2025
Published: 25.03.2025

Cite As

Gökaslan MY. Investigation of the Effect on Thermal Performance Using Organic Phase Change Material in Battery Cooling Systems. Hittite J Sci Eng. 2025;12(1):15-23.

Peer Review: Evaluated by independent reviewers working in at least two different institutions appointed by the field editor.
Ethical Statement: Not available.
Plagiarism Checks: Yes - iThenticate
Conflict of Interest: Authors declare no conflict of interest.

CRediT AUTHOR STATEMENT
Mustafa Yasin Gökaslan: Conceptualization, Data curation, Formal Analysis, Investigation, Methodology, Resources, Supervision, Writing – review and editing.

Investigation of the Effect on Thermal Performance Using Organic Phase Change Material in Battery Cooling Systems

Mustafa Yasin Gökaslan

Van Yüzüncü Yıl University, Department of Mechanical Engineering, Van, Türkiye.

Abstract

The thermal performance of lithium-ion battery under passive cooling (organic PCM) is investigated experimentally. Coconut oil, soy wax and palm wax are used as organic PCM. This study investigates the temperatures at the anode, cathode and midpoint of the battery in natural convection and the effects of passive cooling method on three different organic PCMs located around Li-ion battery during different discharges (1C, 2C and 3C). The results with PCM are also compared with the cases without PCM and the effects of organic PCMs on battery thermal performance are determined. According to the experimental results, it is determined that at the highest discharge rate, coconut oil completely melted, palm wax is in mushy phase region and soy wax does not change phase. Depending on discharge rates, in the case without PCM, while the maximum battery surface temperatures range from 30.7 °C to 48.8 °C, these temperatures range from 25.5 °C to 42.6 °C for coconut oil, 24.8 °C to 41.8 °C for soy wax, and 25 °C to 40.5 °C for palm wax. Battery cooling performance is better in palm wax. In addition, when the surface temperatures of the battery are compared with organic PCMs temperature, it is identified that there is very little difference. These findings indicate that passive cooling can also reduce battery operating temperature and the use of organic PCMs can make positive contributions to battery thermal performance.

Keywords: Organic-PCM, Lithium-ion battery, Thermal Behavior, Passive cooling system.

INTRODUCTION

The importance of energy and its effective use have been one of the most important issues in engineering applications in recent years. The energy required in our daily lives is obtained from renewable or non-renewable energy sources. Renewable energy sources come to the fore due to factors such as the unstable prices of fossil-based energy, lack of confidence in supply and the reduction of CO_2 emissions. One of the most important problems in both renewable and non-renewable energy sources is that energy cannot be stored. Batteries are used to store energy and provide energy in areas that are not accessible. Studies on the chemical, electrical and thermal properties of batteries are still ongoing. Batteries can be divided into two groups, rechargeable and non-rechargeable, depending on their usage areas and capacities. Among rechargeable batteries, the most preferred battery type is Lithium-ion. These batteries are widely used in the automobile-bicycles, household electrical appliances, electronics and aviation industries due to their high efficiency, operating temperature, long life, capacities and low self-discharge rate [1–3]. Capacity is important in batteries used in these devices, and it shows the energy a battery will store and how long it can provide energy at certain discharge currents. However, factors such as ambient temperature, operating current or voltage, discharge rate and sensitivity of the devices directly affect the capacity of the batteries, depending on the battery life. The operating temperature of the battery is an important factor in meeting battery life cycle and power requirements. The operating temperature of the battery is a critical that directly affects its electrical properties such as battery life, capacity and power. Although this undesirable operating temperature is considered as high temperatures, it also negatively affects the battery at operating temperatures below zero [4]. In addition, when the critical temperature is exceeded, it becomes dangerous and unsuitable [5,6]. In this context, depending on the battery characteristics, if it is operated at high currents, the battery temperature is higher depending on the ambient temperature. Cooling is applied to the battery to control the temperature increase of the battery. It is possible to cool the battery in different ways: natural convection, forced convection, coolant circuit, heat pipe, Phase change material (PCM) and hybrid system [7].

PCM stores thermal energy with internal energy of material with temperature change and can transfer this energy to the environment. It is applied in many areas such as textiles, building heating and cooling, cooling of electrical/electronic parts [8]. PCMs can be divided into three groups: organic, inorganic and eutectic. Organic PCMs have properties such as high latent heat of fusion, chemical stability, corrosion resistance and low undercooling. It is possible to classify organic PCMs into two groups: paraffin and non-paraffin. Non-paraffin organic PCMs are preferred in systems operating close to ambient temperature (10-40°C) [9]. Organic PCMs such as paraffin have a negative impact on the environment. Because, paraffin which is petroleum based is toxic to the environment [10]. However, as environmentally friendly bio-based (vegetable oils) organic PCMs, fatty acids are sustainable, non-corrosive and environmentally friendly [10]. Thermophysical properties are investigated depending on the organic PCM cycle in thermoelectric cooling and heating system. While the melting and enthalpy of palm wax remained almost the same depending on the PCM cycle, these values varied in soy wax [11].

Organic PCMs are used in construction materials, heating and cooling systems, etc., and have positive effects. [12–16]. The effect of organic PCMs on thermal management when used as passive cooling in batteries is also among the research topics. However, the application of PCMs in battery cooling is limited due to poor thermal performance, leakage of liquid PCM and challenging temperature control after melting temperatures [17]. However, the most important advantage of PCM is that it does not consume extra power.

Abdulmunem et al. studied the thermal analysis of bio-based PCMs used in lithium-ion battery cooling. The authors used cheap, sustainable and widely available palm fatty acid distillate as PCM. They showed that when bio-based PCM is used in battery cooling, the temperature of the battery is reduced by 10 to 20% and the electrical power is increased

by 17 to 43%[18]. Verma et al. investigated the thermal performance of battery in capric acid (PCM) with different thicknesses. The authors investigated the temperature effect of capric acid on battery discharge at two different ambient and compared the results with commonly used paraffin. The capric acid optimum thickness is 3 mm and provides the best cooling performance [19]. John et al. researched the effect of Stearic Acid (organic PCM) which is non-corrosive and has high latent heat, on battery cooling. The authors simulated PCMs with different PCM thicknesses and different amounts of copper oxide (CuO) nanoparticles to optimize. Addition of 4% CuO is the cooling critical value of PCM, above which adding CuO has no effect on the battery temperature decrease. PCMs with phase change temperatures between 310 K and 330 K are much more effective in battery cooling [20]. Ling et al. developed the encapsulated inorganic PCM-sodium acetate trihydrate and studied the thermal performance of this PCM in battery cooling. Expanded graphite is added to improve the thermal conductivity of this PCM. The Authors claimed that the PCM they obtained is not flammable and even protected the battery from thermal runaway and is safer [21]. Goud et al. researched the thermal performance of battery packs using Myristyl alcohol PCM. This PCM provided maximum temperature reductions of approximately 22 to 35%, depending on discharge rates. Passive cooling with Myristyl alcohol is also safe and effective at high discharge rates [22]. Yazıcı studied passive thermal management using PCM/graphite matrix in the battery pack. The temperature changes of the battery in PCM/graphite matrix were evaluated by thermal images, discharge capacity and energy capacity. Graphite PCM increases thermal conductivity by 35 times. Compared to air cooling, while the operating temperature and temperature gradient along the surface of the battery are reduced by 22% to 43%. The energy capacity and operating time are increased compared to natural convection for high discharge rate [23]. Sinha et al. examined the thermal properties of the battery in different terminal designs of prismatic batteries with and without liquid biocompatible phase change material. The authors stated that the counter-flow designed structure has a more homogeneous temperature distribution than the parallel designed terminal. Authors found that there were decreases in maximum temperature values between 6.23% and 12.44% in different currents due to the use of PCM. The authors stated that the use of PCM provides a more uniform decrease in voltage in the discharge states of the batteries, which can increase the performance and life of the battery [24]. Mei et al. used the composite PCM to reduce the thermal runaway of batteries. Authors stated that heating the battery caused high temperature and bright flam. Then, the burning of paraffin increased the duration of a stable flame and concluded that sodium acetate trihydrate efficaciously prevented the burning of paraffin and reduced the burning time by 40.5% [25].

In this experimental study, the effect of organic PCMs which are abundant in nature, have low corrosion effect and biocompatible [26,27] on battery thermal performance is investigated. Palm wax, soy wax and coconut oil are used as organic PCMs. The distance between the battery box and the battery is designed to be at least 2 mm. The battery box is selected as the rectangular prismatic and the battery is placed inside. The battery surface temperature, anode, cathode region temperature, PCM temperature and ambient temperature are measured at three different discharge currents. The changes in these temperatures in the battery box with and without PCM are examined. In cases without PCM, the temperatures of the anode, cathode and midpoints of the battery are measured at different discharge rates and the temperature differences are determined. Because the thermal performance comparison of the organic PCMs, it is taken into consideration that the initial temperatures of the experiments are almost the same. The purpose of this study is to reveal the thermal performances of organic PCMs in wax form in battery cooling.

EXPERIMENTAL STUDY

Materials Preparation

In battery cooling systems, 3 different methods are generally used: active, passive and hybrid. While air or fluid cooling is generally used in active systems, Heat pipe and PCM are used in passive cooling. Hybrid systems are used in both active and passive systems are used together. These cooling systems may vary depending on the place of use and cooling capacity. In this experimental study, the PCM method, which is one of the passive cooling applications, is examined. It is quite preferred because it does not consume additional power for cooling. Inorganic PCMs or paraffin are used in battery applications due to their high heat capacity. However, organic PCMs are also preferred in many studies due to their low cost, accessibility and recyclability. The effect of 3 different organic PCMs which are coconut oil (CO), palm oil wax (PW) and soybean oil wax (SW) on battery thermal management is investigated

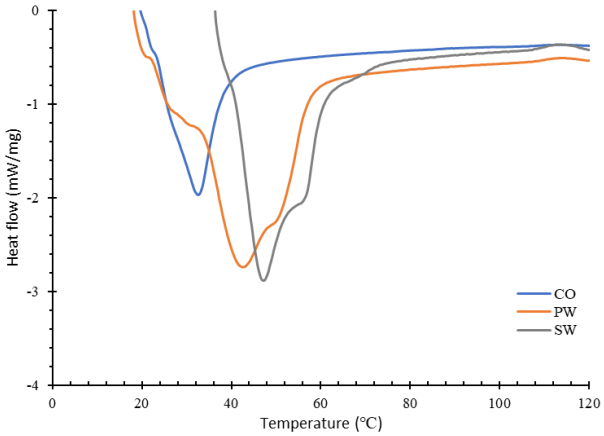

Figure 1. DSC of the organic (Bio-based) PCMs

Organic PCMs in the form of wax are melted and placed in the battery box in liquid phase. Then, the leakage between the battery box and the battery is checked. DSC results of the organic PCMs are given in Fig. 1. The melting behavior of organics PCMs is determined using DSC (Differential Scanning Calorimetry). During the melting times, only one endothermic peak is observed. Therefore, it is seen that the organic PCMs do not consist of eutectic (two or more) PCMs and the phase change temperature is constant values. Thermophysical properties of organic PCMs are given in Table 1.

Table 1. Thermophysical property of organic PCMs

Properties	Coconut oil	Palm wax	Soy wax
Melting Point (°C)	30	42	46
Density (kg/m³)	920 [28]	920 [29]	900 [30]
Latent heat (J/g)	103	135	160
Specific heat capacity (kJ/kgK)	1.55 [16]	2.64 [16]	2.7 [30]

It is seen that the melting temperature starts at the lowest coconut oil 30 °C and increases towards palm wax 42 °C and soy wax 46 °C. The highest density among the PCMs used in this study is soy wax. Latent heat is one of the important parameters to the thermal energy storage capacity of PCMs. It is possible to determine latent heat from the area under the heat flow and temperature curves. The latent heats are listed from lowest to highest as coconut oil, soy wax and palm wax.

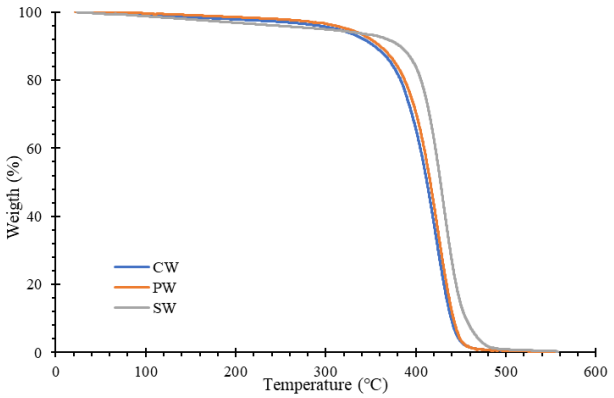

Figure 2. Mass losses of the organic PCMs during heating

In Fig. 2, the mass losses of the PCMs used in the experimental study during heating are given. The melting temperatures obtained from Fig. 1 show that there is a very small mass loss at the transition temperature from solid to liquid state. All three organic PCMs exhibit single-stage decomposition. While coconut oil and palm wax experience a high mass loss during the heating period between 320 and 460 °C, the high mass loss in soy wax is between 360 and 480 °C. This organic PCM may be losing mass due to low moisture content, moisture loss up to 320 °C for palm and coconut, and 360 °C for soy wax, or volatile substances. Because these Bio-PCMs are hydrophobic and have very low water retention capacity [31–33]. It has been observed that the organic PCMs used as battery cooling application reach a maximum temperature of 45 °C and the mass loss in the PCMs at these temperatures is approximately 0.2%. This value is negligible.

Battery Box (Test Chamber)

In this experimental study, the thermal performance of a cell (battery) placed inside the battery box is investigated in different C rates which is discharge currents. The battery is cylindrical with the diameter and height of 18 mm and 65 mm respectively. The battery is in the box and the dimensions of the battery box are 22x22x65 mm. The gap between the battery and the box is at least 2 mm as shown Fig. 3. The battery box is the hollow rectangular prism and it was produced from the 3-D printer. The volume occupied by the battery in the box is 14505 mm³. The total volume of the box is 27588 mm³ and the void volume (PCM) is 13083 mm³. Palm wax, coconut oil and soy wax are used as organic PCMs. The coconut oil placed in the battery box is 12 g, soy wax and palm wax are 15 g.

The battery box is made of 4 mm thick PLA (Polylactic acid) material. The battery box keeps the PCM inside and simplifies the PCM thickness. The thermal conductivity of PLA material is low. Some of the battery boxes used in the application are polymer-based materials. The battery box used in the experiments is given in Fig. 3.

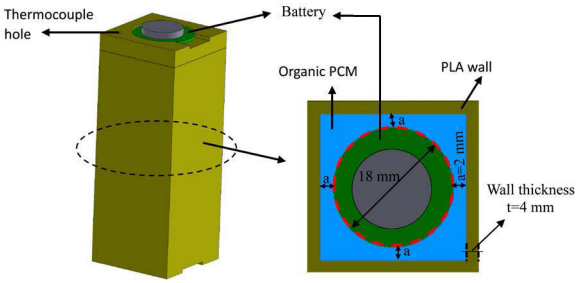

Figure 3. Battery box (Test chamber)

In the study, Orion brand 18650/22 (2200 mAh) model Lithium-ion battery is used. The nominal voltage of the battery used is 3.7 V, the highest voltage is 4.2 V, the cut-off voltage is 2.5 V and the standard capacity is 2200 mAh. The weight, power density and internal resistance of the battery used in the experiment are 45.5g, 8.14 Wh and 35 mΩ, respectively.

Experimental Setup

The battery experimental setup shown in Fig. 4 is established to investigate the effect of using different organic-PCMs on battery thermal performance. The battery experimental setup consists of DC power supply, electronic load, multi-channel temperature recorder, PC and thermocouples, the test chamber consists of the battery box, battery and PCM. The test chamber consists of a cell. The battery (cell) is placed and fixed inside the battery box with equal margins on each side and the anode end on top. DC power supply is used to charge the battery and electronic load is used to discharge it. Since it is a cell, the end of charge/discharge or cut-off voltage stated in the manufacturer's data sheet is not exceeded during charging and discharging. Thus, the battery is not exceeded for the discharge cycle without the need for BMS (Battery Management System) from the applications that cause the battery to be in an unwanted (dead state).

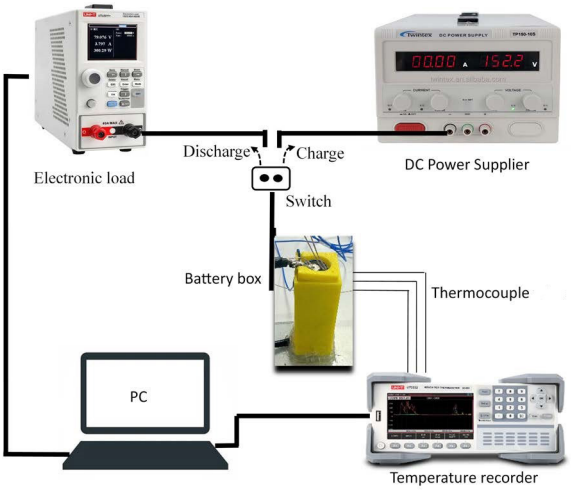

Figure 4. Battery experimental setup

Twintex brand TP150-10S model DC power supply is used to charge the battery. As recommended by the manufacturer, the battery is first current-limited and then voltage-limited to prevent exceeding 2200 mAh. Unit brand UTL8211+ model electronic load is used for battery discharge. Experiments are carried out in 3 different discharge ranges in the electronic load device, with constant current 1C, 2C, 3C discharge rate in the battery module.

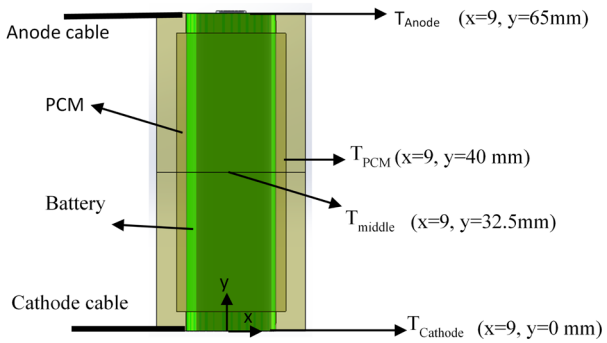

Figure 5. Thermocouple locations

In the experimental study, temperatures are measured from 5 different points, namely the middle, anode, cathode parts of the battery, PCM and ambient temperature. K type thermocouple is used in the experiments. The thermocouple location is given in Fig. 5. In the production of battery surface thermocouples, the thermocouple wires are welded to the surface with the thermocouple-welding device. Thus, it is aimed to minimize the contact resistance. The temperature of the organic PCM is measured from the middle point of the box and 2 mm away from the battery. The ambient temperature is measured approximately 30 cm away from the test chamber. While the temperature data is recorded at different discharge rates, temperature data are taken every second. Temperature data is transferred to the computer via the temperature recorder.

Uncertainty Analysis

Uncertainty analysis can be divided into two categories: measurements and calculations. In this study, there is no uncertainty in the calculations in this study. The measurement uncertainties in the battery experiment are the current and voltage values for both charging and discharging and temperature. The uncertainty of the DC power supply device is 100 mV for voltage and 10 mA for current. The uncertainty of the electronic load device is 0.05%+0.1%FS (full scale) for both current and voltage. The uncertainty of the K type thermocouple is ± 1°C. Therefore, the difference between the measured temperature and the uncertainty of this value is 1 °C. The measured electrical values and their uncertainty are comparatively low and can be neglected.

Governing Equations

The battery is composed of various chemical materials and has a layered structure. Due to this layered structure, the thermal conductivity is not the same in all directions and can be optimal if the battery is cooled differently from the poles or the middle. It is possible to define the physical problem as follows [34,35].

$$\rho c_p \frac{\partial T}{\partial t} = k_b \nabla^2 T + q_{gen} \quad (1)$$

The heat emitted by the battery can be divided into two: the heat resulting from electrochemical reactions and the heat resulting from the battery's internal resistance to current flow [36]. The heat generated in the battery can be defined as shown in Eq. (2).

$$q_{gen} = \frac{1}{V}\left(I^2 R + IT\frac{\partial U_{ocv}}{\partial T}\right) \quad (2)$$

Here, represents the heat generation of battery, V is the battery volume, I is the discharge current, T is the battery temperature, R is the battery internal resistance and $\frac{\partial U_{ocv}}{\partial T}$ represents the entropy coefficient. As shown in Eq. (2), the battery temperature and operating current affect the heat generated by the battery. In this study, the current is constant throughout the experiment. The internal resistance of the battery changes depending on its temperature and state of charge. The relation given in Eq. (3) is used to find out the phase of the PCM in the battery box used in the cooling system [35].

$$\lambda_{PCM} = \begin{cases} 0 & T_{PCM} \le T_s \\ \dfrac{T_{PCM} - T_s}{T_l - T_s} & T_l \le T_{PCM} \le T_s \\ 1 & T_{PCM} \ge T_l \end{cases} \quad (3)$$

Where λ is the liquid fraction, T_s represents the freezing temperature, T_l represents the melting temperature. Melting and solidification temperature is the property of PCM. PCMs store sensible and latent heat. If the PCM temperature is lower than the melting temperature, the phase is solid and the heat it stores is shown in Eq. (4).

$$Q_{PCM} = m_{PCM} c_{p,s,PCM} (T_{PCM} - T_i) \quad (4)$$

Here is the PCM mass, is the specific heat capacity of PCM (solid phase), is the initial temperature. If the temperature of the PCM is at the melting temperature, PCM is in the mushy region. In this region, PCM is between solid and liquid phase and the liquid fraction is important. the can be expressed as Eq. (5):

$$Q_{PCM} = m_{PCM} c_{p,s,PCM} (T_{PCM} - T_i) + m_{PCM} H\lambda \qquad (5)$$

H is the latent heat and if the PCM temperature is above the melting temperature, the phase is liquid and the heat stored in the PCM is as in Eq (6).

$$Q_{PCM} = m_{PCM} c_{p,s,PCM} (T_{PCM} - T_i) + m_{PCM} H + m_{PCM} c_{p,l,PCM} (T_{PCM} - T_m) \quad (6)$$

Here, is the specific heat capacity of PCM (liquid phase), is the melting temperature.

RESULT AND DISCUSSION

In this article, the effect of organic PCMs on battery thermal performance is examined. Experiments are conducted to examine the temperature difference of batteries at ambient temperature in different current discharge over time. Batteries charged to full capacity are discharged to their full capacity at the constant current thanks to electronic load. Firstly, the battery module test of the electronic load device is performed at different discharge currents. The battery test times are 20 (3C), 30 (2C) and 60 (1C) minutes depending on the discharging rates. C rate is the current of discharge of a battery. These C rates are the current range recommended by the manufacturer of the battery used. The C-rates of the battery used in this experimental study at 1C, 2C and 3C are 2.2, 4.4 and 6.6 A, respectively. Although it was desired to go to high C rates, the technical specification of the battery did not support this data and could not meet the continuous 4C current. The maximum pulse discharge of the battery is 8800 mAh (4C) and is not suitable for use at constant current during discharge. The change of battery voltage and capacity with time at different discharge currents is given in Fig. 6.

Choosing the right type, battery capacity and C rate is very important for battery use and cycle. A battery with a low C rate is not meet the desired voltage and efficiency in the discharge state. As seen in Fig. 6, as the discharge current increases, the initial voltage suddenly decreases, which affects the battery capacity.

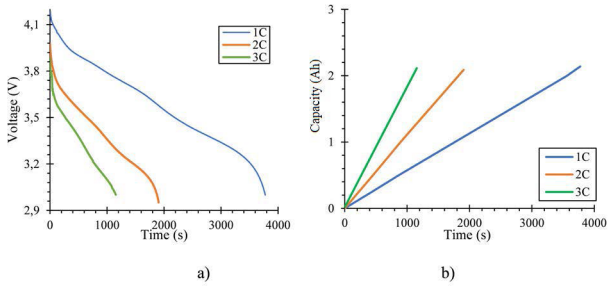

Figure 6. Comparison of a) voltage-time b) capacity-time at different discharge currents

The battery surface temperatures which are the anode, cathode and middle of battery were measured from three different points of the battery. These temperatures of the battery are close when these three-temperature data are examined. The battery surface temperatures are given in Fig. 7. Surface temperatures at different points or region of the battery may vary during discharge [37,38]. These temperature differences are generally caused by battery cooling. Each point or region of the battery surface may not be exposed to the same thermal boundary conditions. In this study, in the case of the battery box without PCM, the surface temperatures at each point of the battery differed.

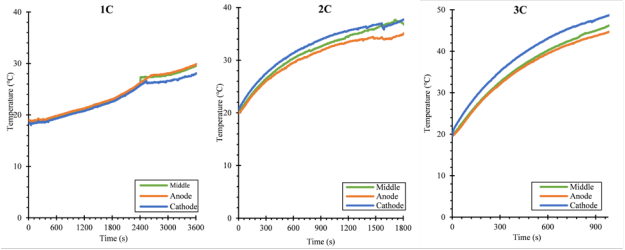

Figure 7. Battery surface temperature a) 1C, b) 2C, c) 3C

In Fig. 7a, it is seen that the difference between the battery surface temperatures does not change much at low discharge currents. As the discharge currents increase, the battery surface temperatures increase and the difference between the temperatures also increases as shown Fig. 7b and Fig. 7c. This is due to the cooling of the battery. Since the anode part is in contact with ambient air, its surface temperature has increased less. The middle part and cathode region of the battery are not in contact with ambient air. Because these areas are in contact with the air inside the battery box. So, these surface temperatures increase more than the anode part. The design of the cooling system around the battery is very important. If each area of the battery is cooled under different conditions, it can affect the battery life.

Fig. 8 shows the changes in battery surface temperatures over time in different discharge currents with 3 different organic-PCM and without-PCM conditions. The discharge process ended at the peak points of the temperature in the Fig. 8 and heat transfer occurs by natural convection at ambient temperature.

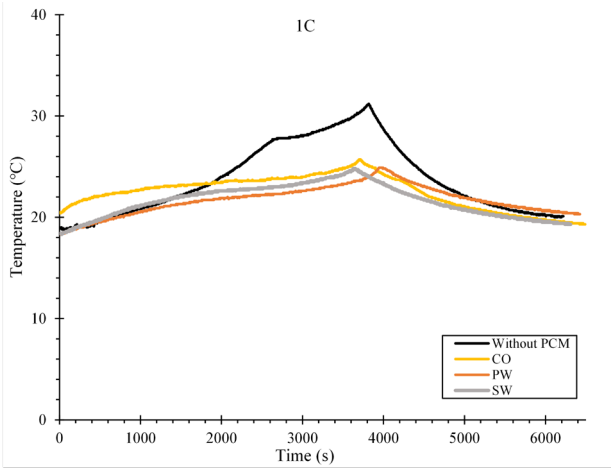

a)

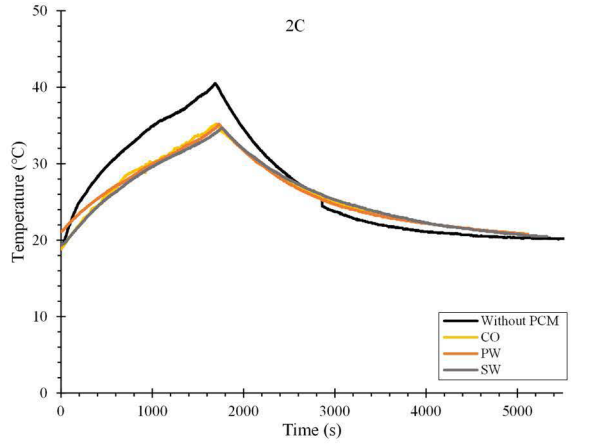

b)

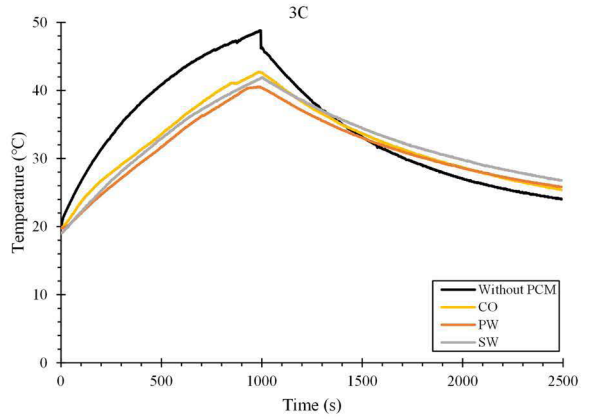

c)

Figure 8. Battery surface temperatures with organic PCM at different discharge currents a) 1C, b) 2C, c) 3C

The initial temperatures shown in Fig. 8 are equal to the ambient temperature. Ambient temperature varies between 19 and 20 °C depending on the experiment day conditions.

In the case without PCM, the maximum battery surface temperatures were measured as 30.7 °C, 40.3 °C and 48.8 °C, respectively, depending on the discharge rate which is 1C, 2C and 3C. When the discharge currents are 1C and 2C, it is seen that the batteries in the organic PCMs are at almost the same surface temperatures as shown Fig. 8a and Fig. 8b. Thanks to the organic PCMs, the battery surface temperature of the battery was approximately 5.2 °C and 6.3 °C lower at 1C and 2C rates, respectively, than that without PCMs. As the discharge current increases, battery surface temperatures in organic PCM were changed. In 3C rate, the lowest battery surface temperature is 40.5 °C in palm wax. This is followed by soy wax and coconut oil. The battery surface temperatures of these organic PCMs are 41.8 °C and 42.6 °C respectively. When the phase change of PCMs was examined, coconut oil was completely melted at 2C and 3C discharge rates. Palm wax was not melted but only in the 3C discharge current was the mushy region. However, no phase change was observed in soy wax at all discharge rates. As seen in Fig. 8c, the temperature of battery cools down more slowly due to the high temperatures of the organic PCMs after the discharge is completed. In addition, when the results obtained from the battery box with PCM are compared to the temperature curves from the test chambers without PCM, more homogeneous and non-suddenly rising/decreasing are obtained. This minimizes the sudden temperature changes of the battery and positively affects the life of the battery.

In Fig. 9, the middle battery surface temperature and the highest data of the organic PCMs temperature is given. As seen in Fig. 9a, there is a greater difference between the temperature of coconut oil and the surface temperature of battery, while in Figs. 9b and 9c, the temperature of soy and palm waxes is close to the battery surface temperature.

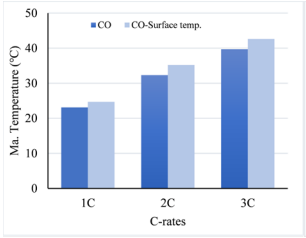

a)

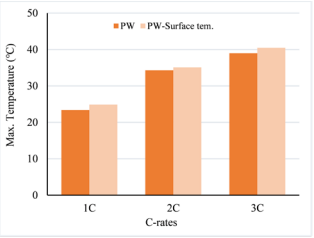

b)

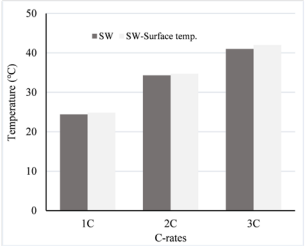

c)

Figure 9. Maximum battery surface temperature vs. PCM temperature (a) Coconut oil (b) Palm wax c) Soy wax

This shows that the thermal conductivity of these two PCMs may be higher than that of coconut oil. The thickness and mass of PCM directly affect these temperature differences.

In addition, the battery box is made of PLA and its thermal conductivity (k=0.13 W/mK) is very low [39]. This means that the heat absorbed by the PCM cannot be transferred to the environment. Therefore, the temperature of the PCM increases faster.

CONCLUSION

It is very important to be able to meet and maintain the capacity and long battery life of lithium-ion batteries. So, both storage and operating temperature are important and very effective for the battery. Long-term operation of batteries at high temperatures reduces their lifecycle and may cause thermal runaway. High temperature affects the internal structure of the battery. This can lead to great dangers for the battery. In this study, battery surface temperatures were investigated during 3 different discharges (1C, 2C, 3C) of batteries at ambient temperature which is between 19 °C and 20 °C. The experiments were conducted with 3 different organic PCMs and without PCM. In the case without PCM, it was observed that maximum battery surface temperatures vary between 30.7 °C and 48.8 °C depending on the discharge rate. In the case without PCM, sudden changes of temperature were observed in the battery surface temperatures. After placing the organic PCMs in the battery box, the battery surface temperatures vary between 25.5 °C and 42.6 °C for coconut oil, 24.8 °C and 41.8 °C for soy wax, and 25 °C and 40.5 °C for palm wax, depending on the discharge rate. Organic PCMs reduced the battery surface temperature. The lowest battery surface temperature is determined in Palm wax. This was followed by soy wax and then coconut oil. Due to the low PCM amount and the material of the battery box, the PCM temperature and the battery surface temperature are close. However, there are also temperature differences depending on the discharge rates. The box with low thermal conductivity affected the PCM and battery temperature. Palm and Soy waxes exhibited almost similar cooling performance, while coconut oil exhibited slightly lower cooling performance. Compared to without PCMs, sudden changes of temperature were not observed in organic PCM, which positively affects battery life. Although organic PCMs store heat and keep the battery temperature at the desired level, there may be difficulties in temperature control after the phase change due to their generally low thermal conductivity. These PCMs have the low melting point, so attention should be paid to ambient temperature and discharge rates in the application. Temperature measurements from a cell (battery) may not provide sufficient data on thermal behavior. Therefore, more experiments are needed to better understand the thermal performance of organic PCMs in battery groups instead of cell and to reveal the effect of these PCMs at higher charge/discharge currents. Heat storage, heat transfer and melting process properties of coconut, palm and soy wax, an organic PCMs, are discussed in detail in battery applications. In addition, in future studies, more experiments are needed to examine the thermal performance if materials with high thermal conductivity are included in the organic PCM.

References

1. K. Roshanai, Recent advances in lithium–ion battery utilization: A mini review, Sigma J. Eng. Nat. Sci. – Sigma Mühendislik ve Fen Bilim. Derg. (2023) 1272–1286. https://doi.org/10.14744/sigma.2021.00077.
2. T. Kim, W. Song, D.-Y. Son, L.K. Ono, Y. Qi, Lithium-ion batteries: outlook on present, future, and hybridized technologies, J. Mater. Chem. A 7 (2019) 2942–2964. https://doi.org/10.1039/C8TA10513H.
3. A. Khan, M. Ali, S. Yaqub, H.A. Khalid, R.R.U. Khan, K. Mushtaq, H. Nazir, Z. Said, Hybrid thermal management of Li-ion battery pack: An experimental study with eutectic PCM-embedded heat transfer fluid, J. Energy Storage 77 (2024) 109929. https://doi.org/10.1016/j.est.2023.109929.
4. A. Belgibayeva, A. Rakhmetova, M. Rakhatkyzy, M. Kairova, I. Mukushev, N. Issatayev, G. Kalimuldina, A. Nurpeissova, Y.-K. Sun, Z. Bakenov, Lithium-ion batteries for low-temperature applications: Limiting factors and solutions, J. Power Sources 557 (2023) 232550. https://doi.org/10.1016/j.jpowsour.2022.232550.
5. V.G. Choudhari, D.A.S. Dhoble, T.M. Sathe, A review on effect of heat generation and various thermal management systems for lithium ion battery used for electric vehicle, J. Energy Storage 32 (2020) 101729. https://doi.org/10.1016/j.est.2020.101729.
6. S. Ma, M. Jiang, P. Tao, C. Song, J. Wu, J. Wang, T. Deng, W. Shang, Temperature effect and thermal impact in lithium-ion batteries: A review, Prog. Nat. Sci. Mater. Int. 28 (2018) 653–666. https://doi.org/10.1016/j.pnsc.2018.11.002.
7. M.W. Nazar, N. Iqbal, M. Ali, H. Nazir, M.Z. Bin Amjad, Thermal management of Li-ion battery by using active and passive cooling method, J. Energy Storage 61 (2023) 106800. https://doi.org/10.1016/j.est.2023.106800.
8. M.S. Mert, M. Sert, H.H. Mert, Isıl Enerji Depolama Sistemleri İçin Organik Faz Değiştiren Maddelerin Mevcut Durumu Üzerine Bir İnceleme, Mühendislik Bilim. ve Tasarım Derg. 6 (2018) 161–174. https://doi.org/10.21923/jesd.331998.
9. C.A. Saleel, A review on the use of coconut oil as an organic phase change material with its melting process, heat transfer, and energy storage characteristics, J. Therm. Anal. Calorim. 147 (2022) 4451–4472. https://doi.org/10.1007/s10973-021-10839-7.
10. P.K.S. Rathore, K.K. Gupta, B. Patel, R.K. Sharma, N.K. Gupta, Beeswax as a potential replacement of paraffin wax as shape stabilized solar thermal energy storage material: An experimental study, J. Energy Storage 68 (2023) 107714. https://doi.org/10.1016/j.est.2023.107714.
11. T. Trisnadewi, E. Kusrini, D.M. Nurjaya, N. Putra, T.M.I. Mahlia, Experimental analysis of natural wax as phase change material by thermal cycling test using thermoelectric system, J. Energy Storage 40 (2021) 102703. https://doi.org/10.1016/j.est.2021.102703.
12. R.M. Kalombe, S. Sobhansarbandi, J. Kevern, Assessment of low-cost organic phase change materials for improving infrastructure thermal performance, Constr. Build. Mater. 369 (2023) 130285. https://doi.org/10.1016/j.conbuildmat.2022.130285.
13. A. Ariwibowo, M. Irsyad, A. Amrul, An Experimental Study of the Use of Coconut Oil-based PCM to Reduce the Thermal Load of Air Conditioners as an Effort to Save Energy, Motiv. J. Mech. Electr. Ind. Eng. 4 (2022) 35–44. https://doi.org/10.46574/motivection.v4i1.107.
14. Y.S. Indartono, A. Suwono, A.D. Pasek, D. Mujahidin, I. Rizal, Thermal Characteristics Evaluation of Vegetables Oil to be Used as Phase Change Material in Air Conditioning System, J. Tek.

Mesin 12 (2011). https://doi.org/10.9744/jtm.12.2.119-124.
15. L. Safira, N. Putra, T. Trisnadewi, E. Kusrini, T.M.I. Mahlia, Thermal properties of sonicated graphene in coconut oil as a phase change material for energy storage in building applications1, Int. J. Low-Carbon Technol. 15 (2020) 629–636. https://doi.org/10.1093/ijlct/ctaa018.
16. J. Jeon, J.H. Park, S. Wi, S. Yang, Y.S. Ok, S. Kim, Latent heat storage biocomposites of phase change material-biochar as feasible eco-friendly building materials, Environ. Res. 172 (2019) 637–648. https://doi.org/10.1016/j.envres.2019.01.058.
17. A. Benhorma, A. Bensenouci, M. Teggar, K.A.R. Ismail, M. Arıcı, E. Mezaache, A. Laouer, F.A.M. Lino, Prospects and challenges of bio-based phase change materials: An up to date review, J. Energy Storage 90 (2024) 111713. https://doi.org/10.1016/j.est.2024.111713.
18. A.R. Abdulmunem, H.M. Hamed, P.M. Samin, I.I. Mazali, K. Sopian, Thermal management of lithium-ion batteries using palm fatty acid distillate as a sustainable bio-phase change material, J. Energy Storage 73 (2023) 109187. https://doi.org/10.1016/j.est.2023.109187.
19. A. Verma, S. Shashidhara, D. Rakshit, A comparative study on battery thermal management using phase change material (PCM), Therm. Sci. Eng. Prog. 11 (2019) 74–83. https://doi.org/10.1016/j.tsep.2019.03.003.
20. S. John, K. Sreyas, Y. Mohan, A.D. Thampi, S. Rani, Numerical investigation on the effect of PCM thickness and nano-additive on the cooling performance of Stearic Acid based battery thermal management system, Mater. Today Proc. 80 (2023) 1442–1447. https://doi.org/10.1016/j.matpr.2023.01.267.
21. Z. Ling, S. Li, C. Cai, S. Lin, X. Fang, Z. Zhang, Battery thermal management based on multiscale encapsulated inorganic phase change material of high stability, Appl. Therm. Eng. 193 (2021) 117002. https://doi.org/10.1016/j.applthermaleng.2021.117002.
22. V.M. Goud, G. Satyanarayana, J. Ramesh, G.A. Pathanjali, D. Ruben Sudhakar, An experimental investigation and hybrid neural network modelling of thermal management of lithium-ion batteries using a non-paraffinic organic phase change material, Myristyl alcohol, J. Energy Storage 72 (2023) 108395. https://doi.org/10.1016/j.est.2023.108395.
23. M.Y. Yazıcı, Thermal Management of Small-Scale Li-ion Battery Module Using Graphite Matrix Composite with Phase Change: Effect of Discharge Rate, Iğdır Üniversitesi Fen Bilim. Enstitüsü Derg. 12 (2022) 389–402. https://doi.org/10.21597/jist.952021.
24. Y. Su, J. Shen, X. Chen, X. Xu, S. Shi, X. Wang, F. Zhou, X. Huang, Bio-based eutectic composite phase change materials with enhanced thermal conductivity and excellent shape stabilization for battery thermal management, J. Energy Storage 100 (2024) 113712. https://doi.org/10.1016/j.est.2024.113712.
25. J. Mei, G. Shi, H. Liu, Z. Wang, Organic and Inorganic Hybrid Composite Phase Change Material for Inhibiting the Thermal Runaway of Lithium-Ion Batteries, Batteries 9 (2023) 513. https://doi.org/10.3390/batteries9100513.
26. F.L. Rashid, M.A. Al-Obaidi, N.S. Dhaidan, A.K. Hussein, B. Ali, M.B. Ben Hamida, O. Younis, Bio-based phase change materials for thermal energy storage and release: A review, J. Energy Storage 73 (2023) 109219. https://doi.org/10.1016/j.est.2023.109219.
27. C. Tambe, D. Graiver, R. Narayan, Moisture resistance coating of packaging paper from biobased silylated soybean oil, Prog. Org. Coatings 101 (2016) 270–278. https://doi.org/10.1016/j.porgcoat.2016.08.016.
28. M.S.M. Al-Jethelah, A. Al-Sammarraie, S.H. Tasnim, S. Mahmud, A. Dutta, Effect of convection heat transfer on thermal energy storage unit, Open Phys. 16 (2018) 861–867. https://doi.org/10.1515/phys-2018-0108.
29. S. Kulandaivel, W.K. Ngui, M. Samykano, R.K. Rajamony, S.K. Suraparaju, N.S. Abd Ghafar, M. Mat Noor, Enhanced Heat Transfer Efficiency through Formulation and Rheo-Thermal Analysis of Palm Oil-Based CNP/SiO 2 Binary Nanofluid, Energy Technol. (2024). https://doi.org/10.1002/ente.202400314.
30. D.K. Yadav, P.K.S. Rathore, R.K. Singh, A.K. Gupta, B.S. Sikarwar, Experimental Study on Paraffin Wax and Soya Wax Supported by High-Density Polyethylene and Loaded with Nano-Additives for Thermal Energy Storage, Energies 17 (2024) 2461. https://doi.org/10.3390/en17112461.
31. S. Nurul Syahida, M.R. Ismail-Fitry, Z.M.A. Ainun, Z.A. Nur Hanani, Effects of palm wax on the physical, mechanical and water barrier properties of fish gelatin films for food packaging application, Food Packag. Shelf Life 23 (2020) 100437. https://doi.org/10.1016/j.fpsl.2019.100437.
32. A.N. Surendran, K.P.K. Ajjarapu, A.A. Arumugham, K. Kate, J. Satyavolu, Characterization of industry grade soybean wax for potential applications in natural fiber reinforced composite (NFRC) filaments, Ind. Crops Prod. 186 (2022) 115163. https://doi.org/10.1016/j.indcrop.2022.115163.
33. A. Farrahnoor, N.A.A. Sazali, H. Yusoff, B.T. Zhou, Effect of beeswax and coconut oil as natural coating agents on morphological, degradation behaviour, and water barrier properties of mycelium-based composite in modified controlled environment, Prog. Org. Coatings 196 (2024) 108763. https://doi.org/10.1016/j.porgcoat.2024.108763.
34. J. Liu, Y. Fan, Q. Xie, An experimental study on the thermal performance of mixed phase change materials-based battery cooling system, J. Energy Storage 46 (2022) 103839. https://doi.org/10.1016/j.est.2021.103839.
35. C. Qiu, C. Wu, X. Yuan, L. Wu, J. Yang, H. Shi, Multi-objective optimization of PCM-fin structure for staggered Li-ion battery packs, Bull. Polish Acad. Sci. Tech. Sci. (2023) 145677–145677. https://doi.org/10.24425/bpasts.2023.145677.
36. J. Liu, Y. Fan, Q. Xie, An experimental study on the thermal performance of mixed phase change materials-based battery cooling system, J. Energy Storage 46 (2022) 103839. https://doi.org/10.1016/j.est.2021.103839.
37. C. Wang, Y. Zhu, X. Fan, C. Qi, F. Gao, Mathematical model for thermal behavior of lithium-ion battery pack under overheating, Appl. Therm. Eng. 191 (2021) 116894. https://doi.org/10.1016/j.applthermaleng.2021.116894.
38. M. Sheikh, A. Elmarakbi, M. Elkady, Thermal runaway detection of cylindrical 18650 lithium-ion battery under quasi-static loading conditions, J. Power Sources 370 (2017) 61–70. https://doi.org/10.1016/j.jpowsour.2017.10.013.
39. M.Y. Gökaslan, E. Yıldız, Experimental investigation of pressure drop and heat transfer in porous media based on 3D printed triple periodic minimum surfaces, Exp. Heat Transf. (2024) 1–16. https://doi.org/10.1080/08916152.2024.2312464.

HITTITE JOURNAL OF SCIENCE AND ENGINEERING

e-ISSN: 2148-4171
Volume: 12 • Number: 1
March 2025

High Temperature Oxidation of Y doped Equiatomic AlCrFeNi Medium Entropy Alloy

Kerem Özgür Gündüz
Gebze Technical University, Materials Science and Engineering Department, Kocaeli, Türkiye.

Corresponding Author
Kerem Özgür Gündüz
E-mail: gunduz@gtu.edu.tr Phone: +90 262 605 26 65 Fax: +90 262 605 26 70
RORID: https://ror.org/01sdnnq10

Article Information
Article Type: Research Article
Doi: https://doi.org/10.17350/HJSE19030000348
Received: 11.11.2024
Accepted: 27.01.2025
Published: 25.03.2025

Cite As
Gündüz ÖK. High Temperature Oxidation of Y doped Equiatomic AlCrFeNi Medium Entropy Alloy. Hittite J Sci Eng. 2025;12(1):25-34.

Peer Review: Evaluated by independent reviewers working in at least two different institutions appointed by the field editor.
Ethical Statement: Not available.
Plagiarism Checks: Yes - iThenticate
Conflict of Interest: Authors declare no conflict of interest.

CRediT AUTHOR STATEMENT
Kerem Özgür Gündüz: Conceptualization, Data curation, Formal Analysis, Investigation, Methodology, Resources, Supervision, Writing – review and editing.

High Temperature Oxidation of Y doped Equiatomic AlCrFeNi Medium Entropy Alloy

Kerem Özgür Gündüz

Gebze Technical University, Materials Science and Engineering Department, Kocaeli, Türkiye.

Abstract

High temperature oxidation (HTO) of Y-doped (0.08 at.%) equiatomic AlCrFeNi alloy produced by vacuum arc melting was studied at 1100 °C for 168h in dry air. As-cast alloys consisted of disordered Fe-Cr rich A2 and Ni-Al rich B2 phase with the additional Y-rich precipitates rich in Ni and Al resembling B2 phase. Alloys possessed a columnar-dendritic microstructure in which dendritic regions contained weave-like morphology (≈120 nm), while interdendritic regions contained relatively coarse structures. Y-rich coarse precipitates were mostly found to segregate into interdendritic regions. After HTO tests the only oxide phase found was α-Al_2O_3 and lower mass gains compared to undoped material were recorded (lean≈ 0.95 mg.cm^{-2}, Y-doped 0.83 mg.cm^{-2}). Two distinct regions were observed based on top-view investigations I) Y-rich regions coupled with smooth Al_2O_3, II) Y-poor regions containing whiskers and smooth Al_2O_3. In both cases, wrinkling of Al_2O_3 scales was not observed. No oxide spallation was observed except at the edges. Additional stress formation on the edges coupled with the high strength of the alloy is assumed to result in oxide spallation. Compact Al_2O_3 scales exhibiting planar metal-oxide interface without wrinkles were observed by cross-sectional analysis. Y/Al-rich precipitates were found within the oxide scale and within the alloy (internal oxidation). Exposing samples also resulted in coarsening of A2 and B2 phases yet the alloy experienced only a 10% reduction in Vickers microhardness values (398 ± 6.8 HV). More studies on optimization of reactive element doping as well as mechanical properties are needed for further improvement of HTO performance.

Keywords: Medium Entropy Alloy, High Temperature Oxidation, Reactive elements, AlCrFeNi, Spallation

INTRODUCTION

Owing to their superior high temperature oxidation (HTO) resistance, ferritic FeCrAl alloys containing 13-20 wt. %Cr and 5-6 wt.% Al are widely used as heating elements in furnaces, cladding materials in nuclear industry, substrates in automobile exhaust catalysts and many more (1–3). This superior HTO resistance of FeCrAl alloys is related with the slow-growing protective α-Al_2O_3 scale especially over 900 °C and can be utilized up to 1300 °C (4,5). However, lean Al_2O_3 forming alloys without de-sulfurization are susceptible to spallation especially when exposed in cyclic oxidation conditions (6). Therefore, these alloys are commonly doped with reactive elements such as Y, Zr, Hf, La, Ce and their oxides (Y_2O_3, ZrO_2) to improve oxide adhesion and slow down the Al_2O_3 growth rate (7,8). The latter not only improves the oxidation properties, but also improves the mechanical properties (e.g. creep resistance) (7,8). Despite their excellent HTO resistance, FeCrAl alloys with open body BCC structure do not possess the desired mechanical properties at elevated temperatures (>600 °C) which highly restrict their applicability (9). Oxide dispersion strengthened (ODS) FeCrAl alloys with better mechanical properties are commercially available (e.g. Kanthal APMT), but they are expensive due to manufacturing route (powder metallurgy) (9). Hence, affordable alloys with identical HTO resistance but with better mechanical properties are needed. One such alternative might be cost effective Co free AlCrFeNi medium entropy alloys (ΔS_{con}: R>x>1.5R). This group of alloys either in equiatomic or in non-equiatomic compositions were shown to form α-Al_2O_3 scales at elevated temperatures (T≥900 °C) with much better mechanical properties such as high yield strength (1041-1424 MPa), high microhardness (403-553 HV) and adequate compressive ductility (ε≈ 18.6-40%) (10–16). Better mechanical properties of these alloys are related with the two-phase structure, B2 phase (Ni-Al rich) reinforcing A2 phase (Fe-Cr rich) (11). However, based on previous studies, RE-free AlCrFeNi alloys especially at 1100 ºC formed wrinkled/buckled α-Al_2O_3 scales with equiaxed morphology and showed extensive oxide spallation which will without a doubt limit the lifetime of these alloys in HTO conditions (14,16). Hence, improvement of high temperature oxidation properties by reactive element modification is needed on AlCrFeNi alloys. Y is one such element and studied extensively to modify FeCrAl and AlCoCrFeNi alloys as a single dopant (6,7,17,18). Y and Y_2O_3 modification are also studied on Cr_2O_3 forming CrFeNi and CoCrFeNi medium entropy alloys not only for improving the oxidation properties but also for better thermal stability (19–22). Especially on FeCrAl alloys, when used as a single dopant, 0.08 at.% Y addition was found to be most effective for prolonging the life time at elevated temperatures (7). However, to the best of the authors knowledge, the effect of reactive element doping on Co-free AlCrFeNi alloys are not yet studied. Therefore, for the first time, high temperature oxidation of Y-doped (0.08 at. % Y) equiatomic AlCrFeNi alloy at 1100 ºC for 168h is studied under air.

MATERIAL AND METHODS

Production and Characterization of Alloys

Y doped medium entropy AlCrFeNi alloy with the nominal composition of $Y_{0.08}$-$Al_{24.98}$ $Cr_{24.98}Fe_{24.98}Ni_{24.98}$ was produced by vacuum arc melting method (Edmund Bühler GmbH, Arc Melter AM200). Hereinafter, the alloy will be designated as Y-AlCrFeNi. Metals at least %99.95 pure were used to produce the alloys. Prior to melting, the chamber was evacuated to 10^{-6} mbar and subsequently filled with Ar (%99.999 pure). Final gas pressure of the system was 600 mbar. Melting process was carried out in two steps. First, Fe-Y master alloy containing 1 at.% Y was prepared. In the second step, this master alloy was melted with pure elements together to fabricate the alloy according to the nominal composition given previously. To obtain homogenous castings, alloys were melted at least 5 times by flipping them upside down in each melting cycle. Final castings were in the shape of ingots with the dimensions of 50 mm x 10 mm x 10 mm. Total weight of ingots after vacuum melting were approximately 24g. To obtain samples with the dimensions of 10 mm x 10 mm x 1 mm, ingots were sectioned with a low-speed saw. After sectioning, samples were ground down to 2500 grit emery paper and subsequently polished with alumina suspension (≈1 µm particle size). After polishing, samples were etched with 3 parts of HCl, 1 part of HNO_3 and

2 parts of H_2O for further metallographic investigations. It should be mentioned that only polished samples were used in high temperature oxidation tests. Prior to oxidation tests, phase analysis was carried out by Bruker D8 Advance (Cu Kα radiation) diffractometer by scanning between 20°-90° with the step size of 0.02°. The scanning rate was selected as 2 °/min and the electrical parameters were 40 mA and 40 kV. Microstructural investigations were made by Nikon Eclipse LV150 light microscope and Philips XL30 FEG SEM equipped with EDS detector (Amatek EDAX). Microhardness tests (Vickers) were carried out with Instron Wolpert Testor 2100 device under 500g load for 5 seconds of loading, dwell and unloading time. ASTM standard E92 is used as the microhardness procedure which is valid between 200gf-150kgf.

High Temperature Oxidation Tests

High temperature oxidation tests were carried out in tube furnace at 1100 °C under laboratory air for 168h. This temperature and exposure duration is commonly practiced to understand the initial high temperature oxidation behavior of Al_2O_3 forming alloys (23,24). Relative humidity of the room was approximately 25%. Temperature profiling of the furnace was carried out by placing an external IN625 jacketed k-type thermocouple in the furnace. The hottest zone of the furnace was approximately 10 cm long and temperature within this zone deviated ± 4 °C. Heating and cooling rate of the samples were 5 °C/min. Samples were placed in Al_2O_3 crucibles (%99.8 purity) in a way to achieve minimum contact with the sample. To ensure reproducibility of the results, exposures were repeated twice and 3 samples were exposed in each oxidation test. Mass gains for each sample was determined by weighing samples before and after HTO tests using sartorius CPA225D scale. The resolution of the scale is 0.01 mg.

Characterization After High Temperature Oxidation Tests

After HTO tests, phase analysis was carried out by Bruker Advance D8 diffractometer with identical parameters used to characterize as-cast alloys. After XRD analysis, top view investigations were made by Philips XL 30 FEG SEM equipped with Amatek EDAX EDS detector. Before SEM investigations, samples were deposited with gold to prevent charging. For cross-sectional investigations one sample was cold mounted with epoxy resin (Struers Epofix) without sectioning. Cold mounted samples were ground down to 2500 grit emery paper and subsequently polished with colloidal Alumina (≈1 µm) and Silica (≈50 nm). Cross-sectional SEM-EDS examinations were also made with Philips XL30 FEG SEM. Samples were also deposited with gold before the cross-sectional investigations. Microhardness tests were also made with the same device with identical parameters.

RESULTS AND DISCUSSION

Investigation of as-cast Y-AlCrFeNi Alloy

Figure 1 illustrates the XRD analysis of as-cast Y-AlCrFeNi alloy. According to the analysis, two phases were detected. I) Fe-Cr rich disordered BCC A2 phase and II) and Ni-Al rich ordered BCC B2 phase. Y-rich phase if present any were not found in the diffractogram most probably related to the minor dopant concentration (0.08 at. %Y) in the alloy. Additionally, peaks of A2 and B2 phases were found to overlap in the diffractogram since these phases have very similar lattice parameters (11). Yet, the (111) peak observed at 55° only belongs to B2 phase, hence justifies the presence of B2 phase (25,26). Furthermore, a second XRD analysis was performed on the same alloy by grinding and re-analyzing the surface and the obtained diffractogram is presented in the supplementary information as Figure S1. B2 phase is usually characterized with the (100) reflection. After the second XRD analysis, both (100) peak with the additional (111) was observed in the diffractogram hence proving the presence of B2 phase. Similar XRD results on AlCrFeNi alloys were also given in previous studies (25–28). The intensity of (110) peak is much higher compared to the other peaks observed in the XRD diffractogram. In contrast, in the second diffractogram the intensity of (211) peak was much higher (Figure S1). The reason for that is related to the production route, since alloys produced by vacuum arc melting usually exhibit anisotropic microstructures due to directional and slow solidification process (16,25,28).

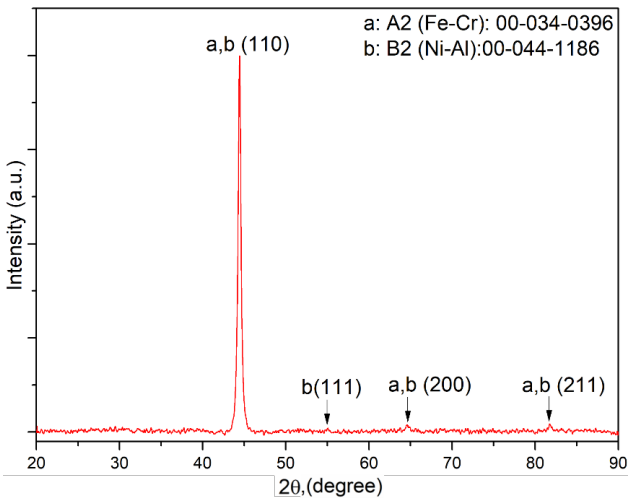

Figure 1: XRD pattern of as-cast Y-AlCrFeNi alloy.

Figure 2 represents the SEM images of polished as-cast Y-AlCrFeNi alloys captured with BSE detector with different magnifications. According to low-magnification images, columnar grains with different orientations were revealed by electron channeling contrast. However, etched optical microscopy images given in Figure S2 (supplementary information) revealed that, the microstructure is dendritic. Hence, orientation difference should be related to the formation of dendrites in a columnar manner with different orientations during the solidification process. General composition of Y-AlCrFeNi alloy determined by SEM-EDS analysis was given in Table 1. Alloys were slightly richer in Al but except that they are very close to the nominal composition. Y concentration was not determined by SEM-EDS analysis due to low Y concentration (0.08 at.% Y). Better analytical techniques such as arc/spark optical emission spectroscopy (OES) or glow discharge optical emission spectroscopy (GD-OES) is needed to determine the actual Y concentration. Furthermore, magnified images Figure 2b and

Figure 2c revealed that dendritic regions consisted of a two-phase lamellar structure commonly referred as weave-like morphology, dark phase being Ni-al rich B2 phase and bright phase being Fe-Cr rich A2 phase (29,30). The width of lamella in dendritic regions is approximately 120 nm. Interdendritic regions were also consisted of same phases, yet they are coarser and resemble a cellular morphology (≈ 1µm). On dendritic regions, it is impossible by SEM-EDS to determine the chemical composition of these phases individually due to small lamella size. However, SEM-EDS analysis carried out on interdendritic regions (Table 1), clarified that dark regions are Ni-Al rich while bright regions are rich in Fe-Cr. The region where the chemical analysis of individual A2 and B2 phases determined by SEM-EDS were given in the supplementary information section as Figure S3. Based on TEM analysis performed in previous studies, the dark regions correspond to Ni-Al rich B2 phase while bright regions correspond to Fe-Cr rich A2 phase (13,28). There is a slight difference in compositions between SEM-EDS and TEM-EDS due to fine microstructure coupled with relatively low spatial resolution of SEM-EDS despite performing the analysis the on coarse regions. Furthermore, In the same Figure (Figure S3), some bright precipitates were observed within the coarse B2 phase located at the interdendritic regions. Due to the very small size of these precipitates, it was not possible to identify these with SEM-EDS analysis, hence further work is needed with TEM-EDS or Atom Probe Tomography (APT). Yet, a study performed on AlCrFeNi system identified these precipitates as A2 precipitates within the B2 coarse matrix (30). Hence, it is likely that these are A2 precipitates. More will be discussed in the upcoming sections.

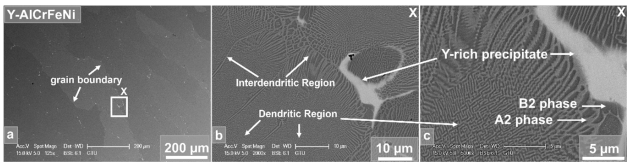

Figure 2. SEM analysis of as-cast Y-AlCrFeNi alloy. a) 125x magnification while b) 2000x and c) 5000x are magnified images of region X marked in a).

Additionally, Y-rich bright precipitates were found to be distributed in the microstructure, as coarse precipitates mostly segregated into interdendritic regions. Y-rich precipitates did not have a distinct morphology, yet the width of these precipitates is approximately 1-5 µm. Chemical analysis of these precipitates by SEM-EDS is also given in Table 1. Based on the obtained composition, these precipitates resemble Ni-Al rich B2 phase enriched with Y. Further analysis is needed to determine this by SEM-EBSD or TEM-SAED. Still, according to previous research on Y doped AlCoCrFeNi alloy, a new phase is identified as a Ni-Y rich phase differing from the Ni-Al phase, but the chemical composition of this phase is not given (31). It is possible that, same phase might be present in the current study. Nevertheless, more studies are needed for phase identification of Y-rich precipitates.

Table 1. SEM-EDS analysis results of as-cast Y-AlCrFeNi.

Points	Fe	Cr	Al	Ni	Y
General Composition	24.36	24.05	27.2	24.39	-
A2 Phase	39.71	43.55	9.77	6.97	-
B2 Phase	15.67	12.54	33.89	37.9	-
Y-Rich Precipitate	9.35	4.35	30.5	41.81	13.99

Furthermore, as-cast Y-AlCrFeNi alloy exhibited a microhardness value of 447 ± 17 HV. A2 and B2 phases exhibit very similar lattice parameters hence they form coherent interfaces which can be understood from the overlapping of peaks in the XRD diffractogram (28,32). The misfit strain in weave-like A2/B2 structures in AlCoCrFeNi alloys were reported as ε= 0.7% (33). This high misfit strain in return causes hardening but in the cost of ductility(29,30). Nevertheless, obtained values are consistent with the previous publications on equiatomic AlCrFeNi alloys (12,13,16). Furthermore, when compared, this value is twice as much of FeCrAl alloys which in return might increase the applicability for load bearing high temperature applications (34). However, as a future work, it is intended to produce alloys with lower misfit strains to achieve a balance between hardness and ductility.

Investigations After High Temperature Oxidation Tests

Figure 3 represents the XRD analysis of Y-AlCrFeNi alloy after HTO tests at 1100 °C after 168h. According to the diffractogram, the only phase detected after the HTO tests are α-Al_2O_3 showing the capability of Y-AlCrFeNi alloy to form protective α-Al_2O_3 scale. No additional phase containing Y-rich oxides were detected in the XRD analysis presumably due to low concentration of Y (0.08 at.% Y) in the alloy. According to the study of Ren et al. (31) when AlCoCrFeNi is doped with 0.1 at.% Y, the only detected phase was also α-Al_2O_3. Tang et al. (18) also reported similar results. Therefore, results consist well with the previous studies. Furthermore, additional peaks belonging to alloy phases (A2 and B2) were also observed. Peaks observed at 2θ= 25° and 44.2° were not able to be identified hence designated as X.

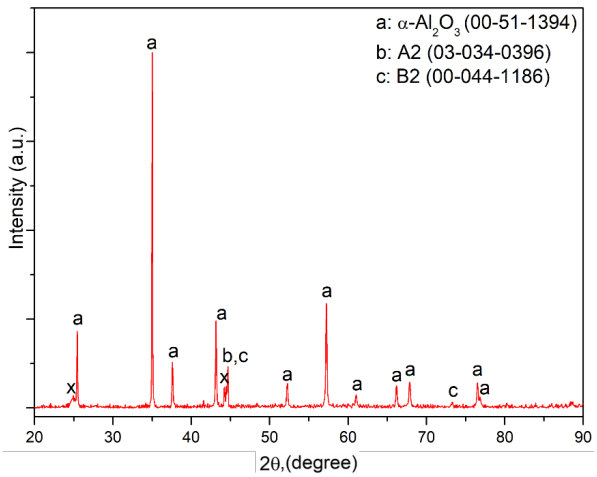

Figure 3. XRD analysis of oxidized Y-AlCrFeNi alloys at 1100 °C for 168h in dry air.

Figure 4. illustrates the top-view SEM images captured after oxidation tests at 1100 °C for 168h. Images Figure 4b and Figure 4c are the magnified regions shown in Figure 4a. Furthermore, Figure 5 represents the point SEM-EDS analysis carried out on regions X and Y marked in Figure 4. Point analysis results are given in Table 2. According to the combined results of Figure 4 and Figure 5, two distinct regions were identified. X represents regions containing whiskers and flat surfaces while region Y consists of bright oxides coupled with flat surfaces without formation of whiskers. On region X, SEM-EDS results suggest the presence of Al_2O_3 based on the analysis carried out on whiskers and flat surfaces. On the other hand, bright oxides found in region Y suggest the formation of a Y and Al rich oxide, coupled with the formation of Al_2O_3. The chemical composition and related phases will be discussed in cross-sectional SEM-EDS examinations.

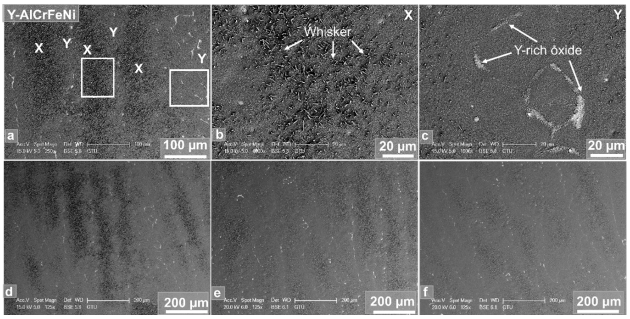

Figure 4. Top-View SEM images of Y-AlCrFeNi alloys after oxidation at 1100 °C for 168h. a) Low magnification top view image. b) Region marked as X in low magnification image. c) Region marked as Y in low magnification image. Images d), e), f) represent alternative images showing that regions X and Y is repeating all over the surface.

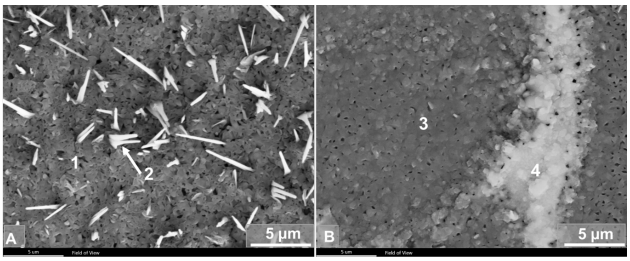

Figure 5. Top-view point SEM-EDS analysis of oxidized Y-AlCrFeNi carried out on a) whisker rich regions and b) Y-rich oxide regions.

Table 2. Top-view point SEM-EDS analysis results of regions marked in Figure 5.

Points	Fe	Cr	Al	Ni	Y	O
1	0.34	0.41	47.61	0.08	0.11	51.45
2	0.18	0.21	36.99	0.05	0.06	62.51
3	0.31	0.66	46.66	0.11	0.13	52.14
4	2.8	1.32	33.23	5.44	9.45	47.76

Furthermore, Figures 4d-4f clearly show that the oxidation pattern observed in Figure 4a is repeated everywhere on the surface: Whiskers being formed on regions that do not contain Y-rich oxides, while the presence of Y-rich oxides suppressed whisker formation. The presence of whiskers on the surfaces is due to formation of metastable Al_2O_3 phases such as θ-Al_2O_3 or γ-Al_2O_3 which are not protective and grow outwards by cation diffusion(35–37) . With time, they do transform into α-Al_2O_3 (38). The important conclusion is the presence of Y-rich oxides clearly shown to suppress whisker formation at 1100 °C when compared with the lean equiatomic AlCrFeNi alloy (16). This is also verified on after oxidation top-view analysis of Y doped FeCrAl alloys (37,39). In fact, on FeCrAl alloys, due to homogeneous distribution of Y-rich precipitates in the matrix, whisker formation is eliminated (37,39). However, arc melted Y-AlCrFeNi alloy did not show this effect, since Y-rich coarse precipitates were mostly segregated into interdendritic regions and in return, Y-rich oxides were more regularly formed in these regions after high temperature oxidation. Therefore, the effect of suppressing whisker formation is rather localized in vacuum arc melted Y-AlCrFeNi alloy. By investigating the previous studies on Y doped AlCrCoFeNi alloys, no such oxidation behavior (regions with and without whiskers) was reported (18,31,40). One such possibility might be the heating regime. Rather than placing the samples in the cool furnace and ramping with a typical heating rate of 5-7 ºC/min, directly inserting the samples into hot zone of the pre-heated furnace at 1100 °C might have mitigated the formation of whiskers since over 1000 °C formation of metastable Al_2O_3 phases are greatly suppressed (35).

Nevertheless, compared to lean equiatomic AlCrFeNi alloy, spallation free, smooth Al_2O_3 scales without any wrinkling were obtained on Y-AlCrFeNi alloy even on the whisker containing regions, showing the beneficial effect of Y doping (16). However, additional top-view SEM images captured on the edges of oxidized samples given in Figure 6 show that Al_2O_3 scales on the edges were completely spalled off, revealing the bare alloy surface. Since the metal surfaces revealed by oxide spallation do not contain any newly formed oxide, it is suggested that Al_2O_3 scales spalled off during the cooling step. The reason for such behavior is related to the additional stress formation on the edges due to geometrical effect coupled with the high strength of Y-AlCrFeNi alloy. All high temperature alloys, when oxidized at elevated temperatures, experience additional stress formation on the edges due to their high curvature (sharp edges) (41,42). Yet, alloys with weak mechanical properties such as FeCrAl alloys, especially at elevated temperatures, can relieve these additional stresses by the combined plastic deformation of alloy and oxide (8). However, the high strength of Y-AlCrFeNi alloy similar to ODS FeCrAl alloys hinders the plastic deformation of alloy thus stress is relieved by the fracture and spallation of Al_2O_3 scales (8,43). Spallation of oxides around edges were also reported in HTO of lean equiatomic AlCrFeNi alloy at 1100 ºC (16). To the best of the authors knowledge, edges of Y-doped AlCrCoFeNi alloys (similar mechanical properties to AlCrFeNi alloy) after high temperature oxidation were not investigated (18,31,40). As a future study, it might be interesting to examine how edges of Y doped AlCoCrFeNi alloys behave after high temperature oxidation. Figure 7 depicts the cross-sectional SEM images captured after high temperature oxidation tests at 1100 °C for 168h. Figure 8 illustrates the SEM-EDS elemental mapping results while Figure 9 shows the point SEM-EDS analysis results. Point SEM-EDS results were tabulated in

Table 3.

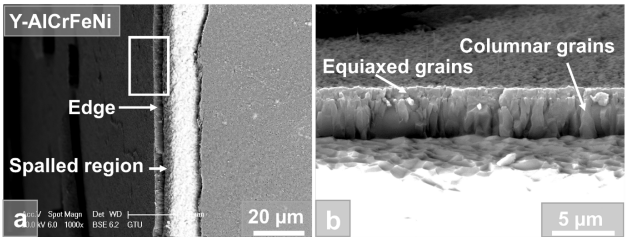

Figure 6. Top-view SEM analysis of oxidized Y-AlCrFeNi alloy captured near the edges of the sample, a) low magnification image, b) Marked region in image a in higher magnification.

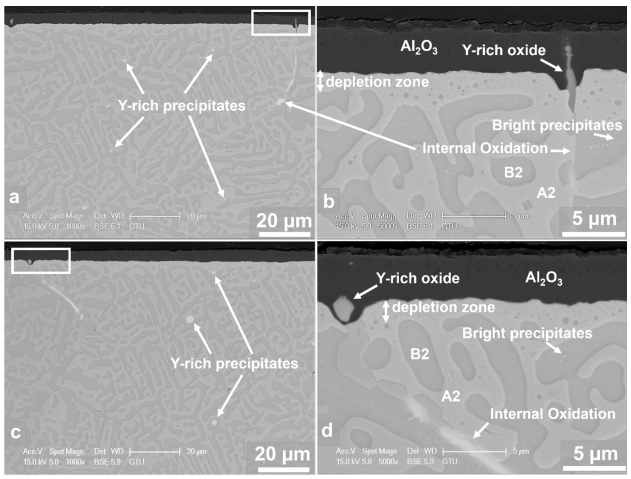

Figure 7. Cross-sectional SEM images of oxidized Y-AlCrFeNi alloy captured from two different regions, a,c) low magnification images , b,d) High magnification images of regions marked in a), c) respectively.

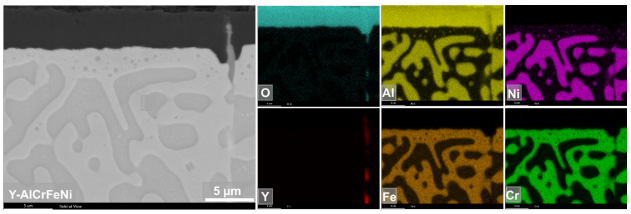

Figure 8. Cross-sectional SEM-EDS Mapping analysis of oxidized Y-AlCrFeNi alloy.

Table 3. Cross sectional point SEM-EDS analysis results of regions marked in Figure 9.

Points	Fe	Cr	Al	Ni	Y	O
1	-	-	43.24	-	-	56.76
2	-	-	33.29		8.8	57.91
3	-	-	43.47	-	-	56.53
4	-	-	25.47	-	15.35	59.18
5	43.71	48.43	4.82	3.04	-	-
6	8.92	4.07	43.55	43.46	-	-
7	9.8	3.15	26.77	46.34	13.94	-
8	9.43	3.68	26.54	46.45	13.9	-

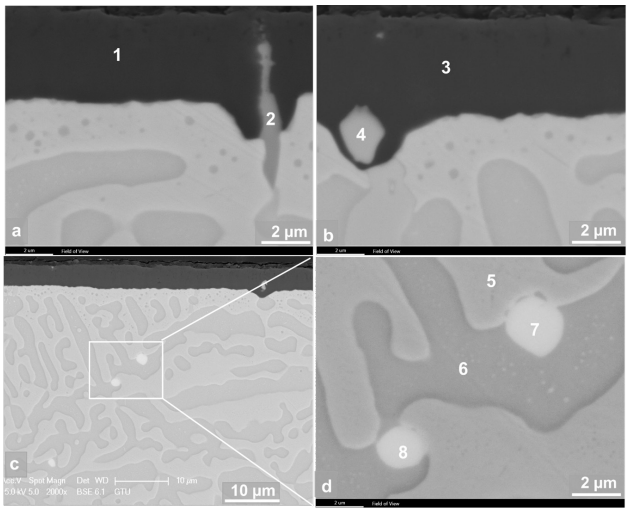

Figure 9. Cross-sectional point SEM-EDS analysis of oxidized Y-AlCrFeNi alloy. a,b) Different regions containing Y-rich oxides, c) Region that contains Y-rich precipitates in the alloy. d) Marked region of Figure c in higher magnification.

Based on the cross-sectional analysis combined with XRD results, pore free α-Al_2O_3 scales with planar metal-oxide interfaces without wrinkles/buckles were obtained. α-Al_2O_3 scales also adhered well to the substrate. When compared with the lean equiatomic AlCrFeNi alloy, this is a significant improvement showing the beneficial effect of Y addition (16).

In localized regions though, Y-Al rich oxides were also present as coarse precipitates within the oxide due to relatively high Y concentration (Figure 8 and Figure 9). In some cases, they were completely encapsulated within the oxide scale. When they are located around the metal-oxide interface they form localized inwards grown perturbations/intrusions known as oxide pegs (44,45). In earlier studies, oxide pegs were reported to improve oxide adhesion by mechanical keying the oxide scale to the substrate. However, present studies show that it is not necessary to have oxide pegs to improve the adhesion of oxide scales (44,46).

Alternatively, when Y-Al rich precipitates are not enveloped continuously by Al_2O_3 scale, the oxidation is progressing towards the metal, forming internal oxides especially in metal grain boundaries (intergranular oxidation). In other words, these precipitates act as oxygen channels towards the metal (17). These internal oxides are reaching almost 50 µm deep within the metal. Based on previous studies, these Y-Al precipitates within oxide scale are identified as Yttrium Aluminates. In high temperature oxidation studies, most commonly observed Yttrium Aluminate phase is $Y_3Al_5O_{12}$ (YAG phase) along with the $YAlO_3$ (YAP phase) (17,47,48). Point analysis performed on the Y-Al rich precipitate observed in Figure 9b showed excellent fit to $Y_3Al_5O_{12}$ phase (Point 4 in Table 3). Yet, the precipitate observed in Figure 9a showed a darker contrast and measured to be richer in Al (Point 2, Table 3). None of the phases reported in the Y_2O_3-Al_2O_3 phase diagram fit into this stoichiometry (49). Additionally, it should be stated that, this precipitate has

an elongated rod-like shape hence it is possible that signals might have been collected from the surroundings during the SEM-EDS analysis. Nevertheless, the darker contrast of this precipitate points toward a relatively Y-poor phase. Further studies with better analytical techniques such as TEM or APT are required to fully identify this phase. Additionally, the deepest part of the mentioned precipitate within the metal (intergranular oxide in the metal) is identified as Y_2O_3 (Figure S4 in the supplementary information) by SEM-EDS analysis which is expected since Y_2O_3 is thermodynamically more stable than Al_2O_3 (17). A very thin depletion zone (≈ 1-2 µm) was observed beneath the Al_2O_3 scale, showing that the alloy can supply sufficient Al to the surface (Figure 9). When compared with the initial microstructure, coarse A2 (bright) and B2 (dark) phases with intertwined morphology were observed in cross-sectional investigations (Figure 9). Point analysis carried out on A2 and B2 precipitates verified that A2 phase is rich in Fe and Cr while B2 phase is rich Ni and Al as expected (Figure 9d and Table 3). The chemical composition of these phases correlates well with the previous studies (13,16,28). Additionally, Y-rich precipitates were also present within the alloy microstructure. Chemical composition of Y-rich precipitates before and after the oxidation tests are quite similar showing that they are rich in Ni, Al and Y. As mentioned previously, these precipitates resemble B2 phase composition that is rich in Y. Yet, further studies with TEM are required to identify the crystal structure of these precipitates. Furthermore, bright precipitates were found within the B2 phase as in the case of coarse structures found in the as-cast alloy (Figure S3). Analysis of such precipitates are given in the supplementary information Figure S5. According to Figure S5, the analysis performed on these regions resulted in a higher Fe/Cr concentration compared to the surrounding regions. Obviously, signals will be collected from the surroundings, yet similar precipitates were identified as A2 phase in a previous study (30). According to previous studies, it is stated that formation of weave-like structure is a result of spinodal decomposition (29,33). Hence a similar mechanism might trigger the formation of nano-precipitates within the B2 phase due to relatively high Fe/Cr concentration of B2 phase. After high temperature oxidation test (1100 °C, 168h), average mass gain values of 0.83 ± 0.01 $mg.cm^{-2}$ were obtained. When compared to the lean Al_2O_3 forming AlCrFeNi alloy (mass gain ≈ 0.95 $mg.cm^{-2}$), and lean FeCrAl alloys at 1100 °C after 1 week (mass gain ≈ 1 $mg.cm^2$), recorded value in the present study is lower (16). It should be noted that the mass gain value for lean equiatomic AlCrFeNi alloy is obtained by converting the thickness value (5.1 ± 0.5 µm) into mass gain to obtain a more accurate value. The reason for obtaining lower mass gain is related to the reduced oxide growth rate and partial elimination of whisker formation when compared with the lean AlCrFeNi alloy (16). However, when compared with the FeCrAl alloys containing 0.1 wt.% Y these values are slightly higher (≈0.76 $g.cm^{-2}$) (37,39). A comparison of surfaces formed on Y-FeCrAl and Y-AlCrFeNi suggests that Y-rich oxides as spherical precipitates were distributed more homogenously on Y-FeCrAl alloy and as a result, formation of whiskers were eliminated with 0.1 wt.% Y doping (37). High entropy AlCoCrFeNi alloys doped with 0.1 at.% Y showed mass gain values around 0.77 $mg.cm^{-2}$ in which whisker formation was not reported (31,40). In the present study, the oxide thickness based on cross-sectional investigations were determined as 3.9 ± 0.14 µm. Conversion of this thickness value into mass gain according to the formula given in reference (50) results in 0.75 $mg.cm^2$. Two sources are identified that results in additional mass gain: I) Formation of Whiskers II) Formation of Y-rich oxide precipitates both in the oxide scale and in the metal (internal oxidation). Since Y-rich oxide formation is also observed on Y-AlCoCrFeNi and Y-FeCrAl alloys, the reason for further additional mass gain is more likely related to the formation of whiskers on top of the oxide scales. Additionally, microhardness measurements carried out after the oxidation tests showed that, values were determined as 398 ± 6.8 HV. Comparing this value with the as-cast structure revealed that the reduction by precipitate coarsening is approximately 10%. Therefore, these alloys were shown to retain their hardness values after 168h at 1100 °C. Prolonged exposures might be useful to observe the coarsening behavior and its effect on microhardness values. Despite Y-AlCrFeNi alloys show enhanced mechanical properties compared to FeCrAl alloys, it seems that high strength of the former caused oxide spallation around edges. This finding shows that the strength of the alloy should be tuned (reduced) by purposeful coarsening with heat-treatments or adjusting the composition in a manner to not prevent plastic deformation at elevated temperatures at least to a level might be a future goal. Additionally, further studies might be useful to improve the high temperature oxidation performance of Co free AlCrFeNi alloys (e.g. mitigating whisker formation or internal oxidation) by optimizing the reactive element concentration, for instance by single doping with Hf and/or double doping with Y and Hf as given in the previous studies (50,51).

CONCLUSION

In this study, production (vacuum arc melting) and high temperature oxidation of Y doped (0.08 at.%Y) cost effective medium entropy AlCrFeNi alloy at 1100 °C for 168h were studied. Conclusions drawn from the present study are given below:

1-Y doped AlCrFeNi alloy in as-cast state consisted of A2 (disordered Fe-Cr rich) and B2 (ordered Ni-Al rich) phases according to XRD and SEM investigations. Due to production by vacuum arc melting, Y-AlCrFeNi alloy was highly oriented in <110> directions.

2-According to etched optical microscopy images coupled with SEM investigations; alloys were found to exhibit a columnar dendritic structure. Dendritic regions consisted of weave-like structures with nano sized A2 and B2 phases while coarser structures with identical phases were found in interdendritic regions. Y-rich coarse precipitates were also observed to form mainly in interdendritic regions. The composition of this phase resembles B2 phase enriched in Y, but further identification with TEM is needed.

3-Microhardness of as-cast Y-AlCrFeNi is measured as 447 ± 11 HV. High hardness of this alloy is due to coherent B2 phase reinforcement of A2 phase.

4-After high temperature oxidation tests carried out at 1100 °C for 168h in dry air, the only detected oxide phase was

α-Al_2O_3 with the additionally observed substrate phases.

5-Top-view analysis revealed that two different types of oxides were observed: I) Region enriched with Y-rich oxides coupled with smooth Al_2O_3 surfaces. II) Y-poor regions consisting of whiskers and smooth Al_2O_3 surfaces. This shows that Y addition into equiatomic AlCrFeNi alloy suppresses whisker formation but not entirely on the surface, due their segregation into interdendritic regions.

6-Despite formation of whiskers on the surface, Y-addition prevented wrinkling and spallation on the main surfaces. However, oxide scales spalled around the edges due to additional stress formation by geometrical effects coupled with the high strength of Y-AlCrFeNi alloy, which prevented stress relaxation by combined plastic deformation of metal and oxide.

7-Cross-sectional investigations revealed that Al_2O_3 scales were compact and pore-free. Planar metal-oxide interfaces without any wrinkles/buckles were observed, verifying the beneficial effect of Y addition.

8-Y-rich precipitates within the oxide scale and within the metal as internally oxidized precipitates were observed in cross-sectional examinations. Some of these precipitates show excellent fit to $Y_3Al_5O_{12}$ (YAG) phase determined by SEM-EDS point analysis. Yet, precipitates deficient in Y were also observed.

9- After exposing samples at 1100 °C for 168h, coarsening of A2 and B2 phases occurred. However, a microhardness value of 398 ± 6.8 HV was measured after the high temperature oxidation tests. Therefore, despite coarsening, only a 10% reduction compared to as-cast structure was obtained.

10-Despite high hardness and its retention after exposures at 1100 ºC for 168h, spallation of oxides located around the edges suggests that an optimization of mechanical properties (heat-treatment, alloying) might be useful for further prolonging the lifetime. Furthermore, optimization of reactive element addition such as double doping with Y and Hf might further improve HTO performance (preventing internal oxidation and whisker formation).

Acknowledgement

Author would like to thank technicians Adem Şen and Ahmet Nazım for their technical assistance in XRD and SEM studies respectively. Casting, sample preparation as well as high temperature oxidation tests were carried out in Gebze Technical University metal casting and heat treatment laboratories, thus the author thanks for the equipment usage to founding members Prof. Dr. Yücel Gençer and Prof. Dr. Mehmet Tarakçı. This work was funded by Gebze Technical University, Project Number: (2023-A-105-01).

References

1. Bunn JK, Fang RL, Albing MR, Mehta A, Kramer MJ, Besser MF, et al. A high-throughput investigation of Fe-Cr-Al as a novel high-temperature coating for nuclear cladding materials. Nanotechnology. 2015;26(27).
2. Naumenko D, Quadakkers WJ, Galerie A, Wouters Y, Jourdain S. Parameters affecting transient oxide formation on FeCrAl based foil and fibre materials. Materials at High Temperatures. 2003 Jan 1;20(3):287–93.
3. Eklund J, Persdotter A, Ssenteza V, Jonsson T. The long-term corrosion behavior of FeCrAl(Si) alloys after breakaway oxidation at 600 °C. Corros Sci. 2023;217:111155.
4. Dryepondt S, Pint BA, Lara-Curzio E. Creep behavior of commercial FeCrAl foils: Beneficial and detrimental effects of oxidation. Materials Science and Engineering: A. 2012;550:10–8.
5. Kim C, Tang C, Grosse M, Maeng Y, Jang C, Steinbrueck M. Oxidation mechanism and kinetics of nuclear-grade FeCrAl alloys in the temperature range of 500–1500 °C in steam. Journal of Nuclear Materials. 2022;564:153696
6. Meier GH, Pettit FS, Smialek JL. The effects of reactive element additions and sulfur removal on the adherence of alumina to Ni- and Fe-base alloys. Materials and Corrosion. 1995 Apr 1;46(4):232–40.
7. Pint BA. Optimization of reactive-element additions to improve oxidation performance of alumina-forming alloys. In: Journal of the American Ceramic Society. 2003.
8. Naumenko D, Pint BA, Quadakkers WJ. Current Thoughts on Reactive Element Effects in Alumina-Forming Systems: In Memory of John Stringer. Vol. 86, Oxidation of Metals. 2016.
9. Brady MP, Yamamoto Y, Santella ML, Maziasz PJ, Pint BA, Liu CT, et al. The development of alumina-forming austenitic stainless steels for high-temperature structural use. JOM. 2008;60(7).
10. Dong Y, Lu Y, Kong J, Zhang J, Li T. Microstructure and mechanical properties of multi-component AlCrFeNiMo x high-entropy alloys. J Alloys Compd. 2013;573.
11. Ren M, Wang G, Li B. Microstructure and properties of AlCrFeNi intermetallic for electronic packaging shell. In: 18th International Conference on Electronic Packaging Technology, ICEPT 2017. 2017.
12. Jiang Z, Chen W, Xia Z, Xiong W, Fu Z. Influence of synthesis method on microstructure and mechanical behavior of Co-free AlCrFeNi medium-entropy alloy. Intermetallics. 2019;108.
13. Jumaev E, Abbas MA, Mun SC, Song G, Hong SJ, Kim KB. Nano-scale structural evolution of quaternary AlCrFeNi based high entropy alloys by the addition of specific minor elements and its effect on mechanical characteristics. J Alloys Compd. 2021;868.
14. Yang D, Liu Y, Han T, Zhou F, Qu N, Liao M, et al. High thermal stability and oxidation behavior of FeCrNiAl-based medium-entropy alloys prepared by powder metallurgy. J Alloys Compd. 2022;918:165562.
15. Hwang YJ, Kim KS, Na YS, Lim KR, Lee KA. High-temperature oxidation properties of economical and lightweight Fe-Cr-Ni-Al medium-entropy alloy. Corros Sci. 2023;219:111231.
16. Ozgenc T, Gunduz KO. Effect of Fe Concentration on the High Temperature Oxidation Behavior of Fex(CrAlNi)100−x Medium Entropy Alloys. High Temperature Corrosion of Materials. 2024;101(2):251–78.
17. Kim S, Lee CH, Kim T, Jang JH, Moon J, Falaakh DF, et al. Effects of yttrium on the oxidation behavior of Fe13Cr6AlY alloys under 1200 °C steam. J Alloys Compd. 2023;960:170642.
18. Tang C, Shi H, Jianu A, Weisenburger A, Victor G, Grosse M, et al. High-temperature oxidation of AlCrFeNi-(Mn or Co) high-entropy alloys: Effect of atmosphere and reactive element addition. Corros Sci. 2021;192.
19. Lu Z, Peng S, Li H, Gao S. Improved oxidation resistance of ODS-CrFeNi medium entropy alloys by different Y2O3/Ti/Zr

additions. J Alloys Compd. 2023;960:171017.
20. Polat G, Kotan H. Microstructural Evolution and Mechanical Properties of Y Added CoCrFeNi High-entropy Alloys Produced by Arc-melting. Hittite Journal of Science and Engineering. 2024;11(1):25–31.
21. Polat G, Tekin M, Kotan H. Role of yttrium addition and annealing temperature on thermal stability and hardness of nanocrystalline CoCrFeNi high entropy alloy. Intermetallics. 2022;146:107589.
22. Tekin M, Polat G, Kalay YE, Kotan H. Grain size stabilization of oxide dispersion strengthened CoCrFeNi-Y2O3 high entropy alloys synthesized by mechanical alloying. J Alloys Compd. 2021;887:161363.
23. Gunduz KO, Visibile A, Sattari M, Fedorova I, Saleem S, Stiller K, et al. The effect of additive manufacturing on the initial High temperature oxidation properties of RE-containing FeCrAl alloys. Corros Sci. 2021;188:109553.
24. Hellström K, Israelsson N, Mortazavi N, Canovic S, Halvarsson M, Svensson JE, et al. Oxidation of a Dispersion-Strengthened Powder Metallurgical FeCrAl Alloy in the Presence of O2 at 1,100 °C: The Influence of Water Vapour. Oxidation of Metals. 2015;83(5):533–58.
25. Singh AK, Subramaniam A. On the formation of disordered solid solutions in multi-component alloys. J Alloys Compd. 2014;587.
26. Tripathy B, Malladi SRK, Bhattacharjee PP. Development of ultrafine grained cobalt-free AlCrFe2Ni2 high entropy alloy with superior mechanical properties by thermo-mechanical processing. Materials Science and Engineering: A. 2022;831:142190.
27. Cui P, Liu Y, Zhou F, Lai Z, Zhu J. Enhancing high temperature mechanical properties via modulating B2 phase with Al contents in FeCrNiAlx(x = 0.63,0.71,0.77) high entropy alloys. J Alloys Compd. 2022;903.
28. Zhou Y, Zhou D, Jin X, Zhang L, Du X, Li B. Design of non-equiatomic medium-entropy alloys. Sci Rep. 2018;8(1).
29. Ma Y, Jiang B, Li C, Wang Q, Dong C, Liaw PK, et al. The BCC/B2 morphologies in Al x NiCoFeCr high-entropy alloys. Metals. 2017;7(2):57.
30. Diao G, Wu M, He A, Xu Z, Mousavi SE, Li D. Manipulate A2/B2 structures in AlCrFexNi alloys for improved mechanical properties and wear resistance. Lubricants. 2023;11(9):392.
31. Ren H, Chen RR, Liu T, Gao XF, Qin G, Wu SP, et al. Unraveling the oxidation mechanism of Y-doped AlCoCrFeNi high-entropy alloy at 1100 °C. Appl Surf Sci. 2024;652:159316.
32. Diao G, Wu M, He A, Xu Z, Bajaj D, Chen D, et al. Adjusting (AlNi)/(FeCr) ratio to tailor microstructure and properties of A2-B2 dual-phase (AlNi)x(FeCr)100-x medium-entropy alloys. Journal of Materials Research and Technology. 2025;34:1921–32.
33. Li JL, Li Z, Wang Q, Dong C, Liaw PK. Phase-field simulation of coherent BCC/B2 microstructures in high entropy alloys. Acta Mater. 2020;197:10–9.
34. Field KG, Snead MA, Yamamoto Y, Terrani KA. Handbook on the material properties of FeCrAl alloys for nuclear power production applications. Nuclear Technology Research and Development. 2017;
35. Berthomé G, N'Dah E, Wouters Y, Galerie A. Temperature dependence of metastable alumina formation during thermal oxidation of FeCrAl foils. Materials and Corrosion. 2005;56(6):389–92.
36. Andoh A, Taniguchi S, Shibata T. TEM observation of phase transformations of alumina scales formed on Al-deposited Fe-Cr-Al foils. In: Materials science forum. Trans Tech Publ; 2001. p. 303–10.
37. Chevalier S, Strehl G, Buscail H, Borchardt G, Larpin JP. Influence of the mode of introduction of a reactive element on the high temperature oxidation behavior of an alumina-forming alloy. Part I: Isothermal oxidation tests. Materials and Corrosion. 2004 May 1;55(5):352–7.
38. Tolpygo VK, Clarke DR. Microstructural study of the theta-alpha transformation in alumina scales formed on nickel-aluminides. Materials at High Temperatures. 2000 Jan 1;17(1):59–70.
39. Issartel C, Buscail H, Chevalier S, Favergeon J. Effect of Yttrium as Alloying Element on a Model Alumina-Forming Alloy Oxidation at 1100 °C. Oxidation of Metals. 2017;88(3–4).
40. Lu J, Zhang H, Chen Y, Li L, Liu X, Xiao W, et al. Y-doped AlCoCrFeNi2.1 eutectic high-entropy alloy with excellent oxidation resistance and structure stability at 1000°C and 1100°C. Corros Sci. 2021;180.
41. Wright JK, Williamson RL, Renusch D, Veal B, Grimsditch M, Hou PY, et al. Residual stresses in convoluted oxide scales. Materials Science and Engineering: A. 1999;262(1):246–55.
42. Evans HE. Stress effects in high temperature oxidation of metals. International materials reviews. 1995;40(1):1–40.
43. Echsler H, Martinez EA, Singheiser L, Quadakkers WJ. Residual stresses in alumina scales grown on different types of Fe–Cr–Al alloys: effect of specimen geometry and cooling rate. Materials Science and Engineering: A. 2004;384(1):1–11.
44. Smialek JL. Invited Review Paper in Commemoration of Over 50 Years of Oxidation of Metals: Alumina Scale Adhesion Mechanisms: A Retrospective Assessment. Oxidation of Metals. 2022;97(1):1–50.
45. Whittle DP, Stringer J. Improvements in high temperature oxidation resistance by additions of reactive elements or oxide dispersions. Philosophical Transactions of the Royal Society of London Series A, Mathematical and Physical Sciences. 1997 Jan 1;295(1413):309–29.
46. Naumenko D, Gleeson B, Wessel E, Singheiser L, Quadakkers WJ. Correlation between the Microstructure, Growth Mechanism, and Growth Kinetics of Alumina Scales on a FeCrAlY Alloy. Metallurgical and Materials Transactions A. 2007;38(12):2974–83.
47. Cueff R, Buscail H, Caudron E, Riffard F, Issartel C, El Messki S. Effect of reactive element oxide coating on the high temperature oxidation behaviour of FeCrAl alloys. Appl Surf Sci. 2004;229(1):233–41.
48. Chevalier S, Issartel C, Cueff R, Buscaif H, Strehl G, Borchardt G. Influence of the mode of introduction of a reactive element on the high temperature oxidation behavior of an alumina-forming alloy. Part III: The use of two stage oxidation experiments and in situ X-ray diffraction to understand the oxidation mechanisms. Materials and Corrosion. 2006 Jun 1;57(6):476–83.
49. 49. Abell JS, Harris IR, Cockayne B, Lent B. An investigation of phase stability in the Y2O3-Al2O3 system. J Mater Sci. 1974;9(4):527–37.
50. 50. Lu J, Chen Y, Zhang H, Ni N, Li L, He L, et al. Y/Hf-doped AlCoCrFeNi high-entropy alloy with ultra oxidation and spallation resistance. Corros Sci. 2020;166.
51. 51. Lu J, Li L, Chen Y, Liu X, Zhao X, Guo F, et al. Y-Hf co-doped AlCoCrFeNi high-entropy alloy coating with superior oxidation and spallation resistance at 1100 °C. Corros Sci. 2021;182:109267.

SUPPLEMENTARY INFORMATION

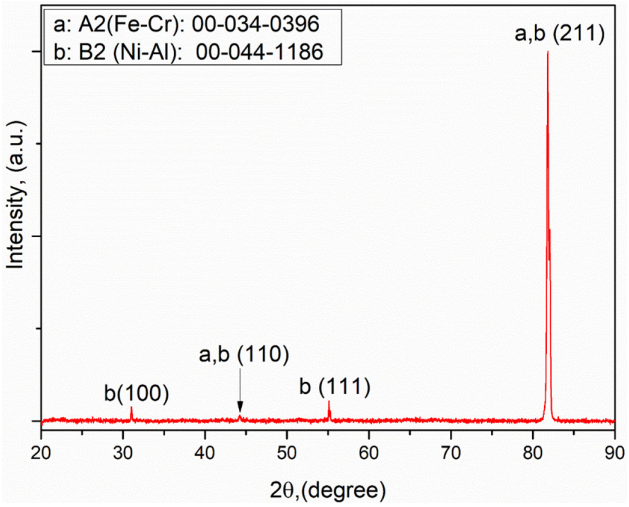

Figure S1. XRD diffractogram of ground and re-analyzed Y-AlCrFeNi alloy.

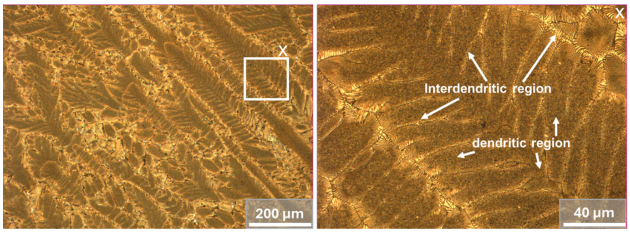

Figure S2. Optical microscope images of etched as-cast Y-AlCrFeNi alloy.

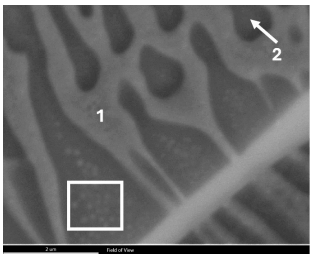

Spot	at.%Fe	at.%Cr	at.%Al	at.%Ni
1(A2)	39.71	43.55	9.77	6.97
2(B2)	15.67	12.54	33.89	37.9

Figure S3. SEM-EDS analysis performed on A2 and B2 phases in the as-cast Y-doped equiatomic AlCrFeNi alloy. Point 1 represents A2 while point 2 represents B2 phase. Note bright precipitates within B2 phase.

Points	Y at.%	Al at.%	O at.%
1	26,86	9.24	63.9
2	35.24	0.87	63.89

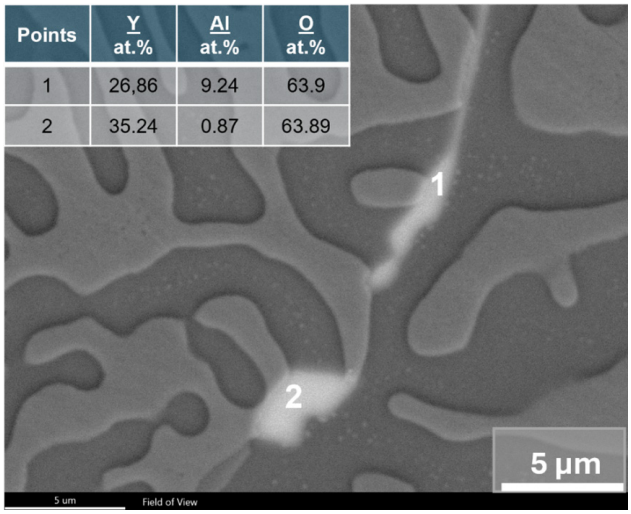

Figure S4. SEM-EDS analysis of internal oxide precipitates located deep within the metal on Y-AlCrFeNi alloy oxidized for 168h at 1100 °C.

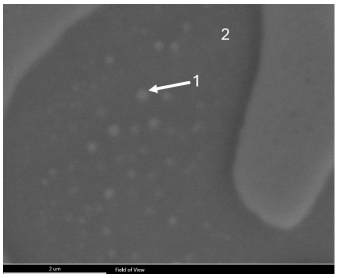

Spot	at.%Fe	at.%Cr	at.%Al	at.%Ni
1	14.77	8.64	39.79	36.8
2	9.09	3.72	43.88	43.31

Figure S5. SEM-EDS analysis performed on bright precipitate (spot 1) and precipitate free region (spot 2) within the B2 phase on the oxidation unaffected region after exposing Y-AlCrFeNi alloy at 1100 °C for 168h.

HITTITE JOURNAL OF SCIENCE AND ENGINEERING

e-ISSN: 2148-4171
Volume: 12 • Number: 1
March 2025

Assessment of the Altering of Tool Wear and Surface Finish in X2CrNiMoN2253 Stainless Steel Under Dry Machining Conditions

Fikret Sönmez
Manisa Celal Bayar University, Hasan Ferdi Turgutlu Faculty of Technology, Department of Mechanical Engineering, Manisa, Türkiye.

Corresponding Author
Fikret Sönmez
E-mail: sonmezfikret@gmail.com Phone: +90 236 314 1010 Fax: +90 236 314 2020
RORID: https://ror.org/053f2w588

Article Information
Article Type: Research Article
Doi: https://doi.org/10.17350/HJSE19030000349
Received: 07.12.2024
Accepted: 10.02.2025
Published: 25.03.2025

Cite As
Sönmez F. Assessment of the Altering of Tool Wear and Surface Finish in X2CrNiMoN2253 Stainless Steel Under Dry Machining Conditions. Hittite J Sci Eng. 2025;12(1):35-41.

Peer Review: Evaluated by independent reviewers working in at least two different institutions appointed by the field editor.
Ethical Statement: Not available.
Plagiarism Checks: Yes - iThenticate
Conflict of Interest: Authors declare no conflict of interest.

CRediT AUTHOR STATEMENT
Fikret Sönmez: Conceptualization, Data curation, Formal Analysis, Investigation, Methodology, Resources, Supervision, Writing – review and editing.

Assessment of the Altering of Tool Wear and Surface Finish in X2CrNiMoN2253 Stainless Steel Under Dry Machining Conditions

Fikret Sönmez

Manisa Celal Bayar University, Hasan Ferdi Turgutlu Faculty of Technology, Department of Mechanical Engineering, Manisa, Türkiye.

Abstract

Machining is a challenging manufacturing method used for precision parts. In this method, tool wear is inevitable and increases constantly. Surface roughness values change caused by tool wear until the tool life is assumed to be complete. In this investigation, tool wear and the effect of tool wear on surface roughness were analyzed. For this purpose, the cutting experiments were performed on stainless steel material under dry machining circumstances at 1 mm depth of cut, 120 m/min cutting speed, and 0.1 mm/rev feed. The tool wear and surface roughness values were inspected at the finish of each operation on the CNC turning center without removing the workpiece. As a consequence of the measurements, it was concluded that the surface roughness values generally deteriorated, and the tool wear increased regularly. Flank wear was found to be the primary type of wear in the experiments, and interestingly, the surface roughness decreased at the end of tool wear. In addition, it was determined that the tool wear reached the limit at the completion of the machining time of 14.4 minutes.

Keywords: Tool wear, Surface roughness, Machining, Hard-to-cut materials

INTRODUCTION

Machining is a method used to fabricate machine components with superior dimensional consistency, tight geometric tolerance, and desired surface roughness [1]. For this reason, machining continues to be used in the production of precision machined parts. Numerous factors influence machining. These factors are typically cutting conditions, cutting tool material, and the material subjected to machining [2]. Although this method has many advantages, it also has unavoidable phenomena such as tool wear. Tool wear is a phenomenon that proceeds according to the cutting circumstances, and increased tool wear affects the workpiece properties, such as surface roughness and geometric tolerance [1, 3]. In addition, tool wear negatively affects machine vibrations and cutting forces [4, 5]. As a result, increased tool wear may lead to tool breakage, resulting in a completely unusable workpiece [6]. Although numerous types of materials can be manufactured through machining, certain materials are somewhat or entirely unsuitable for cutting due to their specific properties. An example of a difficult-to-machine ma terial is s tainless steel. Stainless steel is a poor machining material due to its limited thermal conductivity [7] and vulnerability to strain hardening [1].

Del Risco-Alfonso et al. [8] in studies on AISI 316L stainless steel (austenitic) suggested that cutting speed (200-300-400 m/min) had a direct effect on tool life. Although the feed had a negative effect on tool wear, the main contributor to tool wear was dependent on the cutting speed. In their research, the researchers also pointed out that the differences between Minimum Quantity Lubrication (MQL) and dry cooling conditions were not significant in the experiments. Chen et al. [9] researched the cutting performance of stainless steel (AISI 304) under dry machining conditions using various cutting parameters. The surface finish and tool wear data were examined at certain minutes (6th, 12th, and 18th) throughout the experiments. The cutting tool showed insignificant wear initially, but the amount of wear accelerated later, and excessive tool wear was detected at the 18th minute. The scientists found that this wear caused the surface finish quality values to decrease by almost 14 times. He et al. [10] researched AISI 304 and demonstrated that the rate of rise in cutting tool wear changed from being initially rapid, then increasing steadily, and eventually rapidly increasing. The third zone, where the tool wear values increase rapidly, depends on the cutting circumstance, and can fluctuate up to fivefold. In addition, it has been revealed that wet cutting conditions delay tool wear and reduce cutting forces. Ebrahimi et al. [11] assessed cutting tests on AISI 360 stainless steel material. The researchers analyzed tool life and surface finish values during cutting. Cutting speed and feed were found to have a direct manipulation on the tool wear. The researchers also encountered that, using properly selected parameters, the flank wear and surface roughness values lessened by 33 percent and 23 percent, respectively. Szczotkarz et al. [12] employed turning experiments with AISI 316L steel under a variety of cutting parameters to investigate flank and crater wear values. The researchers benchmarked dry cutting with two cooling conditions (MQL and Minimum Quantity Cooling Lubrication (MQCL) with the addition of extreme pressure and anti-wear (EP/AW) method), and as a result, the researchers obtained up to 21% better tool wear values assessed to dry machining. The researchers emphasized that the cutting insert wear patterns were changed depending on the cooling conditions, especially the notch wear. Zawada-Michałowska et al. [13] performed tool wear tests on X20Cr13 and X8CrNiS18-9 stainless steels. The researchers also used three different cutting inserts in these experiments and achieved up to 75% worse tool life depending on the cutting insert used. In addition, the researchers unveiled that the surface finish values changed dramatically depending on the type of cutting insert.

In the literature review, it was comprehended that the machining of various types of stainless steel was discussed. However, limited research [14] was found in the literature on X2CrNiMoN2253, even though X2CrNiMoN2253 duplex stainless steel is a prominent material used across various industries (chemical, marine, oil, and gas) and applications due to its outstanding combination of high strength, remarkable toughness, and superior corrosion resistance. In addition, a comprehensive examination of the variation in tool wear over time and the variation of the workpiece surface roughness associated with the alteration of tool wear has not been found.

In this study, turning experiments and tool wear analysis were

applied under dry machining conditions on X2CrNiMoN2253, a duplex, hard-to-cut stainless steel used for manufacturing many turning applications parts such as fittings, containers, storage tanks, pipelines, press rolls, and rotary shafts. Besides, the role of tool life in altering the surface finish of the workpiece was extensively investigated.

MATERIAL AND METHODS

In the present investigation, tool wear and surface roughness studies were completed on Ø61 mm x 110 mm duplex stainless steel (X2CrNiMoN2253). Table 1 lists the elemental content of the material employed in this study.

Table 1. The chemical composition of X2CrNiMoN2253 materials.

Element	Cr	Ni	Mo	Mn	C	Si	P	S	Fe
wt.%	22.69	4.84	3.11	1.40	0.015	max 1	max 0.035	max 0.015	Balance

The turning experiments were conducted using a universal-grade (TP2500) cutting insert (TNMG 160404-M3) suitable for P, M, and K-grade materials manufactured by SECO Company. The geometric information of the tungsten carbide (WC) based cutting insert is as follows: cutting edge length 16.50 mm, effective cutting edge length 14.50 mm, corner radius 0.80 mm, and insert thickness 4.76 mm. The cutting insert is suitable for light to medium impact cutting conditions (P25-Grade) and CVD (chemical vapor deposition) coated with (C, N) + Al_2O_3. Cutting tools with an approach angle of 90° are generally used due to their ability to perform both longitudinal turning and face turning. In addition, a tool holder with a 90° approach angle (PTGNR 2020K16) was chosen (Figure 1). ISO 3685 standard [15] was used to determine the turning parameters. The selected values are presented in Table 2.

Table 2. The cutting conditions.

Parameter	Value
Cutting speed	120 m/min
Depth of cut	1 mm
Feed	0.1 mm/rev
Cutting insert nose radius	0.4 mm

It is a well-known fact that the cooling environment, such as cutting fluids, greatly reduces tool wear. Therefore, all experiments were executed under dry-cutting conditions to better observe tool wear. The workpiece was turned in 13 passes, starting from Ø61 mm down to Ø35 mm. The cutting length was determined as 90 mm in each pass. Depending on the changing workpiece diameter, various cutting times were obtained in each pass (Table 3).

The turning experiments were continued for 14.4 minutes until the tool life was finalized (Table 3), a nd t he o utput quantities (surface roughness and tool wear) were measured after the completion of all passes. The tool wear examinations were carried out by measuring both flank wear and notch wear values in a toolmaker's microscope (Mahr MM200). In addition to the toolmaker's microscope examination, the cutting tools were inspected by SEM-EDX after the termination of all experiments (Zeiss GeminiSEM 500). The surface roughness records were assessed in compliance with the ISO 21920-3:2021 (previously ISO-4288) standard [15]. The surface roughness measurements (Ra, Rz, and Rt) were repeated over five runs around the workpiece (Figure 1).

Table 3. The total cutting length and cutting time for the cutting insert.

Pass	Total cutting length (mm)	Total cutting time (min)	Pass	Total cutting length (mm)	Total cutting time (min)
1	90	1.39	8	720	9.8
2	180	2.73	9	810	10.82
3	270	4.03	10	900	11.78
4	360	5.28	11	990	12.7
5	450	6.48	12	1080	13.57
6	540	7.64	13	1170	14.4
7	630	8.74	Total	1170	14.4

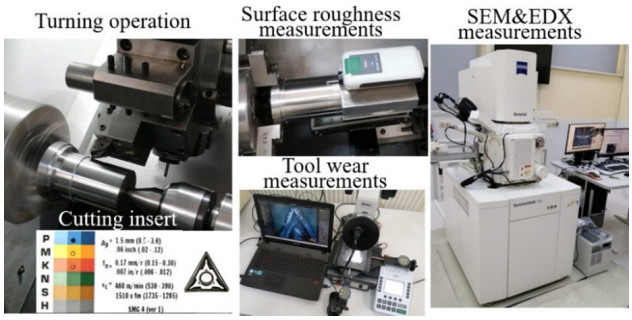

Figure 1. The experimental order.

RESULTS AND DISCUSSION

Tool Wear

During machining, cutting tools are affected by numerous factors and wear over time. As a result, various wear mechanisms appear on the cutting tool, and different wear types develop as a result of these wear mechanisms. Ultimately, the cutting tool becomes unusable after a certain period. In the research, the wear of the tool over time was studied. The measurements for the different passes (1st, 5th, 10th, and 13th) are given in Figure 2.

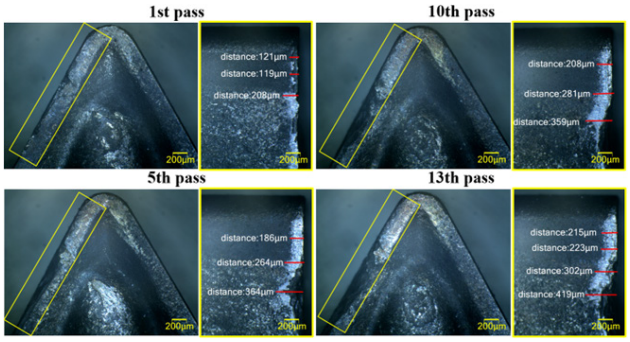

Figure 2. The tool wear examinations with the toolmaker's microscope.

Instead of a single wear mechanism, tool wear frequently consists of multiple wear mechanisms [16]. However, in this study, it is understood that abrasion wear (three-element abrasion wear) is dominant on the cutting tool, and abrasion marks are obvious (Figure 2). Over time, abrasion has caused flank wear and notch wear. Therefore, tool life analyses have been studied based on these two types of wear. CNC turning centers were frequently employed with single-point cutting tools, and ISO 3685 was applied to control the tool life [17]. In the current examination, the cutting tool wear was found to be regular, as shown in Figure 2. Consequently, a value of 300 µm was used to determine the flank wear limit value according to ISO 3685. The limit value was reached on the 13th pass (14.4 min cutting tool life); hence, the tool was considered worn, and the experiments were terminated. In their study, Letot et al. [18] detected 300 µm flank wear approximately after 10-14 minutes of cutting time. In addition, tool wear was monitored until the end of the time when the tool was considered worn (until the end of the 13th operation), and the tool wear was monitored by performing measurements after each operation (Figure 3).

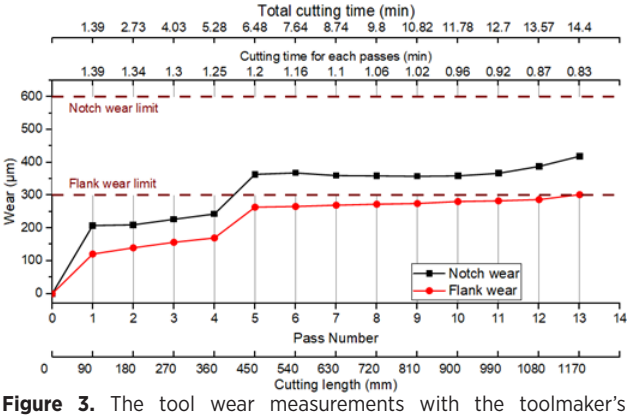

Figure 3. The tool wear measurements with the toolmaker's microscope.

The time-dependent tool wear shown in Figure 3 was examined. In the first pass, where the experiments started, there was a rapid increase in the notch wear and flank wear values. In all subsequent passes, the notch wear value was found to be higher than the flank wear value throughout all the tests. It is known that the notch wear moves faster when it is related to the flank wear [19]. Tool wear increased with time, as expected. It was known that cutting tools wear rapidly at the beginning, then continue to wear at a steady rate, and in the final stage, wear accelerates again; this was relatively ordinary in tool life curves in general [18, 19]. However, as the diameter of the material decreased with each pass, the cutting time decreased with each pass. The cutting time in the first pass was 1.39 minutes, while the cutting time in the last pass was 0.83 minutes. Therefore, the acceleration of tool wear was not developed as fast as expected. It was understood that the tool wear was slowed down considerably, especially in the last few passes. The machining operations were performed with a total length of 1170 mm within 14.4 minutes when the tool life was finalized, and the investigations were terminated due to tool wear. Finally, the worn cutting tools were monitored by SEM and EDX investigations (Figure 4).

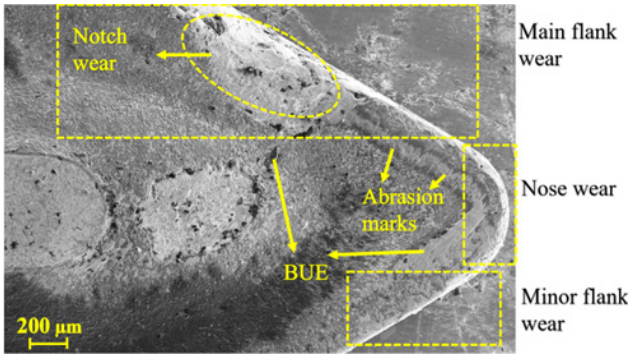

Figure 4. The tool wear measurements with the SEM.

The SEM examination was performed on the insert (Figure 4). Although flank wear and notch wear were detected in the microscopic examination, Built-up edge (BUE) formation and nose wear were also observed in the SEM analysis. However, since the surface examination did not provide sufficient information on insert wear, the insert was examined from an oblique view (Figure 5).

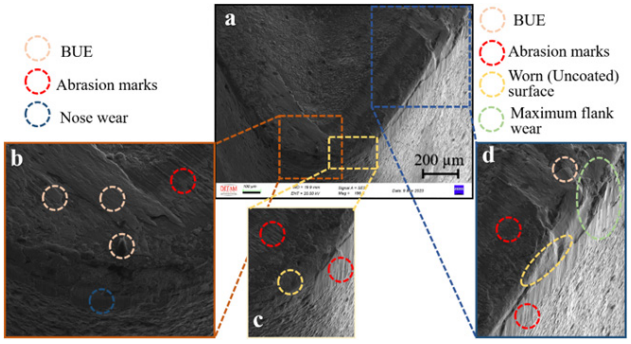

Figure 5. The SEM analysis according to the types of wear.

The SEM image (Figure 5) of the cutting tool was examined. The abrasive wear mechanism was apparent on all surfaces of the cutting tool that encountered the workpiece (Figures 5-b, 5-c, and 5-d). Both BUE formation and nose wear were evident in Figure 5-b, which shows the nose area of the cutting tool was presented. BUE formation is frequently observed in the literature [20]. Figure 5-d shows the surface where the cutting tool first encounters the workpiece. Since thermal cracks and crater wear are not observed, it can be argued that the wear is only due to mechanical effects. This surface showed significant wear due to three-element abrasion wear. The cutting tool was coated with Ti (C, N) and Al_2O_3 coating layers employing the Chemical Vapor Deposition (CVD) method. Coatings have many advantages in cutting tools, especially in extending tool life. However, as can be clearly detected in Figure 5-d, the coating on the cutting tool is largely removed as expected due to tool-workpiece interaction. Notch wear, which is frequently encountered in cutting tools, was partially visible in the tool. A SEM&EDX analysis was performed to obtain more information about the cutting tool surface (Figure 6).

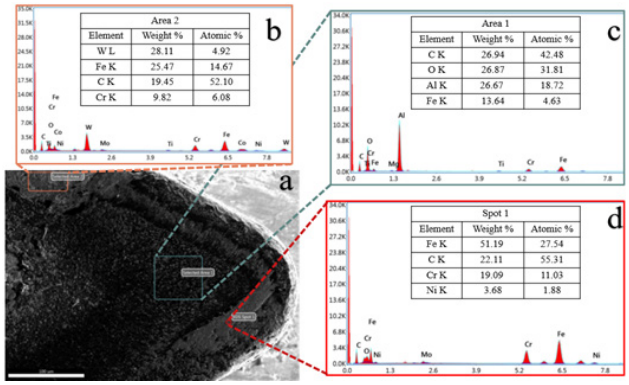

Figure 6. The EDX analysis of the top surface of the cutting insert.

The EDX investigations were operated on three different regions of the cutting insert (Figure 6-a). In Figure 6-b, where notch wear was observed, the presence of W and C atoms in the chemical composition showed that the cutting tool coating was completely worn, and the WC (tungsten carbide) substrate, which was expected to be seen in the substrate, became visible. Figure 6-c shows the chemical composition analysis taken from the area where there was no direct interaction between the workpiece and the cutting insert. Ti (C, N) and Al_2O_3, which were used in the cutting insert coatings, were expected to be seen in this area. The existence of Al, O, and C elements, as expected, indicated an unworn cutting tool coating. The presence of Cr and N elements, mostly related to the content of the workpiece material (stainless steel), in the last examination area (Figure 6-d), proves the formation of BUE in this examination.

Surface Roughness

Machine parts coming out of the machining process are expected to have certain qualities. One of these qualities is surface finish. In the present study, surface finish investigations were performed after each pass, and the average surface roughness (Ra) values presented in Figure 7 were obtained.

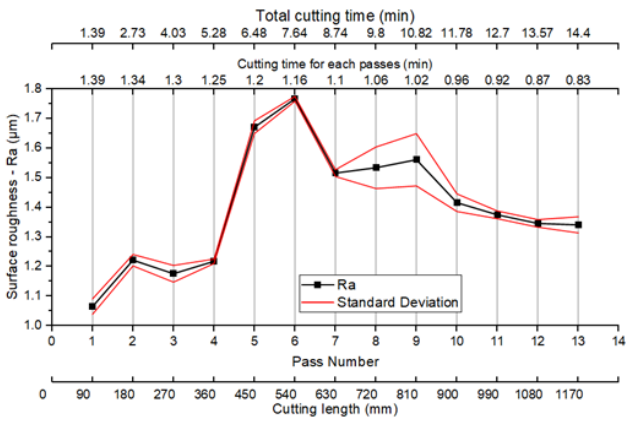

Figure 7. The surface roughness (Ra) results of the machined workpiece.

The surface roughness results were calculated by averaging a total of five measurements without dismounting the workpiece from the CNC lathe. Therefore, it is intended to increase the reliability of the measurement. In addition, the surface roughness measurement area is kept constant for each pass by using the C-axis capability of the turning center. It was reported in the literature that the surface roughness values deteriorate because of tool wear [2, 9, 21]. In the surface roughness measurements, a rapid increase in surface roughness as a factor of tool wear was monitored. Furthermore, it was also found that the standard deviation of these measurements was also low. However, after 7.64 minutes of tool life (after the 6th pass), the surface roughness measurements decreased interestingly until the end of the experiments. Some literature sources also highlighted this intriguing circumstance, and the researchers showed that the surface finish of the machined surface could increase as the tool life was near its end [19, 22]. The geometric shape of the cutting inserts transforms under the influence of tool wear. It was recognized that the two dominating influences on surface roughness were feed and tool geometry [23, 24]. It is also known that wiper cutting inserts are employed in some cutting tools to provide a smoother surface finish [3, 25]. The decrease in surface roughness can be explained in several ways. The tool nose radius directly affected the surface roughness; increased tool wear increased the tool nose radius, and increased tool nose radius decreased the surface roughness. Moreover, the geometrical change of the cutting insert could make a wiper tool effect to decrease the surface roughness. The coated layer of the tool is significantly harder than the substrate; therefore, a burnishing effect rather than a cutting effect could affect the surface roughness. Moreover, there were meaningful standard deviation differences in tool wear on the 8th and 9th passes. Since the feed was kept constant in all experiments, the change in surface roughness can only be explained by tool wear. Tool wear is affected by many factors; however, machining time or machining length can be defined as the main reason for the increasing tool wear [26,27]. In this case, while the increase in surface roughness due to tool wear was expected, the enhancement in surface roughness at the end of 7.64 minutes of tool life could be explained by the transformation of the worn tool surface into a geometry similar to wiper cutting inserts. In the evaluation of surface roughness, in addition to the average surface roughness parameter, the Rz and Rt parameters were also measured to better express the surface roughness (Figure 8).

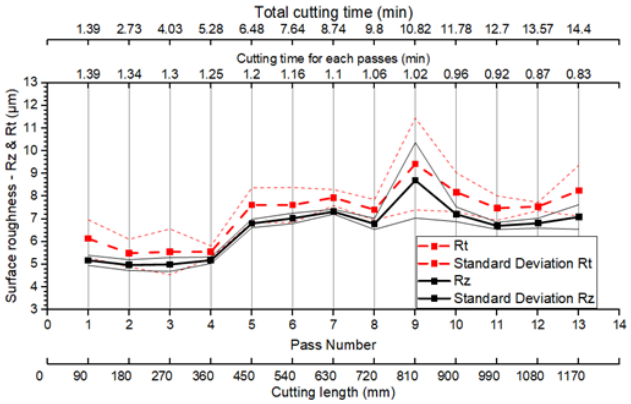

Figure 8. The surface roughness (Rz and Rt) results of the machined workpiece.

Similar to the Ra parameter, both the Rz and Rt parameters

deteriorated due to tool wear (Figure 8). However, the enhancement in surface roughness seen in the Ra parameter after 7.64 minutes of tool life (at the end of the 6th pass) was interestingly not observed in the Rz and Rt measurements. In addition, as expected, the Rt parameter was higher than the Rz parameter in all experiments. Elba et al. [3] emphasized in their study that Rz and Rt were almost 5-6 times higher than Ra. Similarly, in this study, the Rz value was 4.67 times the Ra, and the Rt value was 5.2 times the Ra. After the tool life of 10.82 minutes (9th pass), it was discovered that there was a very significant standard deviation, similar to the Ra measurement. The entire surface roughness investigation examined and understood that both surface roughness values (Rz and Rt) deteriorate extensively with time.

CONCLUSION

In the current study, the tool wear and surface roughness changes in the turning of stainless steel were analyzed under dry machining conditions. For this purpose, the constant length of the workpiece (90 mm) was machined each time, and surface roughness and tool wear measurements were studied at the end of each cutting operation. The primary outcomes of these analyses were as follows:

Distinct types of wear, particularly notch and flank w ear, were monitored. The wear values increased with time and the tool life ended at the end of 14.4 minutes of machining time (1170 mm) when the flank wear value reached 300 µm. It was observed that both the flank wear and notch wear values intensified swiftly and then intensified at a steady rate. However, the third stage of tool wear, which was frequently seen in cutting tools and in which the cutting tool wears rapidly, has not been determined. In addition, significant BUE formation was revealed by SEM and EDX analysis.

To analyze the surface roughness values, in particular, the Ra parameter, the Rz and Rt parameters were also examined. It was observed that the Ra parameter first deteriorated due to tool wear, but after 7.64 minutes of cutting time, it interestingly improved until the end of 14.4 minutes when the experiments were completed. However, interestingly, this improvement was not observed for the Rz and Rt parameters.

Considerable detailed studies were conducted within the scope of this study. However, towards the end of the experiments, it was not entirely clear why the Rz and Rt parameters did not increase while the Ra parameter increased. An investigation of this situation may be interesting for future studies. In addition, conducting current experiments with wiper inserts and comparing the results can contribute to the literature.

Acknowledgement

The author received no financial support for the research, authorship, and/or publication of this article.

References

1. Stephenson DA, Agapiou JS. Metal cutting theory and practice. 3rd Ed. Boca Raton FL, USA, CRC Press, 2018.
2. Pinar AM, Fırat K. Machinability evaluation of multi-directional turning tools. Materials Testing. 2020 Feb 25;62(3):311-316.
3. Elbah M, Yallese MA, Aouici, H., Mabrouki, T., Rigal, J.-F. Comparative assessment of wiper and conventional ceramic tools on surface roughness in hard turning AISI 4140 steel. Measurement. 2013 Jun 26;46(9):3041-3056.
4. Huang YW, Yeh SS. Development of insert condition classification system for CNC lathes using power spectral density distribution of accelerometer vibration signals. Sensors (Basel). 2020 Oct 19;20(5907):1-20.
5. Tzotzis A, García-Hernández C, Huertas-Talón J-L, Kyratsis P. 3D Fe modelling of machining forces during AISI 4140 hard turning. Strojniški vestnik – Journal of Mechanical Engineering. 2020;66(7-8):467-478.
6. Sousa VFC, Silva FJG. Recent advances in turning processes using coated tools—a comprehensive review. Metals. 2020 Jan 23;10(170):1-28.
7. Callister Jr, WD, Rethwisch DG. Callister's materials science and engineering. 10th ed, New York, USA, John Wiley & Sons, 2020.
8. Del Risco-Alfonso R, Pérez-Rodríguez R, Zambrano Robledo, PdC, Rivas Santana M, Quiza R. Optimization of the cutting regime in the turning of the AISI 316L steel for biomedical purposes based on the initial progression of tool wear. Metals. 2021 Oct 25;11(1698):1-15.
9. Chen J, Wang Y, Zhang Y, Yang S, Zhang X. Investigation on tool wear mechanism during dry cutting 304 stainless steel. Manufacturing Technology. 2020 Jul 31;20(1):36-44.
10. He Q, DePaiva JM, Kohlscheen J, Veldhuis SC. Analysis of the performance of pvd altin coating with five different Al/Ti ratios during the high-speed turning of stainless steel 304 under dry and wet cooling conditions. Wear. 2022 Dec 8;492-493:204-213.
11. Ebrahimi SM, Hadad M, Araee A. Sustainable machining of hardened AISI630 stainless steel using thermally enhanced turning technique. Mach. Sci. Technol. 2021 May 14;25(4):608-636.
12. Szczotkarz N, Mrugalski R, Maruda RW, Królczyk GM, Legutko S, Leksycki K, Dębowski D, Pruncu CI. Cutting tool wear in turning 316L stainless steel in the conditions of minimized lubrication. Tribol Int. 2021 Dec 5;156(106813):1-11.
13. Zawada-Michalowska M, Piesko P, Jozwik J. Tribological aspects of cutting tool wear during the turning of stainless steels. Materials (Basel). 2019 Dec 26;13(123):1-12.
14. Sönmez F. The effect of feed and depth of cut parameters on surface roughness and chip morphology in stainless steel materials. European Journal of Technique (EJT). 2024 Jun 30;14(1), 69-75.
15. ISO 21920-3:2021. Geometrical product specifications (GPS) - Surface texture: Profile — Part 3: Specification operators, International Organization for Standardization. Geneva, 2021.
16. Singh Bedi S, Prasad Sahoo S, Vikas B, Datta S. Influence of cutting speed on dry machinability of AISI 304 stainless steel. Mater Today Proc. 2021 Jun 27;38: 2174-2180.
17. ISO 3685:1993. Tool-life testing with single-point turning tools, International Organization for Standardization. Geneva, 1993.
18. Letot C, Serra R, Dossevi M, Dehombreux P. Cutting tools reliability and residual life prediction from degradation indicators in turning process. Int J Adv Manuf Technol. 2015 Dec 16;86(1-4):495-506.
19. Derani MN, Ratnam MM, Nasir RM. Improved measure of workpiece surface deterioration during turning using non-contact vision method. Precis Eng. 2021 Dec 23;68:273-284.
20. Pekşen H, Kalyon A. Optimization and measurement of flank wear and surface roughness via Taguchi based grey relational

analysis. Materials and Manufacturing Processes, 2021 May 14;36(16):1865-1874.
21. Parsi PK, Kotha, RS, Routhu T, Pandey S, Dwivedy M. Machinability evaluation of coated carbide inserts in turning of super-duplex stainless steel. SN Appl Sci. 2020 Oct 31;2(1933):1-19.
22. Akhavan Niaki F, Mears L. A comprehensive study on the effects of tool wear on surface roughness, dimensional integrity and residual stress in turning IN718 hard-to-machine alloy. J Manuf Process. 2017 Oct 2;30:268-280.
23. Baday Ş, Ersöz O. Comparative investigations of cryo-treated and untreated inserts on machinability of AISI 1050 by using response surface methodology, Anova and Taguchi design. Proc. Inst. Mech. Eng., Part C. 2021 Agu 28;236(3):1751-1765.
24. Rashid WB, Goel S, Davim JP, Joshi SN. Parametric design optimization of hard turning of AISI 4340 steel (69 Hrc). Int J Adv Manuf Technol. 2015 Jun 13;82(1-4):451-462.
25. Subbaiah KV, Raju C, S Pawade R, Suresh C. Machinability investigation with wiper ceramic insert and optimization during the hard turning of AISI 4340 steel. Mater Today Proc. 2019 Oct 28;18:445-454.
26. De Oliveira PA, de Menezes Pereira LMP, Monção RM, *et al.* Tool wear, surface roughness, electric current, and chip morphology in the turning of AISI 1045 steel with minimum quantity lubrication (MQL) technique. Int J Adv Manuf Technol. 2024 Jul 08;133;5743–5759.
27. Bouchama R, Bouhalais ML, & Cherfia A. Surface roughness and tool wear monitoring in turning processes through vibration analysis using PSD and GRMS. Int J Adv Manuf Technol. 2024 Jan 05;130;3537–3552.

HITTITE JOURNAL OF SCIENCE AND ENGINEERING

e-ISSN: 2148-4171
Volume: 12 • Number: 1
March 2025

Electronic Detection of Garlic Density in Various Kinds of Yogurts Using Statistical Features

Bilge Han Tozlu
Hitit University, Engineering Faculty, Department of Electrical and Electronics Engineering, Corum, Türkiye.

Corresponding Author
Bilge Han Tozlu
E-mail: bilgehantozlu@hitit.edu.tr Phone: +90 364 219 12 00 - 13 06 Fax: +90 364 219 13 10
RORID: https://ror.org/01x8m3269

Article Information
Article Type: Research Article
Doi: https://doi.org/10.17350/HJSE19030000350
Received: 06.01.2025
Accepted: 28.02.2025
Published: 25.03.2025

Cite As
Tozlu BH. Electronic Detection of Garlic Density in Various Kinds of Yogurts Using Statistical Features. Hittite J Sci Eng. 2025;12(1):43-50.

Peer Review: Evaluated by independent reviewers working in at least two different institutions appointed by the field editor.
Ethical Statement: Not available.
Plagiarism Checks: Yes - iThenticate
Conflict of Interest: Authors declare no conflict of interest.

CRediT AUTHOR STATEMENT
Bilge Han Tozlu: Conceptualization, Data curation, Formal Analysis, Investigation, Methodology, Resources, Supervision, Writing – review and editing.

Electronic Detection of Garlic Density in Various Kinds of Yogurts Using Statistical Features

Bilge Han Tozlu

Hitit University, Engineering Faculty, Department of Electrical and Electronics Engineering, Corum, Türkiye.

Abstract

Accurate detection of food components plays a critical role in developing modern culinary technologies and food safety practices. This study uses electronic nose technology to determine garlic concentration in garlic yogurts. An electronic nose system consisting of 11 different MQ brand gas sensors was used in the study. Five different yogurt types were prepared with three different garlic concentrations: plain, low, and high. A total of 225 odor records were taken from 15 yogurt samples, and various features were extracted from these data, which were analyzed using four different classification algorithms. The Extra Trees algorithm was the most successful method, with 89.14% classification accuracy, 89.80% sensitivity, and 94.57% specificity rates. The results of the study show that electronic nose technology can be used in many application areas, especially in smart kitchen devices analyzing food ingredients to provide information about freshness and composition, in the food industry to ensure standardization of product quality in production processes and to ensure that intense aromatic ingredients such as garlic are used in the right amount, and in the development of food products suitable for consumers' special diets or personal tastes.

Keywords: Garlic yogurt, Odor classification, Electronic nose, Extra trees algorithm

INTRODUCTION

In today's world, electronic systems can do many tasks, and odors can be detected electronically. Systems that do this job are called electronic nose (e-nose) systems. Although Alexander Graham Bell first proposed measuring odor in 1914 [1], Moncrieff conducted the first study to develop a device to detect odors in 1961 [2]. E-noses were invented by imitating the human odor detection system. A simulation of e-nose and human olfactory systems is given in Figure 1 [3].

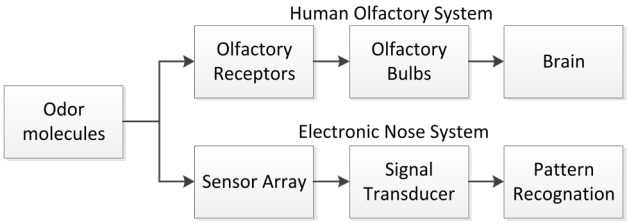

Figure 1. E-nose and human olfactory systems

Many studies have been carried out in food, health, and chemistry with e-nose, which has developed and increased in prevalence over the last 20-30 years.

Many studies have been conducted, from studies on perfume identification with e-noses in chemistry [4] to applications such as air quality monitoring, odor detection, and industrial emission control in environmental engineering [5].

Studies in the health field detect many diseases by using exhaled breath. Studies have been carried out on breathing diagnosis of many diseases using electronic noses, especially lung cancer [6], asthma [7], heart attack [8], diabetes 9], kidney diseases [10], and urinary tract infections [11].

Numerous studies have also been conducted in the field of food and beverages. There are many studies on detection by using an e-nose in food and beverages, such as tea [12], fruit juice [13] in quality determination studies; fish [14], cheese [15] in species identification studies; meat [16], milk [17] in spoilage studies; coffee [18], yogurt [19] in flavor determination studies; seafood [20], and chicken [21] can be given as examples in freshness determination studies.

There are studies in the literature using electronic noses on yogurt and garlic. Li Qiu et al. created a total of 12 different yogurt samples by taking three glasses from four different types of yogurt (plain and flavored). These samples contained 0.1%, 0.3% and 0.5% Rosa rugosa cv. Plena extract (RPE). The researchers classified these samples with a commercial electronic nose branded i-nose. They determined that flavored yogurts' smell differed from plain yogurt's [22]. In the other study, Kaur and his colleagues first examined the effect of yogurt on removing sulfur volatiles formed in the breath after garlic consumption and the role of yogurt components in this process [23]. They then examined the ability of yogurt and its components to deodorize raw and fried garlic volatiles, where they detected the volatile compounds formed after garlic consumption with an electronic nose and evaluated the effect of yogurt on these compounds [24]. In another application, Tamaki and his colleagues analyzed the odor components formed after consumption of raw and heated garlic in laboratory environments and living organisms (in vitro and in vivo) using e-nose. They found that raw and heated garlic had different olfactory characteristics in the breath and laboratory environment [25]. In such a study, using an electronic nose, Suarez and his colleagues investigated whether the source of the gases formed in the breath after garlic consumption was the mouth or the intestine. They also found that gases such as methanethiol and allyl mercaptan were found in high concentrations in the mouth, and allyl methyl sulfide was of intestinal origin [26]. In a study conducted on this subject, Makarechian et al. also evaluated the effects of different desiccation methods and pre-storage times on the aroma of garlic by using an electronic nose [27]. In a similar study, Liu et al. studied drying characteristics, quality changes, parameter optimization, and aroma analysis of garlic slices dried by microwave vacuum drying method with an electronic nose [28].

This study focuses on determining the amount of garlic in garlic yogurt, frequently used in kitchens, using electronic nose technology. Various studies have been conducted on yoghurt and garlic using electronic nose in the literature. In these studies, the classification of different aromas and components of yoghurt was examined. In addition, the effect of yoghurt consumption on volatile compounds of garlic was investigated. In addition, changes in the aroma of

garlic depending on drying and processing methods were also evaluated. However, no study has directly determined the amount of garlic in yogurt via an electronic nose. In this context, this study provides an essential innovation for quantitatively analyzing garlic yogurts and the future use of such a device in innovative kitchen technologies. This method provides a practical solution, especially regarding the rapid and accurate detection of food components.

MATERIALS AND METHODS

This section explains the design of the electronic nose system, data collection processes, feature extraction methods and classification procedures in detail.

Building of the Used Electronic Nose System

The sensor block of the electronic nose built for the study was produced using the gas sensors listed in Table 1, together with their kits.

Table 1. Used Gas Sensors

No	Sensor Model	Sensed Gases	Sensitivity Range (ppm)
1	MQ-2	Methane, Butane, LPG, Smoke	300-10000
2	MQ-3	Alcohol, Ethanol, Smoke	10-1000
3	MQ-4	Methane, CNG Gas	200-10000
4	MQ-5	Natural Gas, LPG	200-10000
5	MQ-6	LPG, Butane Gas	200-10000
6	MQ-7	Carbon Monoxide	20-2000
7	MQ-8	Hydrogen Gas	100-10000
8	MQ-9	Carbon Monoxide, Flammable Gasses	10-10000
9	MQ-131	Ozone	10-1000
10	MQ-135	Air Quality (CO, Ammonia, Benzene, Alcohol, Smoke)	10-1000
11	MQ-137	Ammonia	10-100

MQ brand gas sensors were used with their own electronic kits. Gas sensors collected on a single card were placed in a storage container with a lid. The sensors' cables inside the box were brought out through a narrow airtight hole. The sensor kits were powered by a power supply, and the analog signal taken from the sensors was connected to the two Arduino Uno cards' analog inputs. Sensor output analog data was converted into digital data with Arduino cards and transmitted to the computer via the USB port. Sensor data were recorded using the software prepared in LabView. The e-nose system made for the study is given in Figure 2.

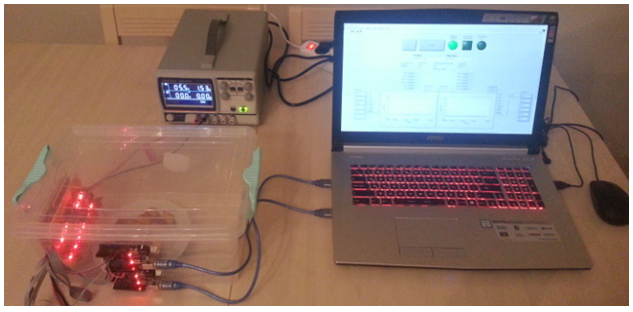

Figure 2. The electronic nose setup

Data Collection and Preprocessing Phase

In this study, five different types of yogurt were used. One hundred fifty grams of each of these yogurts were taken into a bowl. One bowl was left as plain yogurt. Two cloves of garlic were added to one of the other yogurt samples to make yogurt with less garlic. Five cloves of garlic were added to another sample to make yogurt with more garlic. These three different samples for a type of yogurt are shown in Figure 3.

Figure 3. Yogurt samples

The obtained yogurt samples were placed in the olfactory box of the electronic nose, and 15 odor records were taken from each one. The number of odor recordings taken is given in Table 2.

Table 2. Number of sniffing data

	Plain yogurt	Two cloves of garlic yogurt	Five cloves of garlic yogurt
Homemade yogurt	15	15	15
Light yogurt	15	15	15
Strained yogurt	15	15	15
Full-fat skimmed yogurt	15	15	15
Pan yogurt	15	15	15

All measurements were taken for 3 days, with freshly prepared samples, between 20:00-23:00, under 24-26 °C temperature and 50-70% humidity. The sniffing cycle begins by placing the yogurt sample in a ventilated e-nose odor box, closing the box lid, and launching the odor recording software. The e-nose sniffing cycle duration was 30 seconds, and 10 data were received from the sensors per second. Three hundred one data were recorded from a gas sensor in each round, and an 11x301 data matrix was obtained in one sniffing cycle. As seen in Table 2, 225 separate odor records were taken, resulting in a three-dimensional matrix with dimensions of 225x11x301.

In the preprocessing part, some gaps (missing values) were detected in the datasets obtained from the Arduino device during the data collection process. Missing values in the dataset were filled using neighboring non-zero values, ensuring the dataset's suitability for analysis. This method

ensured that the missing data was estimated as accurately as possible and data integrity was maintained.

Feature Extraction Phase

The features of the received data were first extracted. Statistical values such as mean value, standard deviation, total, median, minimum, maximum, first quartile, and third quartile are used here, and their formulas are given in 1-8:

Here, x_{mean} is the mean value of a trial, x_{std} is the standard deviation value of a trial, x_{sum} is the total value of a trial, x_s is the last value of a trial, s is the value number of a trial, x_{median} is the value in the middle of a trial, x_{min} is the minimum value of a trial, x_{max} is the maximum value of a trial, x_{Q1} is the value in the 25% slice when a trial is sorted, that is, the 1st quarter (Q1) value, x_{Q3} is the value in the 75% slice when a trial is sorted, that is, the 3rd quarter (Q3) value.

$$x_{mean} = \sum_{x=1}^{s} \frac{x_1 + x_2 + \cdots + x_s}{s} \quad (1)$$

$$x_{std} = \sqrt{\frac{(x_1 - x_{mean})^2 + \cdots + (x_s - x_{mean})^2}{s-1}} \quad (2)$$

$$x_{sum} = x_1 + x_2 + \ldots + x_s \quad (3)$$

$$x_{median} = \begin{cases} x_{\frac{s+1}{2}} \\ \frac{1}{2}\left(x_{\frac{s}{2}} + x_{\frac{s}{2}+1}\right) \end{cases} \quad (4)$$

$$x_{min} = min(x_1, x_2, \ldots, x_s) \quad (5)$$

$$x_{max} = max(x_1, x_2, \ldots, x_s) \quad (6)$$

$$x_{Q1} = Percentile(x, 25) \quad (7)$$

$$x_{Q3} = Percentile(x, 75) \quad (8)$$

Classification Phase

In the classification process, not all features have the same meaning. In addition to critical features, unimportant features have also been produced. All these reduce the classification accuracy and add a burden to the calculation. Therefore, it is necessary to separate unimportant features and use essential features. In this study, feature selection was done using the Recursive Feature Elimination (RFE) method. Feature selection based on the Random Forest classifier was performed using the RFE method. The number of features to be selected was determined using the cross-validation method.

After selecting the features, the data were randomly selected as training, validation, and test data with a ratio of 60%-20%-20%, respectively. The classification was performed with four different classification algorithms.

Then, the test data were classified using these features by the most common classification algorithms: k-nearest Neighbor (kNN), Random Forest, Extra Trees, and Gradient-Boosting classification algorithms.

The kNN classification method is widely used and very useful in classification studies. In kNN classification, the distances between the data are calculated. Test data is classified according to its k nearest neighbors. The ideal k number was determined by the cross-validation method [29].

Random Forest is a standard classification method that makes decisions with multiple decision trees. Each tree is trained using randomly selected features for a random subset of the data. This method determines the final classification decision by a majority vote of the trees. Thus, thanks to the diversity of trees, the risk of overlearning decreases, and generalization ability increases [30].

The Extra Trees classification method is similar to Random Forest, except that it trains each tree on the entire dataset. Split points are chosen completely randomly. Because of this, trees are more diverse, and training times are generally faster. This method also prevents overlearning due to high randomness. The splitting criteria may be the Gini coefficient or entropy, but the splitting points are randomly chosen [31].

The Gradient Boosting method is one in which weak learners (usually decision trees) are trained sequentially by expanding additively and forming a strong ensemble. In each new tree, previous errors are tried to be corrected. The final classification is made by the weighted sum of all trees [32].

Figure 4 shows the flow chart of the classification process.

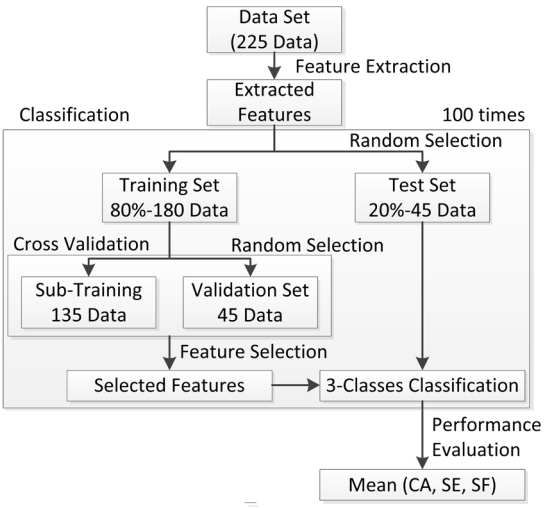

Figure 4. Classification Flow Diagram

The classification metrics were used to evaluate the performance of the classifiers.

$$CA = \frac{CCT}{TT} x100 \quad (9)$$

$$SE = \frac{TP}{TP+FN} x100 \quad (10)$$

Table 3. Selected Features

	MQ-										
	2	3	4	5	6	7	8	9	131	135	137
x_{mean}	F0	0.097	F16	F24	0.114	F40	F48	F56	F64	0.117	F80
x_{std}	F1	0.081	F17	0.123	F33	F41	F49	F57	F65	F73	F81
x_{sum}	F2	0.116	F18	F26	F34	F42	F50	F58	F66	F74	F82
x_{med}	0.123	F11	F19	F27	F35	F43	F51	F59	F67	F75	F83
x_{min}	F4	F12	F20	F28	F36	F44	F52	F60	F68	F76	F84
x_{max}	F5	0.073	F21	F29	F37	F45	F53	F61	F69	F77	F85
x_{Q1}	F6	0.060	F22	0.096	F38	F46	F54	F62	F70	F78	F86
x_{Q3}	F7	F15	F23	F31	F39	F47	F55	F63	F71	F79	F87
Total Effect (%)	0.123	0.427	-	0.219	0.114	-	-	-	-	0.117	-

$$SF = \frac{TN}{TN+FP} x100 \quad (11)$$

CA: Classification Accuracy, SE: Sensitivity, SF: Specifity, CCT: Correctly Classified Trials, TT: Total Trials, TP: True Positive, TN: True Negative, FP: False Positive, FN: False Negative.

For the sake of the reliability of the classification process, the classification mentioned above was performed 100 times with the random selection of different training-test sets. The arithmetic average of 100 classification results was accepted as classification success.

RESULTS AND DISCUSSION

The study recorded the odor of 225 yogurt samples on a computer. They belong to 5 different yogurt types. One-third of the total 225 samples were plain yogurt, one-third had little garlic, and the other was yogurt with lots of garlic. All these samples were sniffed for 30 seconds, and sensor data were taken into the computer. Here, a matrix of values of 225x11x301 has been obtained, including 225 samples, 11 gas sensors, and 301 sensor output values.

Eight different features (x_{mean}, x_{std}, x_{sum}, x_{med}, x_{min}, x_{max}, x_{Q1}, x_{Q3}) were extracted from each sensor. These features were obtained from 11 sensors, reaching 11×8=88 features. The number of features to be selected was determined by testing with the cross-validation method, and the ten features that provided the best performance were selected. The RFE method was configured to select the ten most effective features among these 88 features. Feature extraction is one of the most fundamental components of the success of a classification study. Here, the more accurately the features the classifier uses are extracted, the higher the performance at the end of the classification [33]. The selected features and the selection percentages of these features are given in Table 3.

As seen in Table 3, the effective sensors are the MQ-2, MQ-3, MQ-5, MQ-6, and MQ-135 gas sensors. The total effect of each sensor on the result is expressed in the table. According to these results, the most effective gas sensors in detecting garlic concentrations of garlic yogurts with the e-nose used in the study were MQ-3, MQ-5, MQ-2, MQ-137, and MQ-6, respectively.

The test data were classified with four different classification algorithms using these features. The performances of the classification algorithms with CA, SE, and SF metrics calculated according to the average confusion matrix obtained as a result of classifications made with 100 different training-test data are given in Table 4 [34]. The number k in the kNN algorithm was determined by the cross-validation method, and the optimum value was selected as 3. For the Random Forest algorithm, the n_estimators parameter was used as 100, which is the default value of the scikit-learn library.

Table 4. Classification Results According to Classifiers

Classification Algorithm	CA (%)	SE (%)	SF (%)
Extra Trees	89.14	89.80	94.57
kNN-3	86.22	86.89	93.10
Random Forest	84.30	84.39	92.21
Gradient Boosting	82.00	82.00	91.00

For the test data of the Extra Trees Classification algorithm, which gives the highest CA accuracy in classifications, the average confusion matrix of 100 classifications in percentages is given in Table 5.

Table 5. Confusion Matrix for Extra Trees Classification (%)

		Predicted		
	Accuracy: 89.14% plain yogurt	yogurt with a little garlic	yogurt with lots of garlic	
Real	**plain yogurt**	96.0	4.0	0.0
	yogurt with a little garlic	6.7	82.7	10.7
	yogurt with lots of garlic	2.0	9.3	88.7

The pseudo-code of the study, generated only for the Extra Trees algorithm, is presented in Table 6.

Table 6. The Pseudo-Code of the Study

```
Input: Sensor data from 11 sensors
Output: Classification performance metrics (CA, SE, SF)
1. Load Data:
  a. Read sensor data from multiple Excel files.
  b. Ensure all files have the same shape.
2. Preprocess Data:
  a. Detect missing values (zeros) in the data.
  b. Replace missing values with neighboring non-zero values.
3. Feature Extraction:
  a. For each sensor, calculate 8 statistical features:
    - Mean, standard deviation, sum, median, minimum, maximum,
Q1, Q3.
  b. Combine these features from all 11 sensors to form a feature set
of 88 features.
4. Feature Selection with RFE:
  a. Use Recursive Feature Elimination (RFE) with Random Forest
Classifier.
  b. Select the top 10 features based on importance scores.
5. Split Data:
  a. Divide the data into training (60%), validation (20%), and test
(20%) sets.
6. Train and Test the Model:
  a. For 100 iterations:
    i. Randomly shuffle and split the data.
    ii. Train Extra Trees Classifier on the training set.
    iii. Predict labels for the test set.
    iv. Record accuracy (CA), sensitivity (SE), and specificity (SF)
for each iteration.
7. Calculate Final Performance:
  a. Compute the average CA, SE, and SF across 100 iterations.
  b. Record the confusion matrix for the final model.
8. Return Results:
  a. Selected features from RFE.
  b. Average classification performance (CA, SE, SF).
```

Zeng et al. (2023) combined electronic nose technology with machine learning methods to determine the aroma types of plain yogurt [19]. In this study, garlic concentrations in yogurt were determined using an electronic nose. While both studies highlight the potential of electronic nose systems in food analytics, the current research focuses specifically on the quantitative analysis of garlic, an aromatic component.

Kaur and Barringer (2024) investigated the effect of yogurt on neutralizing the volatile sulfur compounds of raw garlic [23]. Another study by the same authors in 2023 analyzed how the volatile compounds of both raw and fried garlic were removed by yogurt and its components [24]. While these studies focused on the removal of garlic odor, the current study focuses on the determination and classification of the concentration of garlic in yogurt. Therefore, while previous studies evaluated the odor removal aspect of garlic, this study uses electronic nose technology to objectively measure the presence and amount of garlic.

Tamaki et al. (2008) analyzed the odor changes after garlic consumption with both electronic nose and gas chromatography [25]. However, this study focused on determining the concentration of garlic in different types of yogurt and offers a new application for the determination of food components.

The accuracy and performance of the MQ series gas sensors used in this study are based on the technical specifications of the manufacturer. Calibration and accuracy tests of the sensors are outside the scope of this study. However, the effectiveness of the sensors in detecting garlic concentration is indirectly supported by the high classification accuracy (89.14%) and sensitivity (89.80%) rates obtained with machine learning algorithms. In future studies, it is recommended to perform calibration studies using standard gases or reference samples in order to test the accuracy of the sensors in more detail. In addition, a more comprehensive evaluation of the sensor performance with additional experiments such as cross-sensitivity tests and repeatability analyses will increase the reliability of this technology in food analysis.

There are two limitations to the study. Among these, the first thing that stands out is the small number of samples. Since this is a research study, the number of samples has been kept small. Although there are different yogurts, it has been shown that the amount of garlic in garlic yogurt can be detected electronically. The number of samples will inevitably increase when the study needs to be integrated into any electronic system in the future. The second limitation is that the number of features is kept at eight. Classifiers may make this determination with higher accuracy by extracting various features.

CONCLUSION

In this study, an e-nose with eleven gas sensors was made. Fifteen different samples were obtained from five different types of yogurt, including plain, low garlic, and very garlic, and the odors of these samples were taken with the e-nose. Then, eight different features (x_{mean}, x_{std}, x_{sum}, x_{med}, x_{min}, x_{max}, x_{Q1}, x_{Q3}) were calculated for each sensor, and a total of 88 features were obtained. The most effective ten features were selected from these 88 features with the Recursive Feature Elimination (RFE) method. As a result of examining the selected features, it was determined that only the data of five gas sensors were significant in the study, and among these sensors, the MQ-3 gas sensor had the highest contribution. The significant sensors were identified as MQ-2, MQ-3, MQ-5, MQ-6 and MQ-135. These feature values were classified for 100 different training-test data selections with four different classification algorithms. The test data were classified using the most successful Extra Trees classification algorithm, which had 89.14% CA, 89.80% SE, and 94.57% SF performance, according to the average of 100 different classification results. As a result of the study, yogurts with different garlic densities were detected with high accuracy based on their odor profiles using the proposed method.

Acknowledgment

This research is not related to either human or animal use.

References

1. N. Altawell, Introduction to Machine Olfaction Devices. Elsevier, 2021.
2. J. W. Gardner and P. N. Bartlett, "A brief history of electronic

noses," Sens. Actuators B Chem., vol. 18, no. 1, pp. 210–211, Mar. 1994, doi: 10.1016/0925-4005(94)87085-3.
3. N. Husni, A. Handayani, S. Nurmaini, and I. Yani, Odor classification using Support Vector Machine. 2017, p. 76. doi: 10.1109/ICECOS.2017.8167170.
4. M. Cao and X. Ling, "Quantitative Comparison of Tree Ensemble Learning Methods for Perfume Identification Using a Portable Electronic Nose," Appl. Sci., vol. 12, no. 19, Art. no. 19, Jan. 2022, doi: 10.3390/app12199716.
5. A. Khorramifar et al., "Environmental Engineering Applications of Electronic Nose Systems Based on MOX Gas Sensors," Sensors, vol. 23, no. 12, Art. no. 12, Jan. 2023, doi: 10.3390/s23125716.
6. A. D'Amico et al., "An investigation on electronic nose diagnosis of lung cancer," Lung Cancer Amst. Neth., vol. 68, no. 2, pp. 170–176, May 2010, doi: 10.1016/j.lungcan.2009.11.003.
7. B. Ibrahim et al., "Non-invasive phenotyping using exhaled volatile organic compounds in asthma," Thorax, vol. 66, no. 9, pp. 804–809, Sep. 2011, doi: 10.1136/thx.2010.156695.
8. B. H. Tozlu, C. Şimşek, O. Aydemir, and Y. Karavelioglu, "A High performance electronic nose system for the recognition of myocardial infarction and coronary artery diseases," Biomed. Signal Process. Control, vol. 64, p. 102247, Feb. 2021, doi: 10.1016/j.bspc.2020.102247.
9. A. Bermak and M. Hassan, "Noninvasive Diabetes Monitoring with Electronic Nose," presented at the Qatar Foundation Annual Research Conference Proceedings Volume 2016 Issue 1, Hamad bin Khalifa University Press (HBKU Press), Mar. 2016, p. HBPP2776. doi: 10.5339/qfarc.2016.HBPP2776.
10. O. Zaim, T. Saidi, N. El Bari, and B. Bouchikhi, "Assessment Of 'Breath Print' In Patients With Chronic Kidney Disease During Dialysis By Non-Invasive Breath Screening Of Exhaled Volatile Compounds Using An Electronic Nose," in 2019 IEEE International Symposium on Olfaction and Electronic Nose (ISOEN), Fukuoka, Japan: IEEE, May 2019, pp. 1–4. doi: 10.1109/ISOEN.2019.8823338.
11. A. de la Rica-Martinez et al., "Low-Cost Electronic Nose for the Determination of Urinary Infections," Sensors, vol. 24, no. 1, Art. no. 1, Jan. 2024, doi: 10.3390/s24010157.
12. M. Xu, J. Wang, and L. Zhu, "Tea quality evaluation by applying E-nose combined with chemometrics methods," J. Food Sci. Technol., vol. 58, no. 4, pp. 1549–1561, Apr. 2021, doi: 10.1007/s13197-020-04667-0.
13. E. Osmólska, M. Stoma, and A. Starek-Wójcicka, "Juice Quality Evaluation with Multisensor Systems—A Review," Sensors, vol. 23, no. 10, Art. no. 10, Jan. 2023, doi: 10.3390/s23104824.
14. S. Güney and A. Atasoy, "Study of fish species discrimination via electronic nose," Comput. Electron. Agric., vol. 119, pp. 83–91, Nov. 2015, doi: 10.1016/j.compag.2015.10.005.
15. K. Fujioka, "Comparison of Cheese Aroma Intensity Measured Using an Electronic Nose (E-Nose) Non-Destructively with the Aroma Intensity Scores of a Sensory Evaluation: A Pilot Study," Sensors, vol. 21, no. 24, Art. no. 24, Jan. 2021, doi: 10.3390/s21248368.
16. A. N. Damdam, L. O. Ozay, C. K. Ozcan, A. Alzahrani, R. Helabi, and K. N. Salama, "IoT-Enabled Electronic Nose System for Beef Quality Monitoring and Spoilage Detection," Foods Basel Switz., vol. 12, no. 11, p. 2227, May 2023, doi: 10.3390/foods12112227.
17. A. Poghossian, H. Geissler, and M. J. Schöning, "Rapid methods and sensors for milk quality monitoring and spoilage detection," Biosens. Bioelectron., vol. 140, p. 111272, Sep. 2019, doi: 10.1016/j.bios.2019.04.040.
18. C. Gonzalez Viejo, E. Tongson, and S. Fuentes, "Integrating a Low-Cost Electronic Nose and Machine Learning Modelling to Assess Coffee Aroma Profile and Intensity," Sensors, vol. 21, no. 6, Art. no. 6, Jan. 2021, doi: 10.3390/s21062016.
19. H. Zeng, H. Han, Y. Huang, and B. Wang, "Rapid prediction of the aroma type of plain yogurts via electronic nose combined with machine learning approaches," Food Biosci., vol. 56, p. 103269, Dec. 2023, doi: 10.1016/j.fbio.2023.103269.
20. S. Grassi, S. Benedetti, L. Magnani, A. Pianezzola, and S. Buratti, "Seafood freshness: e-nose data for classification purposes," Food Control, vol. 138, p. 108994, Aug. 2022, doi: 10.1016/j.foodcont.2022.108994.
21. Y. Xiong et al., "Non-Destructive Detection of Chicken Freshness Based on Electronic Nose Technology and Transfer Learning," Agriculture, vol. 13, no. 2, Art. no. 2, Feb. 2023, doi: 10.3390/agriculture13020496.
22. L. Qiu, M. Zhang, A. S. Mujumdar, and L. Chang, "Effect of edible rose (Rosa rugosa cv. Plena) flower extract addition on the physicochemical, rheological, functional and sensory properties of set-type yogurt," Food Biosci., vol. 43, p. 101249, Oct. 2021, doi: 10.1016/j.fbio.2021.101249.
23. M. Kaur and S. Barringer, "Effect of Yogurt on the Deodorization of Raw Garlic (Allium sativum L.) Sulfur Volatiles in Breath and the Roles of Its Components," Dairy, vol. 5, no. 2, Art. no. 2, Jun. 2024, doi: 10.3390/dairy5020026.
24. M. Kaur and S. Barringer, "Effect of Yogurt and Its Components on the Deodorization of Raw and Fried Garlic Volatiles," Mol. Basel Switz., vol. 28, no. 15, p. 5714, Jul. 2023, doi: 10.3390/molecules28155714.
25. K. Tamaki, S. Sonoki, T. Tamaki, and K. Ehara, "Measurement of odor after in vitro or in vivo ingestion of raw or heated garlic, using electronic nose, gas chromatography, and sensory analysis," Int. J. Food Sci. Technol., vol. 43, no. 1, pp. 130–139, 2008, doi: 10.1111/j.1365-2621.2006.01403.x.
26. F. Suarez, J. Springfield, J. Furne, and M. Levitt, "Differentiation of mouth versus gut as site of origin of odoriferous breath gases after garlic ingestion," Am. J. Physiol., vol. 276, no. 2, pp. G425-430, Feb. 1999, doi: 10.1152/ajpgi.1999.276.2.G425.
27. A. Makarichian, R. Amiri Chayjan, E. Ahmadi, and S. S. Mohtasebi, "Assessment the influence of different drying methods and pre-storage periods on garlic (Allium Sativum L.) aroma using electronic nose," Food Bioprod. Process., vol. 127, pp. 198–211, May 2021, doi: 10.1016/j.fbp.2021.02.016.
28. J. Liu, Y. Liu, X. Li, J. Zhu, X. Wang, and L. Ma, "Drying characteristics, quality changes, parameters optimization and flavor analysis for microwave vacuum drying of garlic (Allium sativum L.) slices," LWT, vol. 173, p. 114372, Jan. 2023, doi: 10.1016/j.lwt.2022.114372.
29. E. Ozturk Kiyak, B. Ghasemkhani, and D. Birant, "High-Level K-Nearest Neighbors (HLKNN): A Supervised Machine Learning Model for Classification Analysis," Electronics, vol. 12, no. 18, Art. no. 18, Jan. 2023, doi: 10.3390/electronics12183828.
30. T. Kavzoglu and F. Bilucan, "Effects of auxiliary and ancillary data on LULC classification in a heterogeneous environment using optimized random forest algorithm," Earth Sci. Inform., vol. 16, no. 1, pp. 415–435, Mar. 2023, doi: 10.1007/s12145-022-00874-9.
31. A. K. V, A. A, B. Jose, K. Anilkumar, and O. T. Lee, "Phishing Detection using Extra Trees Classifier," in 2021 5th International Conference on Information Systems and

Computer Networks (ISCON), Oct. 2021, pp. 1–6. doi: 10.1109/ISCON52037.2021.9702372.
32. Y. Chen, Z. Jia, D. Mercola, and X. Xie, "A Gradient Boosting Algorithm for Survival Analysis via Direct Optimization of Concordance Index," Comput. Math. Methods Med., vol. 2013, no. 1, p. 873595, 2013, doi: 10.1155/2013/873595.
33. Ö. Aydemir, "Common spatial pattern-based feature extraction from the best time segment of BCI data," Turk. J. Electr. Eng. Comput. Sci., vol. 24, no. 5, pp. 3976–3986, Jan. 2016, doi: 10.3906/elk-1502-162.
34. S. A. Hicks et al., "On evaluation metrics for medical applications of artificial intelligence," Sci. Rep., vol. 12, p. 5979, Apr. 2022, doi: 10.1038/s41598-022-09954-8.

HITTITE JOURNAL OF SCIENCE AND ENGINEERING

e-ISSN: 2148-4171
Volume: 12 • Number: 1
March 2025

Effect of Double-Pulse Strategy on the Expulsion Formation and Peak Loads During Resistance Spot Welding of Dissimilar Thickness Ultra - High Strength MS1500 and Mild DD11 Steels

Mehmet Okan Görtan
Hacettepe University, Department of Mechanical Engineering, Ankara, Türkiye.

Corresponding Author
Mehmet Okan Görtan
E-mail: okangortan@hacettepe.edu.tr Phone: +90 312 297 62 08 Fax: +90 312 297 62 06
RORID: https://ror.org/04kwvgz42

Article Information
Article Type: Research Article
Doi: https://doi.org/10.17350/HJSE19030000351
Received: 21.01.2025
Accepted: 21.03.2025
Published: 25.03.2025

Cite As
Görtan MO. Effect of Double-Pulse Strategy on the Expulsion Formation and Peak Loads During Resistance Spot Welding of Dissimilar Thickness Ultra - High Strength MS1500 and Mild DD11 Steels. Hittite J Sci Eng. 2025;12(1):51-58.

Peer Review: Evaluated by independent reviewers working in at least two different institutions appointed by the field editor.
Ethical Statement: Not available.
Plagiarism Checks: Yes - iThenticate
Conflict of Interest: Authors declare no conflict of interest.

CRediT AUTHOR STATEMENT
Mehmet Okan Görtan: Funding acquisition, Conceptualization, Methodology, Investigation, Data curation, Visualization, Validation, Writing- original draft.

Effect of Double-Pulse Strategy on the Expulsion Formation and Peak Loads During Resistance Spot Welding of Dissimilar Thickness Ultra - High Strength MS1500 and Mild DD11 Steels

Mehmet Okan Görtan

Hacettepe University, Department of Mechanical Engineering, Ankara, Türkiye.

Abstract

Resistance spot welding (RSW) is widely utilized in the automotive industry due to its high efficiency, flexibility, and compatibility with automation. These advantages make it a preferred method for joining advanced high-strength steels, enabling lightweight designs without compromising structural integrity. This study explores the mechanical properties of resistance spot-welded joints between ultra-high-strength MS1500 steel and hot-rolled DD11 steel, with a focus on single-pulse and double-pulse welding strategies. The effects of varying current levels were evaluated in terms of tensile-shear strength, failure energy, nugget diameter, hardness distribution, and microstructural transformations. In single-pulse welding, expulsion was observed at a current of 8.6 kA, limiting joint performance. Conversely, the double-pulse welding strategy provided enhanced control, yielding superior results. Optimal performance was achieved at a second welding current of 8.4 kA, with a tensile-shear strength increase of 11.6% and a fracture energy enhancement of 32.2% compared to single-pulse welding. Beyond 8.6 kA, expulsion caused inconsistencies in mechanical properties, highlighting the importance of current optimization in welding strategies. The findings demonstrate the effectiveness of the double-pulse welding strategy in improving the strength and quality of resistance spot-welded joints.

Keywords: Resistance spot welding, Ultra-high strength steel, Double-pulse welding, Expulsion, Mechanical strength

INTRODUCTION

One of the most significant trends that has marked the automotive industry over the last 20 years is weight reduction. The most commonly employed strategy to achieve this is replacing the materials used with higher-strength alternatives. This approach enables the reduction of vehicle weight by carrying the same loads with smaller cross-sections without compromising passenger safety [1]. Due to its flexibility in application, high efficiency, and suitability for automation, resistance spot welding (RSW) has become the preferred method for joining high-strength sheets, particularly in the automotive industry [2]. Therefore, improving the mechanical strength of RSW joints holds great importance.

An electric current is passed through sheet materials, typically held together by pressurized electrodes that are actively cooled during RSW. The heat energy generated by the flow of electricity causes a rapid temperature increase in a relatively small area between the sheets, allowing the molten metals to bond within a short time [3]. In the RSW process, the rapid cooling of the molten metal in the nugget region after welding enables the formation of martensitic microstructures with high mechanical strength in steel sheets [4]. Therefore, RSW is currently widely used, especially in the automotive industry, for joining advanced high-strength steel sheets [5-7].

The most common traditional method to improve the mechanical properties of RSW joints is to optimize the welding current and duration. The main determining factor here is to maximize the nugget diameter in the joint area without causing expulsion [8]. In recent years, a technology frequently referred to as double-pulse welding has been employed. In this method, the welding current is interrupted in the first step before expulsion occurs, followed by the application of a higher or lower current in a second welding step [9-13]. This approach allows for increasing the nugget diameter without expulsion, which negatively affects joint stability, thereby enhancing mechanical strength.

In addition, the use of metals with different strength and metallurgical properties together is a common practice, especially in the automotive industry. RSW can also be used to join these materials. In the current studies, it is shown that RSW can also be used to join advanced high-strength steel sheets of different types and thicknesses based on specific application needs [14-19].

In the current study, the RSW properties of ultra-high-strength MS1500 steel and hot-rolled DD11 (1.0332) steel of varying thicknesses were investigated. Those kind of joints are required recently especially in the bumper beam sections of passenger vehicles. In preliminary studies, expulsion limit of the joint in single-pulse strategy was determined. Afterwards, the effects of the double-pulse welding strategy using different current values were investigated. Mechanical strength of the joints was determined using tensile-shear tests. After the mechanical testing of the joints, the types of fractures that occurred were examined using optical microscopy. The strength and the various fracture modes observed were discussed along with the microstructural properties.

MATERIAL AND METHODS

In the experimental studies, martensitic micro-structured ultra-high-strength MS1500 steel with a thickness of 1.2 mm and hot-rolled DD11 drawing steel with a thickness of 2.0 mm were used. The chemical compositions of these materials are shown in Table 1. The MS1500 steel contains 0.271% carbon and 0.770% manganese. On the other hand, the DD11 steel has very low carbon content but relatively high manganese content of approximately 0.219%. Accordingly, a martensitic transformation in the microstructure can be expected in both materials after rapid cooling from the austenitic region.

Table 1. Alloy composition of the investigated materials (weight %).

Material	C	Si	Mn	Al	Ti	Cr	B	Cu	Fe
DD11	0.057	-	0.219	0.045	-	-	-	-	balance
MS1500	0.271	0.207	0.770	0.268	0.036	0.023	0.010	0.116	balance

The mechanical properties of the material were determined using specimens with a nominal width of 12.5 mm and a nominal gauge length of 50 mm in accordance with the ISO 6892-1:2009 standard. For this purpose, five tests were conducted, and the average results of these tests are presented in Table 2.

Table 2. Mechanical properties of the investigated materials.

Material	Yield Strength [MPa]	Tensile Strength [MPa]	Alongation at Fracture [%]
DD11	272.3	372.3	34.5
MS1500	1459.2	1643.8	5.5

The specimens to be used in RSW trials were mechanically cut to dimensions of 105 x 45 mm in accordance with the ISO 14273:2016 standard. These specimens were positioned and joined as shown in Figure 1, in compliance with the standard. DD11 samples are put on top and MS1500 samples are at the bottom during welding. That way, welding of dissimilar materials is realized. After the welding process, support plates were welded to prevent additional deformation in the nugget region during the tensile-shear test. The arrows in the figure indicate the pulling directions during the tensile-shear test.

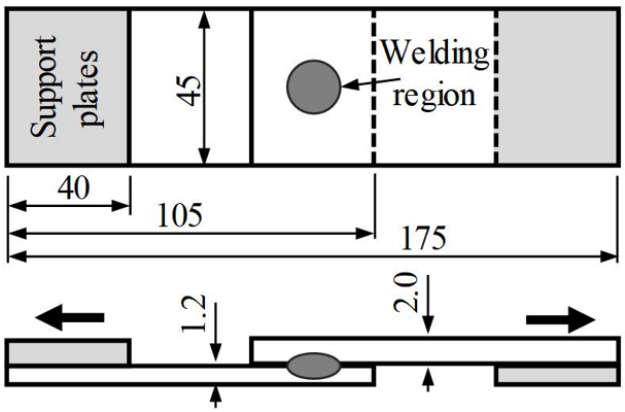

Figure 1: Geometry of the resistance spot welded specimens (All dimensions in mm).

All welding operations were performed using a 70 kVA capacity, water-cooled, pneumatically operated pedestal-type RSW machine with numerically controlled welding current, duration, and electrode pressure. This machine operates at 50 Hz frequency, identical to the electrical grid, meaning one welding cycle lasts 20 milliseconds. The primary welding parameters in this study were determined in accordance with the recommendations of the American Welding Society.

First, since sheets of different thicknesses were used, the equivalent sheet thickness was calculated using the formula provided in Eq. 1:

$$t_{eq} = t_{thin} + \left[0.2 * \left(t_{thick} - t_{thin}\right)\right] \quad (1)$$

Here t_{eq} represents the equivalent thickness, t_{thin} is the thickness of the thinner sheet, and t_{thick} is the thickness of the thicker sheet.

Based on the calculated equivalent thickness value of 1.36 mm, electrodes compliant with ISO 5821:2009 standards, type G0 with an 8 mm contact diameter and a height of 20 mm, were used in the welding process. These electrodes were manufactured from type A 2/3 copper alloyed with chromium and zirconium, as specified by ISO 5182:1991.

The electrode force applied in the study was set to 3.5 kN. The welding duration for each operation was set to 12 cycles, equivalent to 0.24 seconds. The hold time after welding was chosen as 20 cycles, or 0.40 seconds.

During single-pulse welding, expulsion was observed at current values above 8.6 kA. Therefore, 8.6 kA was chosen as the starting value for this study. In double-pulse welding, after applying an 8.6 kA current for 12 cycles, a 2-cycle (0.04-second) pause was introduced. Subsequently, in the second stage, currents ranging between 7.2 and 9.6 kA, increasing incrementally by 0.2 kA, were applied for another 12 cycles.

In both welding strategies, the squeeze time before welding was set to 50 cycles. Similarly, the electrode release time after the completion of each welding operation was also set to 50 cycles. The applied welding strategy is schematically illustrated in Fig. 2.

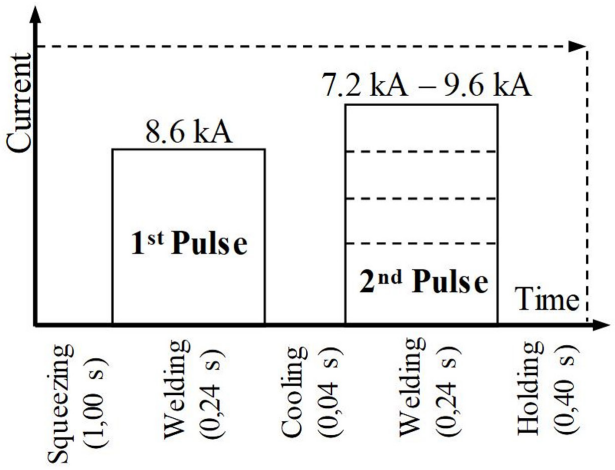

Figure 2: Schematic view of the pulse scheme.

For each welding current value planned for investigation in the study, 10 specimens were produced. To ensure the statistical significance of the tensile-shear test results, 9 of these specimens were used for testing. All tests were conducted in accordance with the ISO 14273:2016 standard using a servo-mechanical UTEST universal tensile testing machine with a 50 kN capacity at a constant speed of 10 mm/min.

The tensile-shear strength and fracture energy of the joints were determined from the force-displacement curves of the applied tests. These results are shown as an example in Fig. 3. The highest value on the force-displacement curve is considered the tensile-shear strength of the joint.

The fracture energy is defined as the area under the force-displacement curve up to the maximum load value and is calculated using Eq. 2:

$$FE = \sum_{n=1}^{n_{max}} F(n) * \left[x(n) - x(n-1)\right] \quad (2)$$

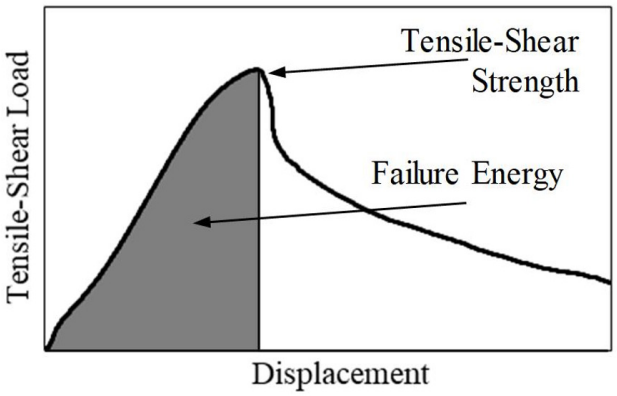

Figure 3: Schematic representation of load-displacement curve results.

Here F is the load in Newtons, x is the displacement in millimeters, n is the total number of data points, and n_{max} is the number of data points corresponding to the maximum force measured.

One of the welded specimens was used for geometry and microstructure analyses. For this purpose, the specimens were abrasively cut at their central regions and mounted in cold bakelite. Subsequently, they were ground with papers ranging from P400 to P2500 grit and polished using a 1µm diamond suspension. To examine the microstructure and perform geometric measurements, the specimens were etched with 4% Nital solution for approximately 10 seconds. Optical measurements were carried out using an Optika IM-3MET microscope. In this study, specific measurements of the nugget diameter and indentation geometry were conducted. The indentation value was determined using Eq. 3:

$$indentation = t_{thin} + t_{thick} - weld\ \ height \quad (3)$$

Here t_{thin} is the thickness of the thinner sheet, t_{thick} is the thickness of the thicker sheet, and *weld height* is the measured joint section thickness. These dimensions are schematically illustrated in Fig. 4.

Microstructure analyses were performed using a Hitachi SU5000 scanning electron microscope. The hardness measurements of the specimens were conducted in accordance with the ISO 6507-1:2018 standard using a Future Tech FM-700e device with a 100 g load and a dwell time of 15 seconds. All measurements were taken along a section starting in the base metal of DD11 material, going through the nugget, and ending in the base metal of MS1500 steel.

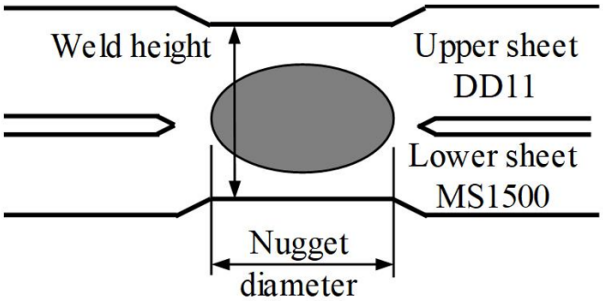

Figure 4: Schematic representation of joint section.

RESULTS AND DISCUSSION

The tensile-shear test results of the specimens produced using different current values and welding strategies are shown in Fig. 5. In this figure, the average results of the 9 tests performed are presented along with the standard deviation of the results. At the current value of 8.6 kA, which is the limit for the single-pulse welding application, the tensile-shear force and fracture energy values were determined as 18.32 kN and 33.27 J, respectively. Additionally, in this case, the standard deviation values for the tensile-shear force and fracture energy were calculated as 0.84 kN and 1.90 J, respectively.

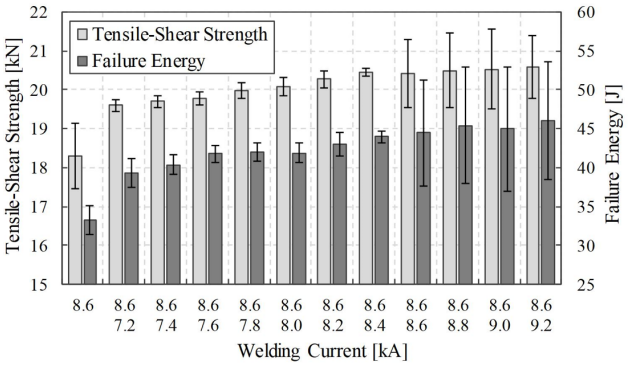

Figure 5: Tensile-shear test results of trials with different current values.

When the double-pulse welding strategy was applied, a consistent increase in strength values and a regular decrease in standard deviation values were noted until the second welding current reached 8.4 kA. However, when the second welding current increased to 8.6 kA, the increase in mechanical strength values ceased, and a significant rise in standard deviation values was observed. As a result, for the condition where the first and second pulse welding currents were 8.6 kA and 8.4 kA, respectively, which yielded the highest mechanical strength, the tensile-shear strength and fracture energy were determined as 20.45 kN and 43.98 J, respectively. In this condition, compared to the single-pulse welding application, an increase of 11.6% in tensile-shear strength and 32.2% in fracture energy was observed. Furthermore, in the double-pulse welding application with the highest strength, the standard deviation values were determined as 0.09 kN for tensile-shear strength and 0.79 J for fracture energy. However, no improvement in mechanical strength was observed when the second current value was

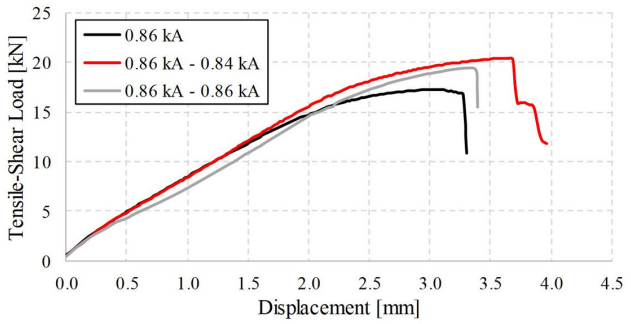

Figure 6: Example of tensile-shear test results.

8.6 kA or higher. On the contrary, the standard deviation values of the measurements increased significantly.

The differences can be better understood by analyzing the tensile-shear test results in detail. Fig. 6 shows sample test results for three different cases. When single-pulse welding is applied, relatively low strength and low deformation before fracture are observed. Accordingly, the results shown in Fig. 5 are obtained. For the case where the highest strength is achieved using the double-pulse welding strategy, the deformation at the moment of fracture is greater compared to other cases. Additionally, it is observed that the test specimens do not break suddenly; after reaching the maximum strength, the sheets separate from each other only after undergoing additional deformation. Consequently, the failure energy values are also higher compared to other cases. However, when the current value in the double-pulse welding strategy exceeds 8.6 kA, the maximum strength values decrease, and the specimens fracture suddenly. Lastly, a common feature of all tensile-shear tests is that the force increases rapidly at the beginning but slows down as it approaches fracture. This has been interpreted as an indication that the lower-strength DD11 steel undergoes additional deformation before fracture.

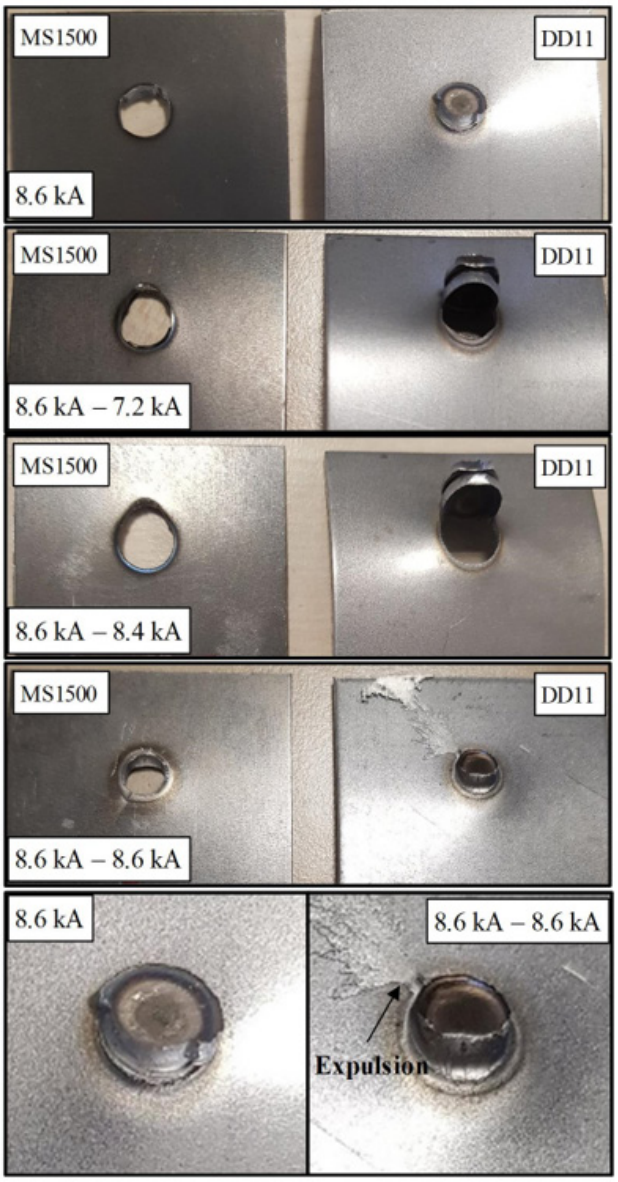

Figure 6: Fracture pictures of the joints generated using different currents (Detail views of fracture is given in the bottom pictures).

This situation observed in the results can be explained by the fracture images of the weld region shown in Fig. 7, the nugget diameter distribution in Fig. 9, the changes in indentation depth shown in Fig. 10, and the force-displacement diagrams provided as an example in Figure 11. In Fig. 7, it is shown that when a single-pulse welding current of 8.6 kA is applied, the weld region fractures in the form of partial pull-out and partial interfacial failure, and no expulsion occurs during welding. When double-pulse welding is applied, even at the lowest second current value of 7.2 kA examined, the fracture occurs in the form of full pull-out failure. A similar observation is valid for the current value at which the highest strength is achieved. However, when the double-pulse welding current is increased to 8.6 kA, expulsion occurs in the weld region, and the fracture happens as partial pull-out and partial interfacial failure. In the RSW process, expulsion occurs randomly and cannot be controlled. Consequently, differences in mechanical strength values arise among repeated tests.

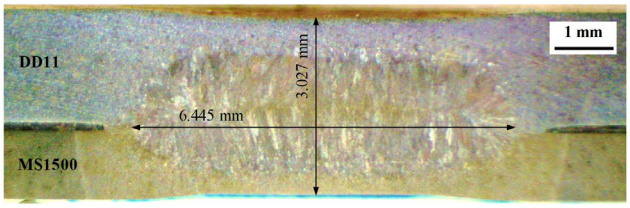

Figure 8: Cross-section view of the welded joint using double-pulse strategy with 8.6 kA and 8.4 kA currents.

The geometric properties of welds performed with different current levels were examined through their cross-sections. The cross-section image of the joint, created using the double-pulse strategy with the highest strength observed at 8.6 kA and 8.4 kA currents, is shown as an example in Fig. 8. The measured nugget diameter values of joints welded with different currents using single-pulse and double-pulse welding strategies are presented in Fig. 9. When these values are analyzed, it is observed that the nugget diameter increases even at the lowest current value when transitioning

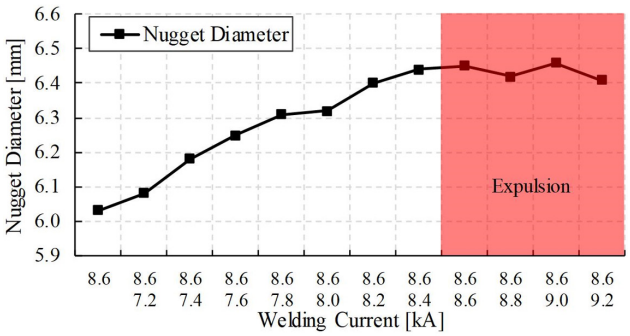

Figure 9: Nugget diameter distribution depending on the welding current.

from the single-pulse to the double-pulse welding strategy. Furthermore, this increase in diameter continues until the double-pulse welding current reaches 8.4 kA. However, when the current value is 8.6 kA or higher, the increase in nugget diameter ceases. This situation is directly associated with expulsion. In the case of expulsion, the liquid metal in the weld area is expelled outside the welding zone. As the molten metal exits the welding zone, the nugget diameter stops increasing. The occurrence of expulsion at currents of 8.6 kA and above is also illustrated in Fig. 7.

The changes in indentation values depending on the welding current and welding strategy are shown in Fig. 10. In the geometry of resistance spot-welded joints, it is desirable to have low indentation values. However, due to the increase in the volume of molten metal during the process, the penetration of the electrodes into the metal increases as a result of the applied force. Especially in the automotive industry, it is expected that the indentation value remains below 10% for aesthetic components. It has been determined that the indentation ratio increases when transitioning from the single-pulse to the double-pulse welding strategy. Additionally, the indentation values show a consistent increase up to a welding current of 8.4 kA. However, at 8.6 kA, a significant upward jump in the indentation value is observed. This is caused by the expulsion and resulting ejection of the molten metal out of the nugget section. As a result, welding electrodes can penetrate the sheet metals more.

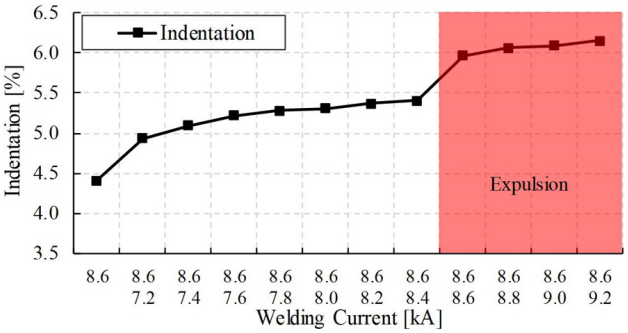

Figure 10: Indentation distribution depending on the welding current.

The hardness distribution along the weld was examined for the specimens produced with the double-pulse welding strategy at the current values yielding the highest strength. The measurement results are shown in Fig. 11. Hardness measurements were conducted at intervals of 0.10 mm. Measurements were taken along the line shown in Fig. 11 starting from the base metal of the DD11 steel, going through the nugget, and ending in the base metal of the MS1500 steel. The most notable observation in the hardness values is a significant increase in hardness in the nugget region of both materials. The initial hardness levels of MS1500 and DD11 steels, which were 365 HV and 135 HV, respectively, increased to about 400 HV within the nugget. Higher hardness in the nugget region of RSW joints compared to the base metal is already reported in former studies about martensitic steels [3, 20]. It is caused by the very high cooling rates in the nugget region of the joint caused by the contact with the cooled copper electrode. As a result, cooling rate may exceed 2000 K/s [3]. Such cooling rates may not be reached in conventional thermos-mechanical processes used in the manufacturing of martensitic steels.

Furthermore, the average hardness in the nugget region of DD11 steel was calculated as 394.9 HV. On the other hand, average hardness in the nugget of MS1500 steel was with 403.2 HV slightly higher. The difference is caused by the higher alloying composition of the MS1500 steel.
Additionally, an increase in hardness was observed in the heat-affected zone (HAZ) of the MS1500 material. No softening was detected in this region. It is caused by the grain refinement of the already existing martensitic structure in the base metal. Conventional martensitic steels are annealed after manufacturing to reduce the brittleness. Such an annealing process also causes a certain amount of grain growth in the microstructure. However, thanks to the rapid cooling after applied RSW process, a significant grain refinement is expected in the heat-affected zone (HAZ) of the joint, which is called as HAZ-hardening in the relevant literature [3].

In contrast to the MS1500 steel, within the DD11 material, the hardness in the HAZ decreased from 400 HV in the nugget to the base metal level of 135 HV over a distance of approximately 1 mm. Due to the low alloying composition of the DD11 steel, martensite formation should be suppressed in that material.

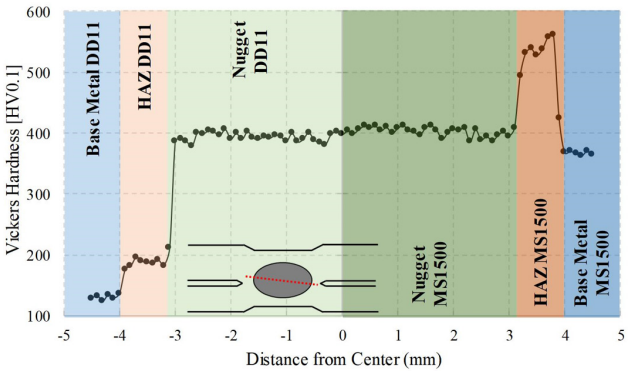

Figure 11: Hardness distribution in welding section.

The hardness behavior of the weld region can be explained through the microstructure analyses shown in Fig. 12. The DD11 steel used in the study has a ferritic-pearlitic microstructure, as shown in Figure 12(a). This ferritic-pearlitic microstructure transformed into a martensitic microstructure due to rapid cooling in the heat-affected zone (HAZ), as shown in Figure 12(b). However, ferrite islands are still visible within this structure. Consequently, the gradual hardness increase observed in Fig. 11 was noted.

As shown in Fig. 12(c), the microstructure of both materials in the nugget is identical. This region contains a martensitic structure, oriented toward the electrodes, which typically forms due to the very rapid cooling seen in resistance spot-welded joints. Fig. 12(d) shows the initial microstructure of the MS1500 material, which consists of a lath martensite structure with well-defined pocket boundaries. Due to the rapid cooling from the austenitic region in the HAZ, this microstructure transformed into fine-grained martensite, as illustrated in Figure 12(e). Accordingly, the hardness increase in the HAZ, shown in Fig 11, was observed.

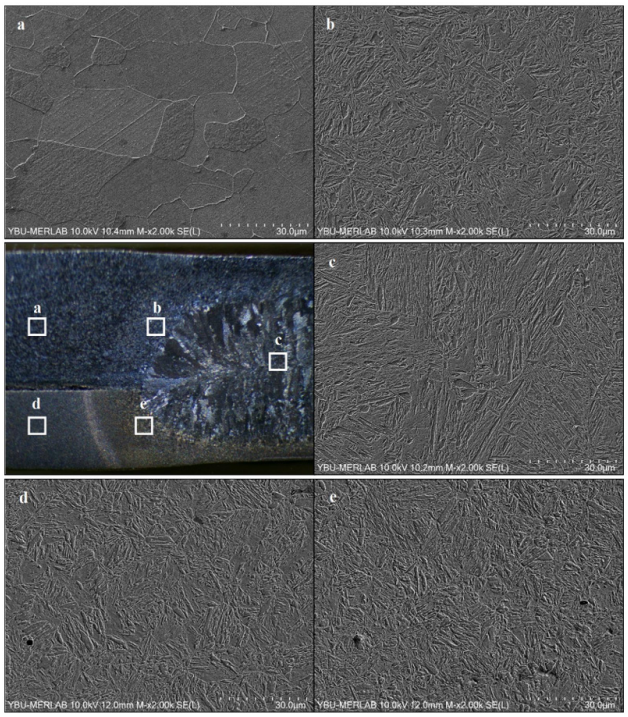

Figure 11: Scanning electron microscopy images of (a) base metal of DD11, (b) heat-affected zone of DD11, (c) nugget section of the joint, (d) base metal of MS1500, and (e) heat-affected zone of MS1500.

CONCLUSION

This study investigated the mechanical and microstructural properties of resistance spot-welded joints produced using single-pulse and double-pulse welding strategies for ultra-high-strength MS1500 steel and hot-rolled DD11 steel. Following conclusions are drawn from the studies:

- It was observed that in the single-pulse welding strategy, expulsion occurred at a welding current of 8.6 kA and above, limiting the mechanical performance of the joints.
- The double-pulse welding strategy could significantly improve the joint strength and failure energy.
- The optimal mechanical properties were achieved with a second welding current of 8.4 kA during the double pulse welding.
- The double-pulse welding strategy with optimum parameters resulted in a tensile-shear strength increase of 11.6% and a fracture energy improvement of 32.2% compared to the single-pulse strategy.
- During double pulse welding, when the second welding current exceeded 8.6 kA, expulsion started to occur and affected joint strength and consistency negatively.
- The double-pulse welding strategy with optimum parameters resulted in a nugget diameter of 6.445 mm which corresponds to an increase of 6.8% compared to single-pulse welding strategy.
- There was a slight increase in the indentation rate when using the double-pulse welding strategy. This rate increased from 4.41% at the single-pulse welding to 5.41% at the optimum double-pulse welding strategy.
- Microstructural analyses on DD11 steel indicated that the transformation of the ferritic-pearlitic structure in the heat-affected zone (HAZ) to martensitic microstructures contributed to the hardness increase.

The findings demonstrate the potential of the double-pulse welding strategy in enhancing the performance of resistance spot-welded joints, especially for applications requiring high strength and minimal deformation. Future studies could explore further optimization of current levels and welding durations to refine the double-pulse strategy for broader industrial applications.

Acknowledgement

The authors wish to thank the Turkish Research Council (TÜBİTAK) for financially supporting the project 5190043.

References

1. Jeswiet J, Geiger M, Engel U, Kleiner M, Schikorra M, Duflou J, Neugebauer R, Bariani P. Bruschi S. Metal forming progress since 2000. CIRP J. Manuf. Sci. Technol. 2008, 11: 2-17. https://doi.org/10.1016/j.cirpj.2008.06.005
2. Kimchi M, Philips DH. Resistance Spot Welding – Fundamentals and Applications for the Automotive Industry. 2nd edition. Switzerland, Springer Nature; 2023.
3. Pouranvari M, Marashi SPH. Critical review of automotive steels spot welding: process, structure and properties, Sci. Technol. Weld. Join. 2013; 18(5):361-403. https://doi.org/10.1179/1362171813Y.0000000120
4. Zhang H, Senkara J. Resistance Welding – Fundamentals and Applications. 2nd edition. Boca Raton: CRC Press; 2011.
5. Chabok A, van der Aa E, De Hosson JTM, Pei YT. Mechanical behavior and failure mechanism of resistance spot welded DP1000 dual phase steel. Mater. Des. 2017; 124:171-182. http://dx.doi.org/10.1016/j.matdes.2017.03.070
6. Noh W, Kim W, Yang X, Kang M, Lee M-G, Chung K. Simple and effective failure analysis of dissimilar resistance spot welded advanced high strength steel sheets. Int. J. Mech. Sci. 2017; 121:76-89. http://dx.doi.org/10.1016/j.ijmecsci.2016.12.006
7. Sivaraj P, Seeman M, Kanagarajan D, Seetharaman R. Influence of welding parameter on mechanical properties and microstructural features of resistance spot welded dual phase steel sheets joint. Mater. Today: Proc. 2020; 22(23):558-562. https://doi.org/10.1016/j.matpr.2019.08.201
8. Jaber HL, Pouranvari M, Salim RK, Hashim FA, Marashi SPH. Peak load and energy absorption of DP600 advanced steel resistance spot welds. Ironmak Steelmak. 2017; 44(9):699-706. https://doi.org/10.1080/03019233.2016.1229880
9. Chabok A, van der Aa E, Basu I, De Hosson JTM, Pei Y. Effect of pulse scheme on the microstructural evolution, residual stress state and mechanical performance of resistance spot welded DP1000-GI steel. Sci. Technol. Weld. Join. 2018; 23(8):649-658. https://doi.org/10.1080/13621718.2018.1452875
10. Pouranvari M, Aghajani H, Ghasemi A. Enhanced mechanical properties of martensitic stainless steels resistance spot welds enabled by in situ rapid tempering. Sci. Technol. Weld. Join. 2020; 25(2):119-126. https://doi.org/10.1080/13621718.2019.1641962
11. Kim JW, Murugan, SP, Yoo, JH, Ashiri R, Park YD. Enhancing nugget size and weldable current range of ultra-high-strength steel using multi-pulse resistance spot welding. Sci. Technol. Weld. Join. 2019; 25(3):235-242. https://doi.org/10.1080/13621718.2019.1680483

12. Soomro IA, Pedapati SR, Awang M. Optimization of postweld tempering pulse parameters for maximum load bearing and failure energy absorption in dual phase (DP590) steel resistance spot welds. Mater. Sci. Eng. A. 2021; 803:140713. https://doi.org/10.1016/j.msea.2020.140713
13. Liu XD, Xu YB, Misra RDK, Peng F, Wang Y, Du YB. Mechanical properties in double pulse resistance spot welding of Q&P 980 steel. J. Mater. Process. Technol. 2019; 263: 186-197. https://doi.org/10.1016/j.jmatprotec.2018.08.018
14. Mousavi Anijdan SH, Sabzi M, Ghobeiti-Hasab M, Roshan-Ghiyas A. Optimization of spot welding process parameters in dissimilar joint of dual phase steel DP600 and AISI 304 stainless steel to achieve the highest level of shear-tensile strength. Mater. Sci. Eng. A. 2018; 726:120-125. https://doi.org/10.1016/j.msea.2018.04.072
15. Yuan X, Li C, Chen J, Li X, Liang X, Pan X. Resistance spot welding of dissimilar DP600 and DC54D steels. J. Mater. Process. Technol. 2017; 239:31-41. http://dx.doi.org/10.1016/j.jmatprotec.2016.08.012
16. Zhang H, Qiu X, Xing F, Bai J, Chen J. Failure analysis of dissimilar thickness resistance spot welded joints in dual-phase steels during tensile shear test. Mater. Des. 2014; 55:366-372. http://dx.doi.org/10.1016/j.matdes.2013.09.040
17. Onar V. Mechanical and Microstructural Characterizations of Resistance Spot Welded Dissimilar TWIP/304L Stainless Steel. Trans. Indian Inst. Met. 2022; 75(7):1731-1739. https://doi.org/10.1007/s12666-021-02446-9
18. Özen F, Onar V, Bulca M, Aslanlar S. Resistance spot weldability of Fe-15.4Mn-2.1Al-1.2C twinning induced plasticity steel. Materialwiss. Werkstofftech. 2023; 54:857–870. https://doi.org/10.1002/mawe.202200241
19. Özen F. Mechanical and microstructural characterization of resistance spot welded dissimilar TWIP1000/TRIP800 joints. Mater. Test. 2024; 66(1):9-21.
20. Özen F, Aslanlar S. Mechanical and microstructural evaluation of resistance spot welded dissimilar TWIP/martensitic steel joints. J. Adv. Manuf. Technol. 2021; 113:3473-3489. https://doi.org/10.1007/s00170-021-06848-3